UNIVERSITÀ DEGLI STUDI DI PAVIA
DIPARTIMENTO DI FISICA

Cyclotron production of the innovative radionuclides ^{47}Sc, ^{155}Tb, and ^{52g}Mn from cross section modeling to dosimetric evaluation

PhD Thesis

Francesca Barbaro

Supervisors: Luciano Canton, Silva Bortolussi

October 2023

Cyclotron production of the innovative radionuclides ^{47}Sc, ^{155}Tb, and ^{52g}Mn from cross section modeling to dosimetric evaluation

Abstract

The novel approach of the precision nuclear medicine is tailoring the treatments on the patient instead of adapting the patient to standard therapies. The uniqueness of the patients' response to treatments is now the focus of the latest research. To achieve this goal the use of radiopharmaceuticals suitable for theranostic applications is a valid strategy. Theranostics is simply the merge of two other words, therapy and diagnostics. The keynote of theranostic is to conjugate diagnosis and therapy, namely it is the certainty to reach the sensitive target visualized through imaging scans also at the therapy stage, exploiting the chemically identical composition of the drug used for both imaging and therapy. Scandium-47 and Terbium-155 are both very promising and innovative radionuclides for precision nuclear medicine and the scientific community currently debates about feasible production routes in compliance with the clinical standards. Moreover, since the key role of imaging scans, the interest in Manganese-52g lies in its viability in PET/β^+ Multimodal Imaging technique.

For the production of ^{47}Sc the cyclotron routes ^{49}Ti(p,2pn), ^{49}Ti(d,α), and ^{50}Ti(p,α) have been investigated. The nuclear code TALYS has been employed to simulate the cross sections of both ^{47}Sc and its main contaminants. The theoretical results of the cross sections have been compared with the the new preliminary REMIX (Research on Emerging Medical radIonuclides from the X-sections) data and few old datasets of the literature. To better reproduce the cross sections an optimization through genetic algorithms, inspired by Darwin's theory of natural selection, has been performed. The tuning of the models free parameters of the nuclear level densities allows to improve the theoretical cross sections and to be more precise in the prediction of the activities and radionuclidic purity (RNP) derived from the cross sections evaluation. The requirements of the European Pharmacopoeia set out a radionuclidic purity greater than 99% (suggested, but not mandatory). According to the RNP, the channel ^{49}Ti(p,2pn)^{47}Sc does not lead to a ^{47}Sc production with sufficient quality and purity to meet clinical standards. Results indicate the production route ^{49}Ti(d,α)^{47}Sc as a valid

alternative when ^{49}Ti targets are considered and the reaction ^{50}Ti(p,α) adequate for applications since also in this case the medical requirements of purity are satisfied. However, another important parameter to consider is the Dose Increase (DI) caused by the impurities generated by the production routes, and this complements the information derived from the RNP. It quantified the increase of the dose to the patients' organs due to the contaminants. There is no strict indication, but generally the DI should be maintained within the limit of 10%. For the nuclear reaction ^{155}Gd(p,n)^{155}Tb a theoretical analysis form the cross sections evaluation to the dosimetric calculations have been carried out. The interest of ^{155}Tb for clinics is on the rise, however its availability in the market with sufficient purity to be adequate for actual applications is still an open issue. In this work the attention is focused on the level of enrichment of the ^{155}Gd targets. When enriched targets are used, the major contribution to the contamination depends on the amount of impurities in the target. This work identified a crucial issue in the target enrichment and found the minimum level of enrichment necessary for the use of ^{155}Tb-imaging method in clinics. For the ^{52g}Mn production the reaction ^{nat}V(α,x)^{52g}Mn has been proposed as a possible alternative to the standard ^{nat}Cr(p,x)^{52g}Mn one. Both channels provide clinically acceptable $^{52g}MnCl_2$ for PET imaging, however the comparison suggests that the use of α on ^{nat}V leads to higher yield and higher purity, resulting in more favorable radiation dosimetry for patients.

CONTENTS

NOMENCLATURE

CN	Compound Nucleus
CoKiMo	Compartmental Kinetic Model
CT	Computed Tomography
CTM	Constant Temperature Model
DI	Dose Increase
DWBA	Distorted Wave Born approximation
EoB	End of Bombardment
FGM	Fermi Gas Model
GA	Genetic Algorithm
GDH	Geometry Dependent Hybrid
GMP	Good Manufacturing Practice
GSM	Generalized Superfluid Model
HFB	Hartree-Fock-Bogoliubov
HF-BCS	Hartree-Fock plus Bardeen-Cooper-Schrieffer model
HFM	Hartree-Fock model
IAEA	Internationale Atomic Energy Agency
ICRP	International Commission on Radiological Protection
INFN	National Institute of Nuclear Physics
ISOL	Isotope Separation On-Line
ISOLDE	Isotope Separator On Line Device
LARAMED	LAboratory of RADionuclides for MEDicine
LD	level density
MEDICIS	Medical Isotopes Collected from ISOLDE
MEMRI	Manganese-Enhanced Magnetic Resonance Imaging
METRICS	Multimodal pET/mRi Imaging with Cyclotron-produced $^{52/51}$Mn iSotopes
MR	Magnetic Resonance
MRI	Magnetic Resonance Imaging
NLD	Nuclear Level Density
OLINDA	Organ Level Internal Dose Assessment
PASTA	Production with Accelerator of ^{47}Sc for Theranostic Applications
PE	pre-equilibrium
PET	Positron Emission Tomography
PSB	Proton Synchrotron Booster
REMIX	Research on Emerging Medical radIonuclides from the X-sections
RNP	Radionuclidic Purity
SPECT	Single Photon Emission Computed Tomography
SPES	Selective Production of Exotic Species
TRT	Targeted Radionuclide Therapy

LIST OF TABLES

LIST OF FIGURES

CHAPTER 1

Introduction

Cancer is the second leading cause of death in the world after cardiovascular diseases. The word cancer comes from a Greek word karkinos, giant crab from Greek mythology, coined by the Greek physician Hippocrates (460-370 BC), who is considered the "Father of Medicine". Nevertheless, the discovery of this disease can not be credited to him. Some of the earliest evidence of human bone cancer was found in mummies in ancient Egypt and in ancient manuscripts dates about 1600 B.C. The world's oldest recorded case of breast cancer dates back to 1500 B.C. and no form treatment were recorded, only palliative treatment. In ancient Egypt, according to inscriptions, surface tumors were surgically removed in a similar manner as they are removed today [8].

Cancer develops when normal cells begin to grow out of control. Several are the treatment options: surgery, chemotherapy, and radiotherapy. When possible the surgery is the first choice and, in some cases, to ensure the complete removal of all cancer cells, patients go through chemotherapy and/or radiation therapy too. Chemotherapy is a drug treatment that uses powerful chemicals to kill fast-growing cells, inhibit cell proliferation, and avoid invasion and metastasis. But chemotherapy is highly toxic due to the effect on normal cells as well. Concerning the radiation therapy, it is possible to distinguish between external and internal sources depending on the position of the radiation source in relation to the patient. Conventional radiotherapy uses external X-rays beams to eradicate the tumor. Hadrontherapy is a form of radiotherapy for the treatment and cure of tumours that are often surgically inoperable or resistant to traditional radiotherapy treatments and it involves the use of proton, carbon ions or heavier ions as external beams. For all these therapies, even though the physical principles they rely on are different, the key is the spatial precision and so the perfect definition of the energy beam that allows to reach the exact depth of the tumor mass, sparing the surrounding healthy and sensitive tissues. On the other hand, the therapy that exploits internal radiation source is classified into brachytherapy, or targeted radionuclide therapy (TRT). The former consists in a

sealed-source interstitial/intracavitary radionuclide therapy (RT). Interstitial means a radioactive wires or seed implanted directly into the tumor volume, while the radioactive source is intracavitary when placed in body cavities in proximity to the tumor. The TRT is, instead, a intravenous or oral administration of a non-sealed radionuclide itself or in a medication, the so called radiopharmaceutical. This internal RT is based on the concept of the biological selectivity. The goal is the precise delivery of cytotoxic radiation to cancer cells by the administration of radiopharmaceuticals. A specific biological site is recognised in a way by a drug that carries a specific radioactive agent suitable for some treatment. The accumulation of the drug can occur via active or passive targeting. In the passive targeting the accumulation of drug carriers at a particular site is due to the inherent pathophysiological, physicochemical or pharmacological factors. While in the active targeting the drug carriers are built with active targeting ligands that possess a high affinity for binding to a specific cell type or tissue in the organism or expressed surface receptors. The second case enhances the therapeutic efficiency and reduces the side effects [9]. There are several ways to accomplish the targeting selection, as shown in Fig.1.1.

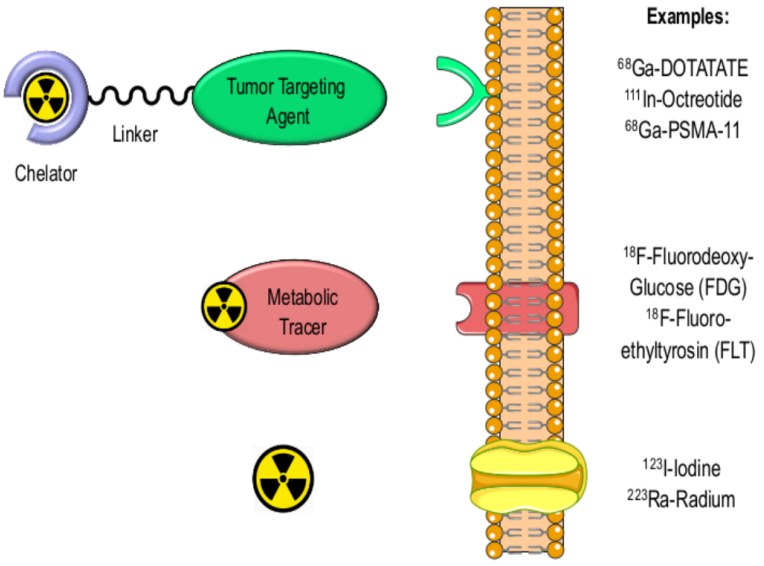

Figure 1.1 Targeting selection

A molecule, linked to the radioactive agent which is stabilized by a chelating complex, is designed to recognize a particular receptor expressed on the surface of a certain type of

tumor cell. Another way to enhance the specificity drug-target is the use of a metabolic tracer labelled with a radionuclide to exploit the metabolic pathways to reach a precise site. Finally, it is possible to deliver the radionuclide in its simplest form leaning on the biological affinity between the radioactive agent and the tissue to reach the sensitive target. The TRT, regardless the way the drug is designed, has a great potential in comparison to conventional radiation therapy. Indeed the biological specificity and selectivity allows to identify tumor masses of all sizes and this means that, in principle, even the metastasis can be recognised. This result is next to impossible to accomplish when external beams are considered.

In comparison to standard drugs, radiopharmaceuticals need much higher target-to-background ratios to increase its uptake on the sensitive target and/or reduce the unnecessary irradiation of healthy tissues. To this purpose a good radiopharmaceutical has to have an high affinity and selectivity for its target, a negligible binding to other non-specific cell components, a rapid uptake, a sufficient period of retention in the region of interest, and a rapid clearance from the rest of the body [10].

The eligibility of a radiopharmaceutical as imaging and/or therapeutic agent depends on the physical features the radionuclide is made of. Currently, a new word has entered in the field of the nuclear medicine: theranostics. It is simply the merging of two other words, therapy and diagnostics. Theranostics is a strategical approach of nuclear precision medicine that conjugates diagnosis and therapy in the interest of the maximum benefit with the minimum impact on the patients' health. Due to its complexity, theranostics is a topic constantly in progress, for which interdisciplinary research and technological innovation are important assets. The production of new radionuclides for theranostic radiopharmaceuticals requires expertise in theoretical and experimental nuclear physics, dosimetry, radiochemistry, radiopharmacy, and diagnostic imaging. The nuclear features of each radionuclide define its possible and specific medical application. Depending on that, they can be classified as diagnostic and/or therapeutic radionuclides. For example, β^+ emitters, like ^{18}F and ^{11}C, are usual Positron Emission Tomography (PET) tracers, while ^{99m}Tc and ^{123}I are typical

γ-emitters suitable for Single-Photon Emission Computed Tomography (SPECT) diagnosis imaging. Radionuclides with characteristic α and β^- decay, like ^{225}Ac and ^{177}Lu, and conversion electrons and Auger electrons emitters, like ^{186}Re and ^{67}Ga, are instead adequate for cancer treatment. The periodic table of elements, presented in fig. 1.2, summarizes the situation. Each colour corresponds to a specific medical application, that is a certain radiation and decay mode. At a glance it is possible to distinguish which element is suitable for imaging and/or therapy on the basis of its colours.

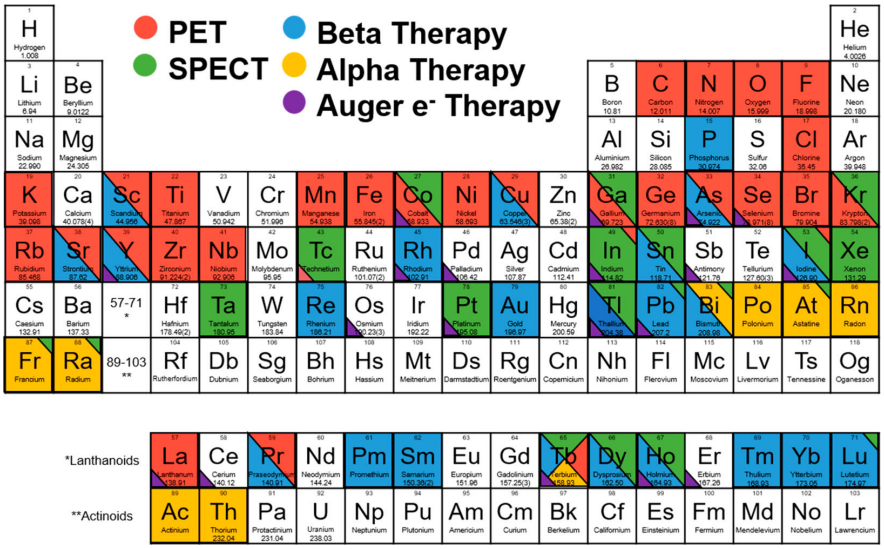

Figure 1.2 The periodic table of elements. For each colored element its decay mode is highlighted and so the related suitable medical practise. Currently, other radionuclides gained interest in nuclear medicine applications. Among them it is worth noting ^{111}Ag, ^{128}Ba and ^{128}Cs. Further details are available at PRISMAP website [4].

Nowadays, to meet the medical demand, several protocols are based on combinations of different radionuclides, implicating the delivery of two compounds of distinct chemical composition with different kinetics and biodistribution. To reduce the dose released and to optimize the balance between the benefit and the acceptable toxicity risk, the latest research aim to the identification of a single radionuclide able to satisfy the theranostic requirement. Indeed, the advantage of a single–element radiopharmaceutical is the chemically identical composition of the drug used for both imaging and therapy. This means same biodistribution of the radiopharmaceutical for both medical investigations, ensuring the treatment efficacy based on a precise diagnostic information. Theranostics allows personalized treatments on the concept “what we see is what we treat (almost)”.

Patients with similar disease could respond to a radiopharmaceutical differently. The use of a small amount of radiopharmaceutical for an imaging scan makes it possible to measure the uptake of the compound and thus to determine in advance the effectiveness of the therapy for each specific patient. The novel approach of the precision medicine is tailoring the treatments on the patient instead of adapting the patient to standard therapies. The uniqueness of the patients' response to treatments is now the focus of the latest research. Thus the search of innovative radionuclides suitable for theranostics is always driven by the idea that the patient is the main focus.

In recent years, the theranostic potential of Rare Earth radionuclides has capture the attention of the scientific community. Their diverse and favourable decay characteristics can cover the wide range of medical applications. Examples are: ^{149}Tb for α-therapy; ^{47}Sc, ^{161}Tb, ^{166}Ho, ^{153}Sm, ^{169}Er for β^- therapy; ^{161}Tb, ^{135}La, ^{165}Er for Auger electron therapy; ^{43}Sc, ^{44}Sc, ^{149}Tb, ^{152}Tb, ^{132}La, ^{133}La for positron emission tomography; ^{47}Sc, ^{155}Tb, ^{152}Tb, ^{161}Tb, ^{166}Ho, ^{153}Sm, ^{170}Tm, ^{152}Tb, ^{161}Tb for single photon emission computed tomography [11–13]. Among the aforementioned radionuclides it is possible to identify pairs that belong to the same element in which one is suitable for imaging and the other for therapy, or single radionuclides with a dual functionality and so adequate for imaging and therapy at the same time, due to their favourable decay. [14] These two cases perfectly embrace the imperative for effective theranostic treatment regimens of administering a single radiopharmaceutical able to meet both medical purposes. Frequently, the diagnostic and therapeutic radionuclides are incorporated into different targeting molecules/vectors, that could exhibit diverse biodistribution and kinetics in the body. In order to significantly reduce the variability in these factors after administration, the radiopharmaceutical must ideally exhibit identical biodistribution and selective tumour uptake. To tandem imaging and therapy and taking the advantage on the basis of the complementary features of the related radionuclides, the best option is a single radiopharmaceutical made of matched pairs or labelled with a sole radionuclide suitable for both medical applications. Furthermore, an additional advantage is the possibility to image the patient during and/or after a treatment to assess the progress achieved and schedule a second administration if necessary.

This thesis focuses on the cyclotron production of the radionuclides ^{47}Sc, ^{155}Tb, and ^{52g}Mn. This last is an interesting radionuclide for multimodal imaging techniques (PET-MRI), while the first two are suitable for theranostic applications. These radionuclides are the focus of two INFN projects in which I participated: METRICS (Multimodal pET/mRi Imaging with Cyclotron-produced $^{52/51}$Mn iSotopes) and REMIX (Research on Emerging Medical radIonuclides from the X-sections) that concerns precisely the production of ^{47}Sc and ^{155}Tb.

The potential of ^{47}Sc stems from its favorable β^- decay properties accompanied by the emission of γ-rays of an ideal energy for SPECT imaging. Moreover, it may be easily combined with β^+ emitters (PET), such as ^{43}Sc and ^{44}Sc, for production of theranostic compounds. Detailed decay information are presented in Chapter 3. Despite interesting properties, the use of ^{47}Sc theranostic radionuclides in preclinical studies and clinical trials is curtailed by their limited availability due to a lack of widely established production methods. Indeed, the production methods for ^{47}Sc are still at an early stage and the research is still devoted to find a reliable production route, which guarantees a sufficient quantity and purity of the radionuclide. This topic has been discussed within a IAEA Coordinated Research Project (CRP) in 2016 for the purpose of identifying the technical issues related to the production and quality control of this emerging radionuclide, together with ^{67}Cu and ^{186}Re [15]. Although the development of ^{47}Sc is still in its infancy, its therapeutic potential has been demonstrated preclinically. The ^{47}Sc-folate was successfully demonstrated to be effective in delaying the tumor growth and increasing the survival time of treated mice, compared to an untreated control group. The matching of ^{47}Sc with its diagnostic counterpart ^{43}Sc or ^{44}Sc makes it more appealing since it results in a promising theranostic agent. It has been demonstrated that PET imaging with ^{43}Sc or ^{44}Sc are potentially advantageous over the currently in use ^{68}Ga, due to an half-lives almost 4 times longer than Ga, which would enable longer acquisition times, better image quality, and the shipment Sc-radiopharmaceuticals to distant PET facilities [16].

For ^{47}Sc production with low-energy proton beams, which can be provided by standard hospital cyclotrons, the use of ^{50}Ti targets is promising. Similarly, the

reaction d-^{49}Ti is appealing. A comprehensive explanation of the possible production methods, considering both already tested and novel approaches, is discussed in Chapter 3.

^{155}Tb is an emerging radionuclide of considerable interest for metabolic radiotherapy. As γ-emitter, it is suitable for SPECT imaging, and, due to its emission of both Auger and conversion electrons, it might be a possible radionuclide also for targeted therapy. Moreover, the possibility to pair ^{155}Tb with other Terbium-isotopes makes it more attractive and flexible in nuclear medicine applications. Currently, ^{155}Tb is a new entry in the radiopharmaceutical field and its production via ^{155}Gd(p,n)^{155}Tb is still at an early stage. The progression from bench to bedside has been jeopardized by the inadequate level of purity of the production methods, due to the co-production of harmful contaminants. Further investigations to optimize and purify the ^{155}Tb production are much needed. That is exactly ^{155}Tb the first radioisotope produced by CERN-MEDICIS (Medical Isotopes Collected from ISOLDE) in 2017 [17]. At the ISOLDE (Isotope Separator On Line DEvice) facility, physicists bombard various targets with beams of 1.4 GeV protons delivered by the CERN PSB (Proton Synchrotron Booster). A large proportion of the primary beam still remain available to proceed with the parasitic irradiation of the MEDICIS target. Adding a second target for MEDICIS behind the first will allow to take advantage of the protons that would be otherwise lost into the beam dump, without interrupting ISOLDE's scheduled experimental programme, for the purpose of researching non-conventional radioisotopes for medical research. The MEDICIS target is exposed to the fraction of the primary beam which did not interact with the ISOLDE target as well as to the secondary beam produced from the impact of the 1.4 GeV proton beam on the upstream ISOLDE target. The concept of the isotope separation on line retrieves the ISOLPHARM project, which is based on the ISOL (Isotope Separation On-Line) technology, an accelerator-based method currently implemented at the Legnaro National Laboratories of the National Institute for Nuclear Physics. ISOLPHARM will exploit the SPES (Selective Production of Exotic Species) Radioactive Ion Beams (E = 40MeV and I = 200 μA) to produce a wide set of high quality (carrier-free) radionuclides suitable for applications in nuclear medicine. The purity of the

production is favoured at the expense of its amount. The above mentioned SPES project aims at the realisation of an accelerator facility for research in the fields of Fundamental Physics and Interdisciplinary Physics. It is divided in four phases and the SPES-γ one is devoted to the production of radionuclides for medical purposes. The installed cyclotron is a B70 accelerator able to produce protons with energy 35-70 MeV and maximum intensity of 750 μA. The beam provided by the SPES cyclotron will be used for the LARAMED (LAboratory of RADionuclides for MEDicine) project, designated to the production of medical radionuclides and radiopharmaceuticals [18].

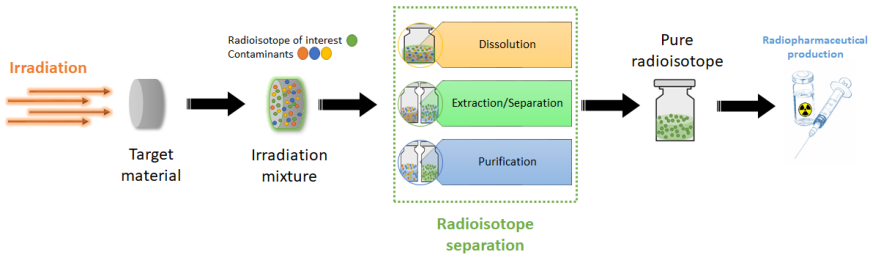

Figure 1.3 Outline of the radiopharmaceuticals' production phases.

Fig. 1.3 shows the production chain of a radiopharmaceutical. The direct activation of a dedicated target occurs when the projectile delivered by the cyclotron impinges on it. At this stage the radionuclide of interest is produced in concomitance with the contaminants. Therefore, the target radiochemical processing to extract and purify the desired radionuclide is necessary. Quality controls of the final product are performed and finally the radiolabelling of the radiopharmaceutical is accomplished. The REMIX (Research on Emerging Medical radIonuclides from the X-sections) project [19] is inserted in the LARAMED framework, a INFN CSN5 collaboration among INFN-LNL, INFN Pavia, Università di Pavia, INFN Padova, Università di Padova, INFN Milano, Università di Milano, Università di Ferrara, Istituto Oncologico Veneto, Ospedale Sacro Cuore Don Calabria Negrar. REMIX aims to investigate new cyclotron routes for producing ^{47}Sc and ^{155}Tb, two innovative and promising radionuclides for medical theranostic applications. This investigation is linked to applied research in nuclear medicine, performed in cyclotron facilities and involves both small low-energy cyclotrons (E up to 20 MeV) available in hospitals such ad Sacro Cuore Don Calabria Hospital Negrar, and intermediate-energy cyclotrons (E up

to 70 MeV) available in research centres such as ARRONAX (Nantes, France) or INFN-LNL (Legnaro, Italy). More widely, this research is inserted within a multidisciplinary context where the interconnections among theoretical and experimental nuclear physics, dosimetry, radiochemistry, radiopharmacy, and diagnostic imaging are essential.

Imaging techniques plays a leading role in relevant clinical applications. For a precise delivery of therapy or a successful surgery, high-quality images are essential. Diagnostic scans are a prerequisite for an optimal target definition, allowing to model the patients' disease and anatomy. A more detailed information gained through the acquisition of such images leads to a better planning of the medical treatments. MultiModal Imaging is a branch of the nuclear medicine that combines morphological and functional images acquired from different modalities for a more detailed image. The acquisition of the images can be performed at different times (asynchronous) or simultaneously (synchronous). In the former case the merging of the images needs digital image manipulation techniques, for the latter it is done automatically. The asynchronous post-processing solution entails various constraints, due to the different positioning of the patient in the two scans acquired at different times in separated machines. To achieve consistency in time and space the synchronous image acquisition is the best solution [20]. In the field of diagnostic imaging SPECT-CT, PET-CT are a standard, commonly used in several medical practises, while PET-MR is a relatively new technique. Magnetic resonance provides excellent soft-tissue contrast and multidimensional functional, structural and morphological information. The combination of multidimensional and molecular information provided by PET-MR allows a deeper understanding of the complex pathophysiological processes involved in diseases. Furthermore, the radiation dose for PET-MR is lower when compared to PET-CT, and this is an advantage for repeated studies aimed at assessing a disease progression and therapy response. Manganese-labeled compounds are valid candidate for PET-MRI technique. Among the manganese radionuclides ^{52g}Mn, ^{52m}Mn, and ^{51}Mn are suitable for PET scans [21]. Here the interest is focused on ^{52g}Mn. The long half-life ($T_{1/2}$ = 5.6 days) of ^{52g}Mn makes it suitable for the radiolabeling of antibodies and other slow biological compounds for the study of

pharmacokinetics. In addition, high resolution PET images are possible thanks to its β^+ emission of about 0.6 MeV. It is necessary to first produce a ^{52g}Mn-labeled compound for PET and, separately, the same compound containing only paramagnetic manganese for MRI. These two molecular agents should have the same chemical composition in order to probe the same biological vector, but they act separately because of the differences in sensitivity requested by PET and MRI scans [22].

The production of ^{52g}Mn is another main topic of this thesis. The MultiModal Imaging with Manganese compounds is also the goal of the METRICS (Multimodal pET/mRi Imaging with Cyclotron-produced $^{52/51}$Mn iSotopes) experiment, a CSN5-INFN project. The scientific interest arises from the possibility to investigate an alternative production route, ^{nat}V(α,x)^{52g}Mn, with potentially higher yield and better radionuclidic purity compared to the standard nuclear reaction ^{nat}Cr(p,x)^{52g}Mn. To complete the analysis dosimetric assessments are fundamental to verify the impact of the radionuclide as well as the impact of the contaminants in terms of radionuclidic purity and of dose released to the patient organs after a radiopharmaceutical administration. This comparison between production methods has been the first testbed for approaching the computational dosimetry. Following the same steps, the theoretical-dosimetric analysis will be adapted to the ^{155}Tb production from enriched Gadolinium targets.

CHAPTER 2

From cross section modeling to dosimetric evaluation

2.1 Cross section

The bombardment of a target by charged particle beams, i.e. p, d, t, ^{3}He, alpha or heavy ion beams, coming from an accelerator is a process that gives rise to a nuclear reaction. The collision of two nuclei can lead to final products different from the initial one, similarly to a chemical reaction. Unlike a chemical reaction, the resulting products of a nuclear reaction are not determined uniquely. This means that, considering two or more initial reactants, quite a few final products could exist with an unlimited number of available quantum states. Each reaction branch, with well defined quantum states of the participants, is known as channel, namely entrance and exit channels. If some of the final products are in an excited state different exit channels would be reached. The probability that a nuclear reaction takes place through a certain exit channel depends on the energy of the incident particle and is measured by the cross section for that channel. This quantity essentially gives a measure of the probability for a reaction to occur.
One can start to consider the general case of a beam of particles incident on a target, assuming the beam to be broader than the target [23], as illustrated in Fig. 2.1. The particles of the beam are supposed to be randomly distributed in space and time. Formally, the flux ϕ is defined as the number of incident particles per unit area and per unit time. Next, the focus is at the number of particles scattered into the solid angle dΩ per unit time. The word scattering refers to the outgoing particle emitted in the solid angle Ω. In average, the number of particles scattered in a solid angle dΩ per unit time will tend toward a fixed value dN_s. The differential cross-section is then defined as:

$$\frac{d\sigma}{d\Omega}(E,\Omega) = \frac{1}{\Phi} \cdot \frac{dN_s}{d\Omega}, \tag{2.1}$$

where $\frac{d\sigma}{d\Omega}$ is the average fraction of particles scattered into dΩ per unit time, per unit incident flux Φ, and for dΩ infinitesimal. Note that because of the dimension of Φ,

dσ has the dimension of an area. In Literature, the cross section is usually measured in units of barns, and 1 barn corresponds to 10^{-24} cm^2. One can interpret dσ as the geometric cross sectional area of the target intercepting the beam. In other words, the fraction of flux incident on this area will interact with the target and scatter into the solid angle dΩ while all those missing dσ will not.

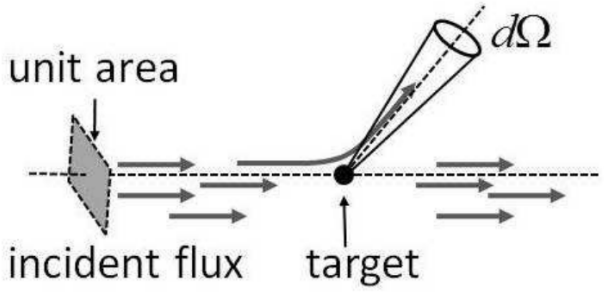

Figure 2.1 Schematic representation of a scattering experiment.

In general, the differential cross-section of a process varies with the energy of the reaction and with the angle at which the particle is scattered. The total cross-section at the energy E can be derived as the integral of the differential cross-section over all solid angles,

$$\sigma(E) = \int \frac{d\sigma}{d\Omega}(E,\Omega)d\Omega. \qquad (\mathbf{2.2})$$

Shifting the description to a real case, the target is usually a slab of material containing many scattering centers, Fig. 2.2, and it is desired to know how many interactions occur on average when that target is exposed to a beam of incident particles. Assuming the slab not too thick, so that the likelihood of interaction is low, the number of centers per unit perpendicular area which will be seen by the beam is n·δx, where n is the density of centers and δx the thickness of the material along the direction of the beam. The number of incident particles eligible for an interaction per unit of time is Φ· A, where A is the perpendicular area of the target and the condition of a beam broader than the

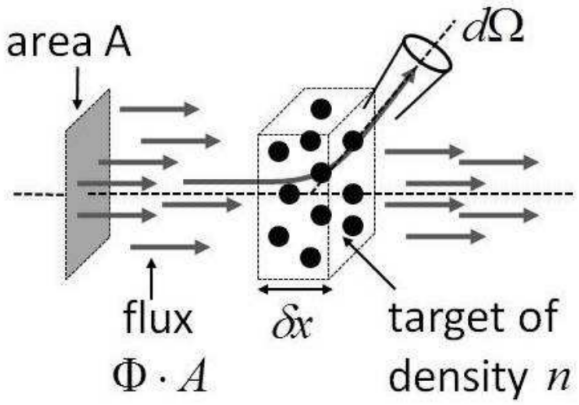

Figure 2.2 Illustration of the scattering cross-section for an extended target, a slab of material containing many scattering center.

target is satisfied. The average number of scattered particles into dΩ per unit time is:

$$N_s(\Omega) = \Phi \cdot A \cdot n \cdot \delta x \cdot \frac{d\sigma}{d\Omega} \cdot \Omega \qquad (\mathbf{2.3})$$

One can derive the total number of scattered into all angles, that is

$$N_{tot} = \Phi \cdot A \cdot n \cdot \delta x \cdot \sigma \qquad (\mathbf{2.4})$$

In the case the beam is smaller than the target, A results equal to the area irradiated by the beam. If N_{tot} is divided by the total number of incident particles per unit time ($\Phi \cdot A$), the probability for the scattering of a single particle in a thickness δx is

$$P_{\delta x} = n \cdot \sigma \cdot \delta x \qquad (\mathbf{2.5})$$

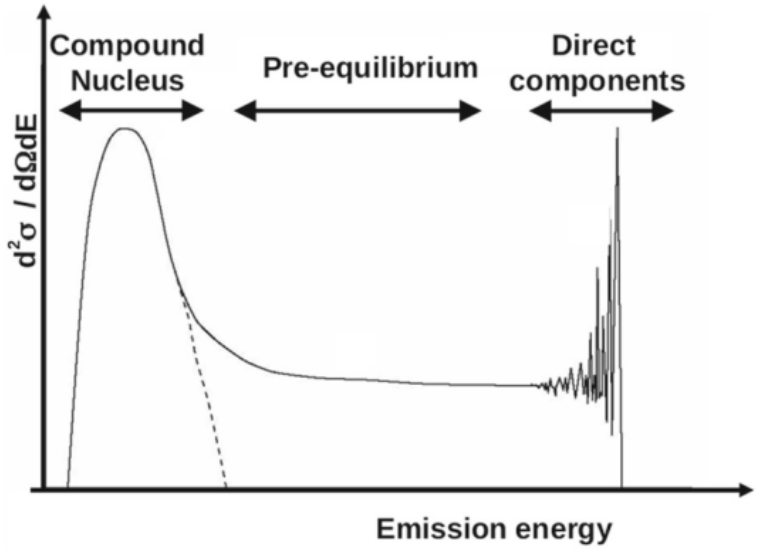

Figure 2.3 A sketch of a nuclear reaction cross section where the three reaction mechanisms that depend on the particle-emission energy are highlighted [5]. Namely, direct reactions (dir), pre-equilibrium emission (preeq), and compound nucleus formation and decay (CN).

2.2 Nuclear reaction mechanisms

Nuclear reactions proceed through many possible distinct mechanisms. Here an overview over the various reaction mechanisms is given. A much more detailed description can be found in Ref. [24], which is in essence a manual of the nuclear reaction code TALYS, described in details in section 2.2.3. In addition it has been recently published in EPJA a very comprehensive review article on nuclear reaction modeling [25]. The main reaction mechanisms that are important for the calculation of the cross sections are direct reactions, compound nucleus formation and decay, and pre-equilibrium emission. Thus, the cross section can be separated approximately into the three parts:

$$\sigma_{react} = \sigma_{dir} + \sigma_{preeq} + \sigma_{CN} \tag{2.6}$$

where the different contributions depend on the energy of the emitted particles.

Briefly, in direct reactions the projectile and the target have an interaction of short

duration, with possible exchange of energy or particles between them. Another mechanism involves the fusion of the projectile with the target, the available energy is distributed among all nucleons and a highly excited compound nucleus is formed. The decay of the compound nucleus leads to the final products of the reaction. In between the pre-equilibrium reactions, that is the nuclear complex breaks up before it reaches the statistical equilibrium.

2.2.1 Direct reactions

Direct reactions are more probable as the energy of the incident particle increases and they happen at a time of the order of 10^{-22} s. They correspond typically to a single-step interaction between the projectile and one nucleon of the target, expressed as $a + A \longrightarrow b + B$. These are called peripheral reactions, where only a few nucleons of the surface participate. In addition, direct reactions exhibit a peculiar angular distribution. Since the initial and final channels of the collision process are strongly correlated, the distribution presents a forward prominent peak and smaller peaks at larger angles, the typical form of a diffraction figure. Several types of direct reactions can be distinguished, depending on the nature of the interaction. 1) Elastic scattering, in which the particle and the target nucleus do not change their energy states, but their directions. 2) The inelastic scattering of the incident particle, which implies an energy transfer to excite a collective mode of the nucleus. 3) In a transfer reaction one or more nucleons are transferred between the projectile and the target. Therefore, it involves a modification in the nuclear composition, i.e. pick-up and stripping reactions. In a pick-up reaction nucleons from the target nucleus are removed and added to the projectile. In a stripping reaction nucleons are transferred to a target nucleus from the passing particle. 4) Break-up reaction, in which the particle splits into two or more fragments after colliding with the target nucleus. 5) A knock-out reaction, engages an incident particle that knocks out a single nucleon or a light cluster of the target nucleus and continues in its path, resulting in three reaction products.

The main theoretical approach to analyse the direct reactions leans on the distorted wave Born approximation (DWBA) and coupled-channel formalism [26].

2.2.2 Pre-equilibrium

Pre-equilibrium is the intermediate reaction mechanism that embodies both direct and compound features. Pre-equilibrium reactions occur on a longer timescale than a direct reaction but on a shorter timescale than compound nucleus formation, before the full equilibrium takes place. It involves a few multiple collisions where few nucleons of the target participate by interacting with the incoming projectile, thus sharing the incoming energy momentum of the projectile among a limited set of nucleons. As the scattering proceeds, increasingly more complex states are created in the residual system with each successive process gradually losing information contained in the initial reaction.

There are two distinct approaches to describe the pre-equilibrium process for nucleon-induced reactions on medium- to heavy-mass nuclei: phenomenological-based models and purely quantum mechanical ones. Quantum mechanical models use the DWBA for the multi-step process. These models are based on statistical assumptions mainly for the two-step process, where the configuration made of two particles and two holes is created by the NN interaction [27].

The second approach to describe the pre-equilibrium processes [28] is based on phenomenological models, such as the exciton model. The exciton model defines the nuclear state by the total number of particles above the Fermi level plus holes below the Fermi sea and by the corresponding total excitation energy E. The pre-equilibrium scattering is treated as a chain of particle-hole excitations. Transitions between particle-hole configurations with the same exciton number have equal probability. The time-dependent master equations controls the evolution of the scattering process through transitions to more or less complex configurations [29]. At any step in this process an outgoing particle may be emitted which is referred to as pre-equilibrium emission. If the emission takes place at an early stage only few interaction steps are involved and the process has similar characteristics to a direct mechanism, while if many intra-nuclear interactions increase step by step the number of excitations, the pre-equilibrium process tends to reach a statistical equilibrium, approaching to the CN limit.

2.2.3 Compound nucleus formation

Compound nuclear reactions are found to take place when a projectile is captured creating a compound nucleus in an excited energy state which subsequently decays. It is assumed that the compound nucleus is formed with an excitation energy high enough so that many states may be excited by the interaction of the incident particle with the target nucleus. Moreover, the incident energy is shared between the individual components of the nucleus which fully equilibrates before decay takes place. This mechanism dominates at low energies, around 10 MeV. The initial energy is distributed among all nucleons and no particle is emitted. This is a slow process that requires reaction times around 10^{-18} s to occur. The final nucleus with X + 1 nucleons, that is an highly unstable nucleus, has an excitation energy equal to the kinetic energy of the incident projectile plus the binding energy of the nucleons. The de-excitation process is not necessarily immediate and the excited nucleus can live relatively for long before its decay. In the final stage the compound nucleus can also evaporate one or more particles.

The general notation [30] for the most common situation in which two final products are formed is:

$$a + A \longrightarrow CN^{*} \longrightarrow B + b$$

The asterisk indicates the excited state of the compound nucleus (CN). The CN lives long enough to "forget" how it was formed, thus the de-excitation to the final products b and B only depends on the energy, angular momentum and parity of the quantum state of the compound nucleus. The exit channels is independent of the way the compound nucleus is formed, viz no correlation exists between the formation and decay of the compound nucleus.

Under these circumstances, the occurrence of a nuclear reaction in two stages allows the cross section for a reaction A(a,b)B to be written as following

$\sigma(a,b) = \sigma_{CN}(a,A) \cdot P(b)$,

where σ(a,A) is the cross section of the compound nucleus formed from the projectile a and the target A and $P(b)$ is the probability that the compound nucleus emits a particle b leaving a residual nucleus B. If the quantum numbers of entrance and exit channels are well specified, i.e. if the reaction begins at an entrance channel α and ends at an exit channel β, one can write

$$\sigma(\alpha,\beta) = \sigma_{CN}(\alpha) \cdot \mathrm{P}(\beta).$$

It is possible to associate the probability P(β) to the width Γ_β of the channel β. Defining

$$\mathrm{P}(\beta) = \frac{\Gamma(\beta)}{\Gamma}$$

where Γ is the total width and $\tau = \frac{\hbar}{\Gamma}$ is the half- life of disintegration of the compound nucleus. The formula expresses the decay probability through channel β as the decay rate through that corresponding channel divided by the total decay rate.

The Hauser–Feshbach formalism [31], is used to describe the CN contribution to the cross section and the decay probability on the basis of the transmission coefficients. Several complexities are taken into account to better describe realistic situations. First, the summation over partial angular momenta taking into consideration the spin averaging over the initial states and the spin re-summation over the final one. Secondly, the spin recombination over the incoming channel and final channel must be accounted for, and finally, one has to impose the conservation conditions of total energy/momentum, angular momentum and parity. Two important further improvements of the Hauser–Feshbach theory are related to two corrections terms explained below.

The Hauser-Feshbach expression based on the independence hypothesis is too simple [5], particularly for low projectile energies. In realistic cases the hypothesis of complete independence between the entrance and exit channels has to be corrected by introducing a width fluctuation factor, $\mathrm{W}_{\alpha,\beta}$, to include interference effects and compensate for this approximation. The second correction is related to the level density ρ(E), that is a measure of the number of available energy states for the decay of the compound nucleus in the interval dE around the energy E. When the projectile energy is sufficiently large

for the compound nucleus to emit particles in the continuum of the residual levels it is necessary to introduce the nuclear level density every time it is unfeasible to describe the excited levels individually. Under these circumstances, the ρ(E, J, π), which represents the density of residual nuclear levels (J, π) with excitation energy E, is included in the transmission coefficients that are energy averaged.

The angular distribution of fragments, or evaporated particles, of a compound nucleus is isotropic in the center of mass.

2.3 Nuclear reaction code TALYS

Modern nuclear reaction codes are today the best tools to perform theoretical calculations in this field. For this research the TALYS simulation package [32], which is an empiric code actively developed and maintained, has been used. The aim of the authors is to provide a complete and high quality set of models [33] for the different reaction mechanisms that are relevant in the energy range of medical interest, namely, nuclear scattering, compound nucleus formation, and preequilibrium emission. Many state of-the-art nuclear models are included to cover most of the reaction mechanisms encountered in light particle–induced nuclear reactions. To the scope, TALYS incorporates six different level-density models (three phenomenological and three based on microscopic theories) and four different pre-equilibrium approaches (three based on the exciton model [29] and one on the fully quantum-mechanical multi-step approach [34]). An additional geometry dependent hybrid (GDH) model [35, 36], the new preequilibrium feature, has been added, enhancing the versatility of TALYS. The GDH model incorporates the diffusive surface properties into the pre-compound decay formalism. Indeed this hybrid model has been proposed by Blann to solve the exciton model deficiency in properly reproduce enhanced emissions from the nuclear surface [37].This code is also used to generate a reference library with simulated data named TALYS Evaluated Nuclear Data Library (TENDL) [38], which is often used for comparison with experimental data.

2.4 Nuclear level density

For low excitation energies nuclear excited levels display a discrete spectrum. When the excitation energy increases, the mean spacing of these levels reduces that it is experimentally impossible to distinguish all of them. Therefore, the individual description of each level is replaced by a description in the continuum by means of a level density function. The level densities are an important ingredients for both the statistical and pre-equilibrium models of nuclear reactions.

In other words, the nuclear level density is defined as the number of levels per unit of energy at a certain excitation energy. The levels in low energy region are well separated, so it is possible to calculate the levels by counting. As the excitation energy increases the spacing between levels gradually decreases while their width increases and the level density is defined by the function $\rho(E_x, J, \pi)$ and corresponds to the number of nuclear levels per MeV around an excitation energy E_x , for a certain spin J and parity π.

Several models for the level density description are included in the in TALYS nuclear reaction code, which range from phenomenological analytical expressions to tabulated level densities derived from microscopic models.

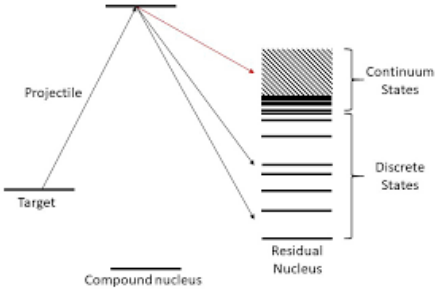

Figure 2.4 Formation and decay of compound nucleus [6].

Three are the semi-empirical analytical formulas frequently used to describe the level density. This approaches are based on the Fermi gas model, the constant temperature model, and the Gilbert-Cameron model [39].

2.4.1 Fermi Gas Model

In the Fermi Gas Model (FGM), it is assumed that the nucleons in a nucleus are non-interacting fermions, and they can only occupy single particle states with definite

excitation energies, spin projections, and parities due to the Pauli exclusion principle. It is based on the assumption that the single particle states which construct the excited levels of the nucleus are equally spaced, and that collective states as well as shell effects are not included. In this description the nuclear level density equation [40] depends on three parameters, the level density parameter a, the spin cut-off parameter σ, and the energy shift Δ.

$$\rho_F(E) = \frac{1}{\sqrt{2\pi}\sigma} \frac{\sqrt{\pi}}{12} \frac{e^{2\sqrt{aU}}}{12\sqrt{2}\sigma a^{1/4} U^{5/4}}, \tag{2.7}$$

where U is the effective excitation energy, defined as $U = E - \Delta$.

The level density parameter a is defined as a nuclide-specific constant and treated as a parameter indipendent from the energy. Ignatyuk et al. [41] found out that to describe a more realistic level density it is necessary to include an energy dependency of a to reflect the energy-dependent shell effects, maintaining valid the Fermi gas formulae.

The spin cut-off parameter σ represents the width of the angular momentum distribution of the level density. The general expression for the continuum is based on the observation that a nucleus possesses collective rotational energy that can not be used to excite the individual nucleons. There are two approaches to define σ. The first one is the semi-classical approach which assumes the nucleus is a rigid body sphere.The second approach is the quantum mechanical one by Ericson. The quantity σ can be defined semi-classically assuming for the nucleus a rigid body description; alternatively, fully quantum-mechanical approaches have beed adopted as well.

The energy shift Δ is an empirical parameter [42] which is related to the pairing energy and it simulates the odd-even effects in nuclei. This term accounts for the fact that pairs of nucleons must be separated before each component can be excited individually. The pairing effect can be mimicked as a shifted ground state energy so that the effective excitation energy is introduced as U = E - Δ.

2.4.2 Constant Temperature Model

The Constant Temperature Model (CTM) [42, 43] is based on the experimental evidence that the cumulative number of levels N(E), considering the first discrete level, is reproduced by the constant temperature law

$$N(E) = e^{\frac{(E-E_0)}{T}}, \tag{2.8}$$

where T is the nuclear temperature. N(E) is related to the nuclear level density by the formula

$$\rho_T(E) = \frac{dN(E)}{dE} = \frac{1}{T} e^{\frac{(E-E_0)}{T}} \tag{2.9}$$

The nuclear temperature does not depend on the excitation energy, and it is assumed to be constant over entire energy range. The two parameters E_0 and T can be determined from fitting the experimental data. In the Gilbert-Cameron model, both the constant temperature model and the Fermi gas model are used to describe the level density in a wide excitation energy region. At the low excitation energy, the nuclear level density is described by the CTM, while at high excitation energy region, the FGM is better to represent the nuclear level densities. These two models are smoothly connected at the certain matching energy E_m, at which $\rho_T(E_m)$, $\rho_F(E_m)$, and their derivatives are identical.

2.4.3 Back-shifted Fermi gas Model

The Back-shifted Fermi Gas level density consists of the general Fermi Gas formalism with only one essential deviation: instead of a constant temperature part, the model is expressed in terms of an effective excitation energy U = E_x - Δ_{BFM}, where E_x is the

true excitation energy and the energy shift is given by

$$\Delta_{BFM} = \chi \frac{12}{\sqrt{A}} + \delta \tag{2.10}$$

The χ values are -1, 0 or 1 for odd-odd, odd-even or even-even nuclei, respectively. The δ is an adjustable parameter to fit experimental data per nucleus [44].

2.4.4 Generalized Superfluid Model

The Generalized Superfluid Model (GSM) [42, 43] takes superconductive pairing correlations into account according to the Bardeen-Cooper-Schrieffer theory. The GSM resembles the CTM to the extent that it distinguishes between a low energy and a high energy region. Although, for the GSM this distinction follows naturally from the theory and does not depend on specific discrete levels that determine a matching energy. At low energy the pairing correlations strongly influence the level density and a phase transition from a superfluid behaviour is considered, while at higher energies the description follows the FGM.

2.4.5 Microscopic models

Microscopical models are an alternative approach to calculate the nuclear level density in energy and mass regions where experimental data are not available. Regarding microscopic models, some approximations pertaining to phenomenological models such as simplified approach to calculation of pairing, shell and collective effects are avoided.

It was only starting from the years 2000 that the microscopic descriptions became sufficiently accurate in the global NLD description, for an extremely large set of nuclides (about 8000/8500), to compete with the phenomenological models for practical applications. In one of the first approach the effective Skyrme-type nucleon-nucleon interactions have been employed in the context of mean-field theories [45]. The method used the Hartree-Fock plus Bardeen-Cooper-Schrieffer model (HF-BCS) to describe the many-body structure and to incorporate the pairing force. NLD was then calculated

using a microscopic statistical method [46]. Further advancements in microscopic NLD calculations were achieved [47, 48], by resorting to a more consistent (axially symmetric) Hartree-Fock-Bogoliubov (HFB) scheme with Skyrme interaction, with the NLD constructed using a shell-model combinatorial approach [49]. This lead to quite a few improvements, such as the determination of the parity dependence of the NLD, together with the inclusion of the collective aspects of both rotational and vibrational character in the theoretical description. More recently, a new study has been completed [50] with improvements in the microscopic description of the collective effects, both vibrational and rotational, based on the use of a new Gogny-type nucleon-nucleon effective interaction in the HFB approach. Also, the introduction of a temperature-dependent generalization allowed one to take into account the evolution of the nuclear deformation with increasing excitation energy, an important aspect that has been disregarded in previous treatments.

In the Hartree-Fock model (HFM) description, the level densities are tabulated at different excitation energies for both parities and different values of spins. Specifically, the level densities for more than 8500 nuclei are made available in tabular form at, for excitation energies up to 200 MeV and for spin values up to J = 49. The values in these tables can be rescaled by simple multiplication to fit experimental data. This technique has been successfully adopted in Ref. [51] to find a global best fit on the entire nuclide chart. In general the original HFM microscopic level densities have not been adjusted to experimental data and the tabulated values can be rescaled by using two parameters (c and p) according to the transformation

$$\rho(E,J,\pi) = exp(c\sqrt{E-p})\rho_{HFM}(E-p,J,\pi) \qquad (\mathbf{2.11})$$

The parameter p is called "pairing shift" in TALYS and allows to obtain the level density from the table at a different energy, and could also represent an energy shift caused by pairing or even shell effects. Parameter c provides an overall normalization of the level density. Adjusting p and c provides flexibility in fitting procedures. This approach let

to modify the original HFM level density and to obtain different "customized" tables, as allowed and shown in the TALYS manual and on the Reference Input Parameter Library (RIPL) [52].

2.5 Yield, activity, purity and dosimetric calculations

When nuclear reactions are investigated the assessment of the cross section is the first parameter that allows to evaluate the production yield of radionuclides under specific irradiation conditions, since it represents the probability of a certain reaction to occur, and so of a specific radionuclide to be produced. From the cross sections other quantities are derived, such as activities, yields, and purities. First, the most promising energy window for the production of the main radionuclide at low contamination shall be identified. The search of the ideal energy range that maximises the cross section of the radionuclide of interest, while minimizing the contribution from the contaminants allows to enhance the quality of the production. This is essential to assess the goodness of a certain reaction in compliance with the medical requirements.

In the following the main physical quantities are introduced. The rate R, that is the number of produced isotopes per second from a beam colliding on a target with a certain thickness can be derived from the expression [5, 23]

$$R = \frac{I_0}{z_{proj}|e|}\frac{N_a}{A}\int_{E_{out}}^{E_{in}} \sigma(E)\left(\frac{dE}{\rho_t dx}\right)^{-1} dE\,, \tag{2.12}$$

where

I_0 = beam current

z_{proj} = charge state of the incident particle

e = electron charge

N_a = Avogadro number

A = atomic mass of the target element

E_{in}, E_{out} = energy of the beam hitting the target and the one leaving the target after traveling through its thickness, respectively

$\sigma(E)$ = production cross section for the nuclide

ρ_t = target density

dE/dx = stopping power of the projectile in the target, calculated with the Bethe-Bloch formula [23].

Once the rate given in eq. (**2.12**) for all the radionuclides of interest is calculated (the main and its contaminants), the time evolution of the number of nuclei, and hence the activity of a specific radionuclide can be obtained, during and after the irradiation. By solving numerically the generalized Bateman equation for decay chain

$$\frac{dN_i(t)}{dt} = R_i - \lambda_i N_i(t) + \sum_{j<i} f_{ij}\lambda_j N_j(t) \qquad (\mathbf{2.13})$$

where

$N_i(t)$ is the number of nuclei of species i produced at time t,

λ_i the decay constant,

f_{ij} the branching ratio from j to i.

Its solution gives the time evolution of $N_i(t)$.

By introducing

$$A_i(t) = \lambda_i N_i(t) \qquad (\mathbf{2.14})$$

as the activity produced by radionuclide i and during an irradiation time t, the integral yield is defined as

$$y_{EoB} = \frac{A(T_{EoB})}{I}, \qquad (\mathbf{2.15})$$

where T_{EoB} is the time at the End of Bombardment and I is the beam current.

Finally, the isotopic (IP) and radionuclidic purity (RNP) are calculated as:

$$IP = \frac{n_{main}}{\sum_i n_i}, \qquad (\mathbf{2.16})$$

where n is the number of nuclei for each i radionuclide and *main* refers to the radionuclide of interest.

$$RNP = \frac{A_{main}}{\sum_i A_i} \tag{2.17}$$

where A is the activity for each i radionuclide and *main* refers to the radionuclide of interest.

In view of pre-clinical and clinical applications it is crucial to find a reliable production route, which guarantees a sufficient and high-quality production in compliance with the medical standards. The European Pharmacopoeia, that is a Commission that consists of 47 members, establishes the requirements a radiopharmaceutical must satisfied to be employed in medicine. However, the research on radiopharmaceuticals is still dynamic and constantly in progress, such that new promising compounds are currently under investigation. The rules about their eligibility are not strict, due to the lack of complete information and the difficulty in defining a general indication that fits all. Depending on the nature of the compounds, categories are identified and for each guidelines are promoted. In general, the reference limits one must considers are the RNP and the dose increase (DI). The control and the limitation of the fraction of radionuclidic impurities is a pivotal part of the demonstration that a specific route is promising for the production of a medical radionuclide, however it is not enough. In fact, it is essential to quantify also the increase of the radiation dose deposited in tissues due to the presence of these impurities. Thus, the production methods must generate a minimal amount of radioisotopes to keep the presence of impurities at as low as acceptable levels [53]. In general, the radionuclidic impurities limit is usually expressed as a percentage and from a pharmaceutical/good manufacturing practice (GMP) viewpoint it should be set lower than 1%. Therefore, according to the recommendation the RNP should be above 99%. However, it is possible to accept a lower RNP, if and only if the percentage of the co-produced impurities is not the cause of an increase of the dose to the patients' organs, guaranteeing a safe clinical application. Therefore, the assessment of the dose increase is the most rigorous condition to be verified. There is no fixed limit for the

DI, however an increase of max 10% is the utmost acceptable risk for the scientific community. Hence, a RNP below 99% is allowed if the DI is maintained below the 10% limit. This is why it is important to accurately consider the effect of the presence of the contaminants on the final product. The fraction of co-produced contaminants characterizes the production route, precisely it is the right combination projectile-target that leads to the optimal production, namely to a negligible contamination. Even though in the case of enriched targets the expected amount of contaminants is small, it cannot be completely excluded depending on the purity of the sample. Thus, dosimetric studies are fundamental to evaluate the impact of the produced radionuclides in terms of dose released to the patient, including the contribution of the contaminants. In this thesis, the dosimetric calculations will be carried out by using the software code OLINDA (Organ Level Internal Dose Assessment), in which the activities previously calculated from yields become the input. The evaluation of the dose imparted by the investigated radionuclides allows determining the best balance between activity and purity and to identify the time window after the End of Bombardment, i.e. the end of the target irradiation for the production of the radionuclide, to label a radiopharmaceutical product with an acceptable DI to the patient.

Biodistribution data are the first step to assess the dosimetric implication. Starting from experimental measurements on mice the information is translated to the human models by means of appropriate scaling methods, which take into account the differences in human and animal organ masses compared to the total body masses. After the administration of the radiopharmaceutical the deposited activity in the animal's organs is measured directly or indirectly, namely through organs explantation or imaging. The activity concentrations in the different animal source organs (blood, lung, spleen, kidneys,stomach, intestines, liver, salivary glands, muscle and bone) is reported as per cent of injected activity per gram of tissue ([%IA/g] A) and then scaled from mice to adult humans to obtain the decay-corrected per cent of injected activity for each human

source organ ([%IA/organ] H) through the following scaling formula:

$$\left(\frac{\%IA}{organ}\right)_H = \left(\frac{\%IA}{g}\right)_A \left(\frac{OW_H}{TBW_H}\right) TBW_A \qquad \textbf{(2.18)}$$

where OW_H is the human organ weight and TBW_A and TBW_H are the average total body weight for animal and human, respectively. OW_H and TBW_H values were obtained from the adult male phantom implemented in the OLINDA software code version 2.2.0 [54, 55], based on the RADAR method for internal dose estimation [56] and the NURBS-type Adult Male and Female models [57], based on the standardized masses defined by ICRP 89 [58]. Biodistribution data were then plotted as a function of post injection (p.i.) time and fitted by a tri-exponential equation, representing the phase of accumulation and the possibility of both a fast and a slow elimination of the radiopharmaceutical, with CoKiMo (Compatmental Kinetic Model) software. At last, the number of disintegrations per unit of administered activity in the source organs was obtained by integration of organ activity curves for each radioisotope, considering its physical half-life. These data were then used as input values in an adult male and/or female phantoms to perform dosimetric calculations with the OLINDA software code, obtaining the organ absorbed doses per unit of administered activity. Considering Scandium as the example, for each ^{xx}Sc radioisotope, the effective dose coefficient, $ED^{^{xx}Sc}$ (mSv/MBq), is obtained as the sum of the product of the organ equivalent dose per unit of administered activity, $D_{organ}^{^{xx}Sc}$ (mSv/MBq), and the respective tissue-weighting factor, w_{organ}, recommended by ICRP 103 [59],

$$ED^{^{xx}Sc} = \sum_{organs} D_{organ}^{^{xx}Sc} \times w_{organ}\,. \qquad \textbf{(2.19)}$$

Afterwards, the total effective dose coefficient (ED_{tot} expressed in (mSv/MBq)), including the contribution of each ^{xx}Sc radioisotope, is calculated at the different

times after EoB, as

$$ED_{tot}(t) = \sum_{xx} f_{^{xx}Sc}(t) \times ED^{^{xx}Sc} \quad \textbf{(2.20)}$$

where $f_{^{xx}Sc}(t)$ is the fraction of total activity corresponding to each radioisotope at the time t after EoB, $A_{^{xx}Sc}(t)$.

Finally, the evaluation of the DI due to the presence of radiogenic impurities in the production route is introduced according to the following equation

$$DI(t) = \frac{ED_{tot}(t)}{ED^{^{47}Sc}}, \quad \textbf{(2.21)}$$

and represents the ratio between the total effective dose (*i.e.*, including the impurities) and the effective dose due to an ideal injection of pure ^{47}Sc.

Chapter 3

Scandium

3.1 Background

Scandium has acquired a great interest in nuclear medicine applications as an ideal theranostic radiopharmaceutical. On the basis of the physical and chemical characteristics of the scandium radionuclides it is possible to produce pairs suitable for both diagnostic and therapeutic purposes. Specifically, ^{47}Sc ($T_{1/2}$ = 3.35 d) is adequate for targeted radionuclide therapy and SPECT imaging, since it is a β^- and γ-emitter, respectively. The ground state of ^{44}Sc ($T_{1/2}$ = 3.891 h) and ^{43}Sc ($T_{1/2}$ = 3.97 h) are instead β^+-emitters, suitable for PET scans. In table 3.1 the decay characteristic of the Sc-isotopes of interest are listed.

Isotopes	Half-life	β^+ $E_{average}$ [KeV] (I)	X and γ [KeV] (I)	β^- $E_{average}$ [KeV] (I)
^{47}Sc	3.35 d	-	159.38 (68.3%)	162 (100%), 441 (68%), 600 (32%)
^{43}Sc	3.9 h	476 (88.1%)	372 (23%)	-
^{44}Sc	4.0 h	632 (94.27%)	1157 (100%)	-

Table 3.1 Decay characteristics of Scandium isotopes suitable for theranostics [1].

In nuclear medicine distinct practises require the use of specific radionuclides depending on the nature of their emitted radiation. Distinct radionuclides might be inserted in diverse chemical scaffolds to build a radiopharmaceutical agent, whose kinetic and biodistribution depends precisely on its chemical structure. For the theranostics purposes the efficacy of a therapy is verified in advance by a prior imaging scan. For this reason the matched pairs ^{44}Sc/^{47}Sc and ^{43}Sc/^{47}Sc represent an attractive and valid alternative as PET/therapy radiopharmaceutical to the pair ^{68}Ga/^{177}Lu, currently used in clinics. The use of pairs belonging to the same chemical element, and hence with the same biodistribution, has the advantage of visualizing the uptake of the drug on the sensitive target through an image and, if enough, of assuring the effectiveness of the treatment beforehand, since the exact same target is expected to be reached. Similar and not identical chemistry, like for the ^{68}Ga/^{177}Lu case, might lead to different and less precise outcomes.

In addition, the stable coordination of Scandium with the chelating agent DOTA makes ^{47}Sc adequate at labelling DOTA-derivatized biomolecules that are currently available in diagnostics. This could represent a valid vehicle also for future applications as theranostic agent. The DOTA-folate conjugate cm10 labelled with ^{47}Sc, ^{47}Sc-cm10, is the Sc-complex better described in the Literature [60, 61]. It consists of three parts: a targeting vector folic acid, which is able to selectively bind to the folate receptor that is expressed on a variety of tumour types; the chelating agent DOTA; and a small-molecular weight albumin, which improves the blood circulation time and tissue distribution profile of folate conjugates. At a preclinical level, the therapeutic potential of ^{47}Sc-cm10 has been proven by Müller et al [60] and Siwowska et al. [61]. In diagnostics, SPECT/CT imaging demonstrates a high localization in the tumour site and from there detailed ^{47}Sc-cm10 biodistribution data have been derived. The information is the starting point to calculate kinetics data necessary to assess the effective dose produced by the specific radiopharmaceutical. Although the valid preclinical results, the translation of ^{47}Sc-therapeutic agents to the clinic has been hindered by the limited availability of ^{47}Sc itself in the market. New and effective production methods to satisfy the high demand are needed.

Currently, the ^{47}Sc production methods include the use of both nuclear reactors and particle accelerators [62], although none is adequate to meet the medical standards required for a safe clinical practise.

At present, ^{47}Sc is produced by neutron-induced reactions by means of nuclear reactors, mainly from enriched Ti or Ca targets, with a sufficiently high RNP. Specifically, the reaction ^{47}Ti(n,p)^{47}Sc requires fast neutrons (E > 1 MeV) to produce ^{47}Sc, while in the case ^{46}Ca(n,γ)^{47}Ca $\rightarrow$ ^{47}Sc thermal neutrons are necessary. With enriched Ti targets it is possible to obtain high yield if high flux and thick targets are used. Regarding the second method, the abundance of ^{46}Ca in ^{nat}Ca is only 0.004% so the cost of the enriched target represents a limitation. In addition, the cross section of the reaction is not that high [63].

Nevertheless, the limited number of nuclear reactors and need of expensive enriched material, moves the interest also to cyclotron-based production routes [64]. A more

affordable production method must go hand in hand with the quality and the amount of the production itself when medical applications are the final goal. This means that the new routes of production must satisfy the medical standards to be considered as valid alternative and/or a complementary option to the already existing ones. Other examples of ^{47}Sc production entail the photonuclear reactions, where an electron beam from a linear accelerator hit a Tungsten (W) target and produces a bremsstrahlung radiation that is used to irradiate an enriched Ti or Ca target. In the first case ^{47}Sc is produced through a the direct reaction ^{48}Ti(γ,p)^{47}Sc [65], in the second case by the indirect reaction ^{48}Ca(γ,n)^{47}Ca $\rightarrow$ ^{47}Sc (neutron knockout) [66, 67]. In the direct reaction with ^{nat}Ti targets the co-production of ^{46}Sc and ^{47}Sc is expected. The use of enriched ^{48}Ti targets allows to diminish, if not completely eliminate, the co-production of ^{48}Sc. However, the ^{48}Ti(γ,pn)^{46}Sc reaction threshold is 22 MeV and peaks at 35 MeV. Therefore, even with an enriched target, ^{46}Sc is produced unless the beam energy is kept below its threshold [68, 69]. For the generator ^{47}Ca/^{47}Sc, a optimum ^{47}Ca production method requires a highly enriched ^{48}Ca target and a high-power 40 MeV electron linac. In general, these channels of production have an issue related to their low yield, due to the little interaction of the photons with the matter. To overcome such hindrance longer irradiation time or expensive target of large mass should be considered. In spite of that, one more production route involving photons is quite attractive. High-purity and carrier-free ^{47}Sc can be produced by irradiating ^{nat}V targets using electron linear accelerators [70]. The use of ^{nat}V, thanks to its low cost and wide availability is advantageous over the enriched Ti and Ca targets. The reaction ^{nat}V(γ,α)^{47}Sc, considering a photon energy of 20 MeV, produces extremely high-purity ^{47}Sc (>99.998% pure) at EoB. The co-production of ^{49}Sc occurs and dominates at higher energies. However, it can be easily eliminated after few hours of cooling, since its shorts half life of 57.3 min.

The production of ^{47}Sc by means of cyclotrons represents an interesting alternative method. At present, several nuclear reactions have been investigated, in consideration of the possibility to irradiate a target with different particles, such as α, deuterons, and protons. In the case of α beams, the production route ^{44}Ca(α,p)^{47}Sc has been analysed with scarce results in terms of both yield and RNP. Neertheless, for small scale studies

with ^{47}Sc the ^{44}Ca(α,p)^{47}Sc reaction might be convenient due to the short range of α projectiles in Ca-target, allowing the use of a relatively small amount of ^{44}Ca target material [62, 71].

When protons are the projectile different targets are suitable for the ^{47}Sc production, namely ^{48}Ti, ^{48}Ca, and ^{nat}V. The proton induced reaction ^{48}Ti(p,2p)^{47}Sc [72] has instead the downside of the production of the main contaminant ^{46}Sc, that could be the reason of an increase of the dose to the patients due to its characteristic γ emission. The co-production of contaminants represents one of the biggest issue in the context of radiopharmaceuticals. As the projectile energy increases more and more radioisotopes can be produced and this leads to a contamination that could affect the purity of the production, since the chemical purification is not effective when isotopes are involved.

The nuclear reaction ^{48}Ca(p,2n)^{47}Sc [73] is interesting in the energy range 17 –24 MeV, since the ^{47}Sc cross section, that peaks at 20 MeV, is large and a smaller production of the main contaminants, ^{46}Sc and ^{48}Sc, is expected. In fact their peaks occur at 33 and 11 MeV, respectively. However, the natural abundance of ^{48}Ca is only 0.187%, thus the feasibility of this production route depends on an extremely highly-enriched and high-cost target.

Regarding the nuclear reaction ^{nat}V(p,x), protons of intermediate energy are required to activate the channel for the ^{47}Sc production. Experimental measurements and theoretical analysis have been carried out within the framework of the PASTA research project (Production with Accelerator of ^{47}Sc for Theranostic Applications), funded by INFN National Laboratories of Legnaro (INFN-LNL) [74]. The study demonstrates that this production route is of particular interest. The nuclear cross section of the ^{nat}V(p,x)^{47}Sc reaction is quite low (approximately 12 mb at about 35 MeV) and a proton beam of energy below 35 MeV is necessary to maintain as low as possible the amounts of other Sc-isotopes co-produced [75, 76]. In addition, the low-cost of the commercially easily available ^{nat}V targets (isotopic composition: 0.250% of ^{50}V and 99.750% of ^{51}V) and the significant world-wide diffusion of medium energy proton cyclotrons, about 40 according to the IAEA database of cyclotrons for radionuclide production [77], makes this reaction a valid alternative.

Concerning the deuteron-induced reactions the use on both natural and enriched Titanium targets are considered, namely ^{nat}Ti(d,x)^{47}Sc, ^{50}Ti(d,αn)^{47}Sc, ^{49}Ti(d,α)^{47}Sc, ^{48}Ti(d,x)^{47}Sc and ^{47}Ti(d,2p)^{47}Sc. For all these routes the threshold that activates the channel related to the ^{47}Sc production is at low energies that makes these reactions suitable for hospital cyclotrons. In the reference by Pupillo et al. [78] a list of these deuteron-induced reactions is presented in more details. Other nuclear reactions like, ^{48}Ca(d,3n)^{47}Sc and ^{46}Ca(d,n)^{47}Sc, are interesting routes since their threshold energy for ^{47}Sc is below 10 MeV and well separated from the ^{46}Sc one. However, these cross sections have not been measured yet. Lastly, another compelling reaction is ^{nat}V(d,x)^{47}Sc, for which the ^{47}Sc cross section starts at 25 MeV and reaches its peak at around 40 MeV, but the contamination by ^{46}Sc can be avoided only for deuterons energy lower than 30 MeV [79].

So far all the ^{47}Sc production methods entail a co-production of other radioisotopes that are responsible for a reduction of the level of purity, depending on the amount of contaminants generated from the specific route. Since the wide interest in the ^{47}Sc radionuclide as a theranostic-agent and the lack of a reliable production route which guarantees a sufficient quantity and purity of the radionuclide, many laboratories are actively participating in current researches to find an efficient production route.

To this purpose, my contribution on this is specifically devoted to a theoretical study of the reactions: ^{49}Ti(p,2pn)^{47}Sc, ^{49}Ti(d,α)^{47}Sc, and ^{50}Ti(p,α)^{47}Sc. The aim is to verify the feasibility of these cyclotron production routes, identifying the optimal irradiation conditions and parameters that allow to limit the contamination in aid of a high purity. The relevance of the theoretical evaluations is manifest. Information such as the type of particle, the energy of the beam, the threshold energy that activates the contaminants' channels are just some of the key hints to guide the experiments. Since the higher purpose of applications in nuclear medicine, to predict in advance if a production reaction complies the clinical standards is valuable.

3.2 The nuclear reaction ^{49}Ti(p,2pn)^{47}Sc

The reaction ^{49}Ti(p,x) for the production of ^{47}Sc has been investigated on the basis of two different approaches, namely the statistical evaluation of the TALYS models that describes the nuclear mechanisms and an optimization method related to the nuclear level density. The common line is the simulation of the cross section by means of the nuclear reaction code TALYS, which is actively developed and maintained. The aim of the authors is to provide a complete and high quality set of models [35] for the different reaction mechanisms that are relevant in the energy range of medical interest, namely, nuclear scattering, compound nucleus formation, and preequilibrium emission. Specifically, for the reaction with protons on enriched ^{49}Ti targets the TALYS version 1.95, which includes the latest pre-equilibrium model, the geometry dependent (GDH) model, has been used. TALYS describes the nuclear reaction mechanisms on the basis of 5 pre-equilibrium models (PE) and 6 level density models (LD), for a total of 30 possible combinations of models. The standard simulation commonly used in Literature, TALYS default (PE2-LD1), does not exploit the potentiality and versatility of the code and it is not always a representative solution. Alternative options have been introduced, like for example the so-called "TALYS adjusted" configuration [80], often used as a replacement of the default option. However, also this case relies on the selection of a single model for level density and pre-equilibrium. For a comprehensive analysis the variability of the models is an essential aspect to be considered. For this reason a statistical dispersion analysis is here performed by defining an interquartile range, between Q1 and Q3, that includes the 50% of the models involved, and taking the centre of this band as the most representative value, simply defined as the centerline.

Fig. 3.1 shows the ^{47}Sc cross section of the p-^{49}Ti reaction. The gray band represents the models variability, the dashed lines are the minimum/maximum values of the cross sections obtained with all models. This representation of the cross section can be seen as an extension of the standard box-whiskers plot used in descriptive statistics to the continuum of the models. However, instead of considering the median of the plot as the baseline, the reference value is the centerline of the band. The data from the Dominicis et al. are the preliminary results of the REMIX project [19] and they are the very first

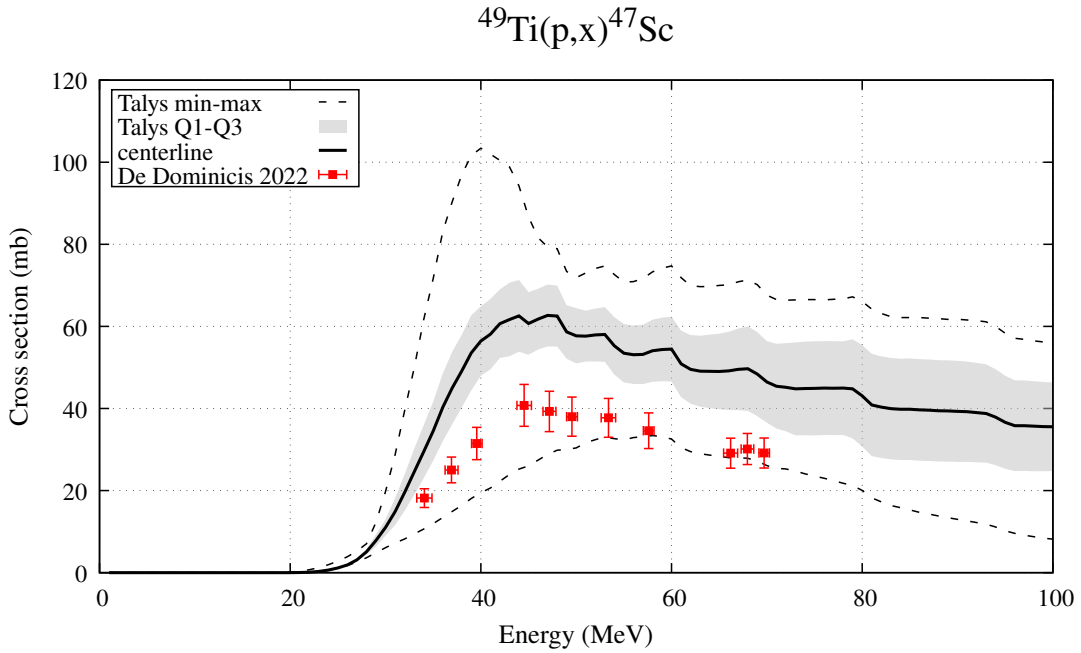

Figure 3.1 ^{47}Sc cross section for the reaction ^{49}Ti(p,x).

experimental measurements available in Literature for this reaction. The collaboration among the theoretical and the experimental group has been essential to achieve this goal. Indeed, the theoretical analysis of cross sections for the production ^{47}Sc has been crucial to efficiently guide the experimental activities. The advantage of supporting the experiments with an upfront modelling guarantees a good predictive capability. Conversely, new measurements are the key ingredient to validate the theoretical models and to optimize the models' free parameters. In this case, the data falls in the lower part of the TALYS band. The trend suggested by the models seems to be reproduced by the data, but the cross section is underestimated if the centerline is the reference.

The analysis of the contaminants concerns mainly the evaluation of ^{46}Sc and ^{48}Sc cross sections, as illustrated in Fig. 3.2 and 3.3. The reasons why these radionuclides are responsible for a possible contamination of the production are the long half-life of ^{46}Sc ($T_{1/2}$= 83.79 d) with respect to the ^{47}Sc one, and the co-production of ^{48}Sc ($T_{1/2}$= 43.67 h) that overlaps the ^{47}Sc optimal energy range of production. For both cases two datasets are available, Levkovskij measurements refers to the production at low energies, while De Dominicis [81] energy range spans from 30 to 70 MeV. Data from Levkovskij [82] have been normalized to a factor 0.8, due to the revaluation

of the monitor values [83–85]. Considering ^{46}Sc cross section it is evident that the black data are in correspondence of the maximum of the models, while the red ones are well reproduced. The ^{48}Sc case shows a general good agreement among theory and experiments. The change in the cross section behaviour is clear, a steep rise well depicted by the black data, and a smooth increase after 25 MeV.

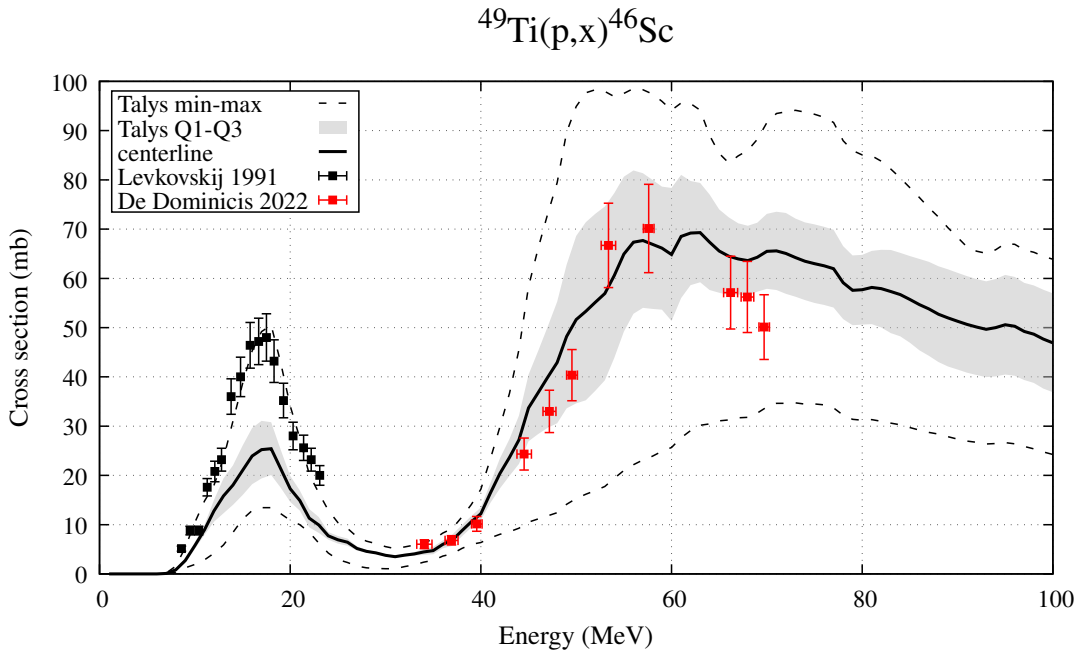

Figure 3.2 ^{46}Sc cross section for the reaction ^{49}Ti(p,x).

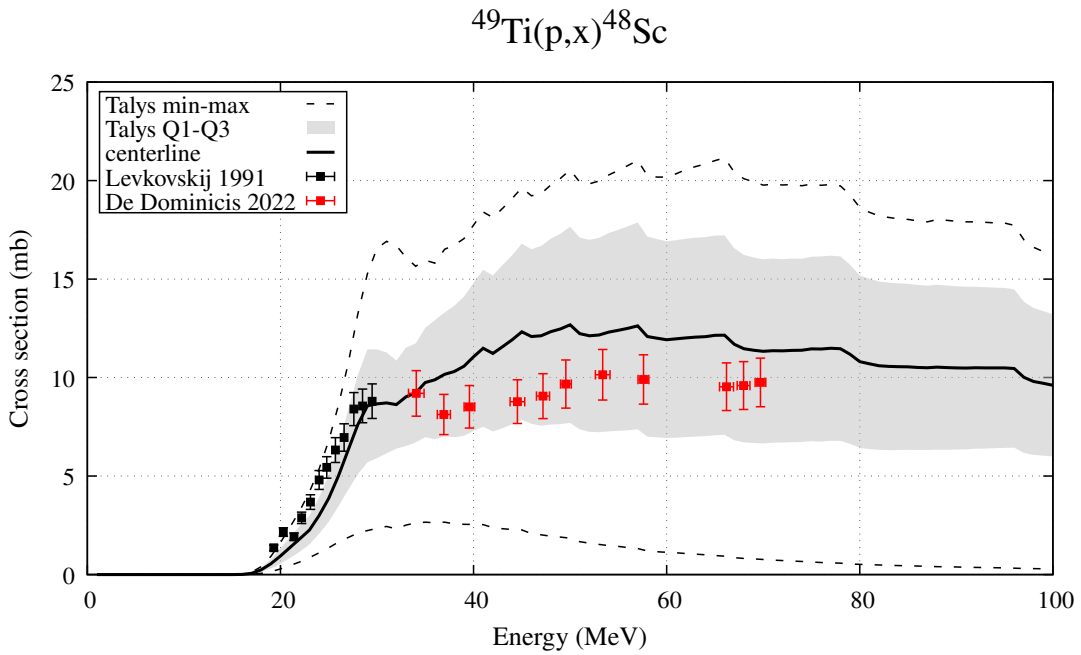

Figure 3.3 ^{48}Sc cross section for the reaction ^{49}Ti(p,x).

3.2.1 Cross sections analysis with the REMIX enriched ^{49}Ti target

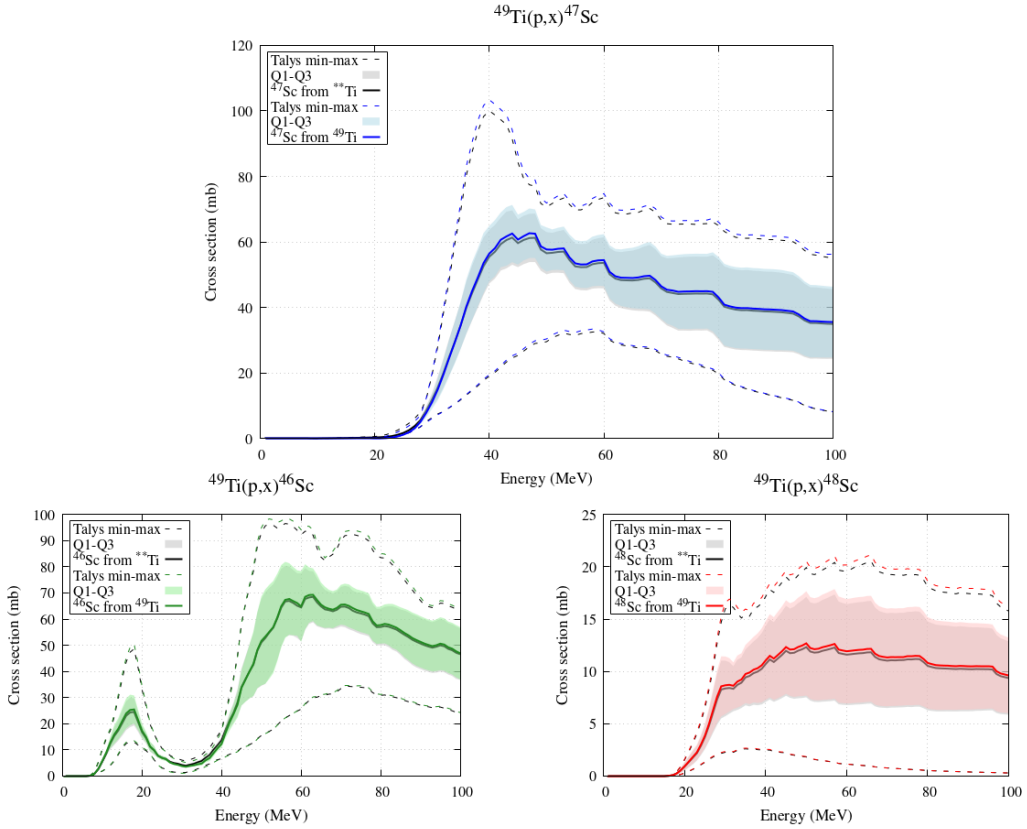

Figure 3.4 Comparison of the ^{47}Sc, ^{46}Sc, and ^{48}Sc cross sections considering a 100% enriched ^{49}Ti target and the isotopic composition of the target used for the REMIX experiment.

It should be noted that the statistical analysis has been conducted considering a 100% enriched ^{49}Ti target. However, the isotopic composition of the target utilized for the REMIX measurements is the following: 0.22% of ^{46}Ti, 0.22% of ^{47}Ti, 2.71% of ^{48}Ti, 96.25% of ^{49}Ti and 0.60% of ^{50}Ti. Figure 3.4 compares the theoretical cross sections of ^{47}Sc, ^{46}Sc, and ^{48}Sc, considering a ^{49}Ti 100%-enriched target and the REMIX one. For all radionuclides the lines related to the ideal target are faintly higher. Therefore, considering one target over the other does not alter the cross sections and since no significant changes are observed, we have limited the analysis to the 100% enriched ^{49}Ti target.

3.3 Optimization

The statistical analysis turns out to be a good method to investigate the modelling of the reaction and verify the agreement between data and theory. The approach reveals

the overall trend of models and the model dispersion one has to expect. For this particular reaction the model variability is quite large by observing the width of the interquartile band or the large difference between the min-max dashed curves. The next step consists in finding a good reproduction of the cross sections, closer to the new experimental data that have been measured. To achieve this goal it is possible to exploit the flexibility that the code TALYS offers in the HFM. The three models based on the HFM approach [86] represents somehow the time evolution of the TALYS code with respect to the microscopic level density models. They complement each other describing different level-density aspects of reaction mechanisms, globally adapted to suite the entire nuclide chart. Each option provides different tabulated level densities and the code allows one to overrule them to improve the agreement with data within a restricted Z and A range. The three different tabulated options one can refer to are: ldmodel 4, the microscopic level densities from Goriely's tables (Skyrme force), ldmodel 5, the microscopic level densities from Hilaire's combinatorial tables (Skyrme force) [48], and ldmodel 6, the microscopic level densities from Hilaire's combinatorial tables (temperature dependent HFB, Gogny force) [50]. The level densities are tabulated at different excitation energies for both parities and different values of spins. TALYS allows to rescale the values in these tables to the purpose of fitting experimental data.

In general the original HFM microscopic level densities have not been adjusted to experimental data and the tabulated values can be scaled according to the transformation

$$\rho(E,J,\pi) = exp(c\sqrt{E-p})\rho_{HFM}(E-p,J,\pi) \tag{3.1}$$

where ρ is the level density, ρ_{HFM} the HFM microscopic level density, E is the energy, J the spin and π the parity. The optimization procedure applied in this work to find the best values of c and p implies two steps. In the first place a grid search, that is a visual inspection of the resulting cross sections accordingly a rough variation of the level density parameters, and secondly a fine tuning of the parameters by means of specific optimization methods. The two parameters c and p are allowed to vary in the

range [-10, 10] [42, 52]. However, the search of the parameters has been restricted within a narrower interval to be more conservative and perturb the cumulatives the least possible. It is worth noting that the variation of the *c* and *p* parameters was not intended for a good description of nuclear level cumulatives (to wit: the number of levels from ground state to a given excitation energy, N(E)). Rather, it has been carried out to optimize the agreement with the experimental cross section, since this is crucial for more accurate estimates of yields and purities in view of the specific application in nuclear medicine described in this thesis.

The practical aim of the study demands a model description of cross sections as close as possible to the experimental data, since many quantities, such as yields, RNP, and DI, are needed with high accuracy for the multidisciplinary evaluation of the production route. The better the reproduction of the cross section the better the prediction of the subsequent calculations, namely the amount of radio-pharmaceutical compound that can be produced in view of preclinical and clinical trials and the evaluation of the dosimetric impact to the patient's organs. In view of the specific nuclear medicine applications we have in mind, a good reproduction of the relevant cross sections is crucial at the point to justify a certain compromise with the overall theoretical consistency of models. For this reason we have adjusted the NLD parameters throughout an optimization procedure. To achieve the most accurate parametrization a specific TALYS microscopic model has been selected and a set of values for the c and p parameters to fit the experimental cross sections has been found. In particular, for the reaction ^{49}Ti(p,x) for the pre-equilibrium model the Talys option pe 5 has been considered. Regarding the level density model the option denoted as ldmodel 4, that refers to the Goriely tables, has been identified as the most appropriate for the reproduction of the cross sections. This means that, through a visual inspection of the most relevant cross sections (^{47}Sc and main contaminants) the curves are close enough to data to entail a variation of the model free parameter as small as possible. In table 3.2 the nuclides considered as compound nucleus are listed. It is worth to notice that the solution reported is not necessarily unique: it is not possible to exclude that another set of parameters (related for example to a different optical potential, preequilibrium, or nuclear level density model) could reproduce the data with a similar accuracy. This

would still be in the spirit of this paper, i.e., to improve the theoretical description of the cross sections of medical radioisotopes and contaminants for radiopharmaceutical applications.

Isotope	c	p
^{46}Sc	0.2	0
^{47}Sc	0	1
^{48}Sc	-0.2	-1
^{48}V	0	-1
^{44}Sc	0.4	0
^{43}Sc	-0.4	2

Table 3.2 Optimized c and p parameters used for the nuclear reaction ^{49}Ti(p,x).

To summarize, the modification of the *c* and *p* parameters of the nuclear level density following the transformation **3.1**, allows to improve the reproduction of the experimental cross sections. However, this optimization procedure is a rough variation of *c* and *p* based on a visual esteem of the cross sections and considering one radionuclide at a time as the compound nucleus. To further refine the reproduction of the cross section another approach has been investigated. By utilizing the genetic algorithms (GA) commonly used to generate high-quality solutions to optimization and search problems by relying on biologically inspired operators, new optimized curves have been obtained. Hence, the optimization procedure consists of two steps: an approximately improvement of the cross sections based on a visual survey followed by a finer tuning through GA. The first level of optimization, although rough, represents a useful step. Indeed, the set *c* and *p* parameters identified at that stage are a hint for the GA, such that they become the chromosomes of the GA initial population. The next paragraphs are focused on the description of this evolutionary algorithm and on the discussion of the results for the production route ^{49}Ti(p,)^{47}Sc.

3.3.1 Genetic Algorithm

In the recent years, metaheuristic algorithms are used to solve real-life complex problems arising from different fields such as economics, engineering, politics, management, engineering, and physics. These algorithms are broadly classified into two categories, namely single solution and population based metaheuristic algorithm. The former case utilizes and improves the single candidate solution by using local search. The main drawback of this method is the possibility to end up in local optima.

Population-based metaheuristics utilizes multiple candidate solutions during the search process. This approach maintains the diversity in a population and avoid the solutions to be stuck in local optima. GA are an example of well-known population-based metaheuristic algorithms [87]. The pioneer of GA is John H. Hollande, who proposed them in 1992. These algorithms are numerical optimisation methods inspired by the biological evolution process of the Darwinian theory, according to which only the fittest in nature survives. In this context that mimics the natural selection, a potential solution to a problem is represented as a set of parameters, namely the genes, joined together to form a string of values, referred to as chromosomes. Chromosomes are considered as points in the solution space. A set of chromosomes, each representing a possible solution to a given problem, form a population of individuals. The starting population is initialized randomly and the new populations are produced by iterative use of biological-inspired operators on individuals present in the population. The basic elements of GA are the chromosome representation, the selection, the crossover, the mutation and the fitness function. Several are the possibilities to be adopted for all the above mentioned operators and Fig. 3.5 summarizes the commonest ones.

3.3.2 Encoding

The encoding is basically the representation of the chromosomes, that can be binary, octal, hexadecimal, permutation, value-based, and tree. In the ordinary used binary encoding each chromosome is represented as a string of 1 or 0 and each bit depicts the characteristics of the solution. This coding scheme has the advantage to fast the implementation of crossover and mutation operators. However, it might require extra effort to perform a conversion into the binary form. In the octal encoding scheme, the chromosome is embodied in the form of octal numbers, i.e. 0–7, while when the coding is hexadecimal the hexadecimal numbers are utilized, that are 0–9 or A-F. To solve ordering problems the permutation encoding scheme is generally used. In this instance the chromosome denotes a string of numbers representing the position in a sequence. In the value encoding scheme chromosomes consist of a string of some values. These values can be real, integer number, or character. This encoding option

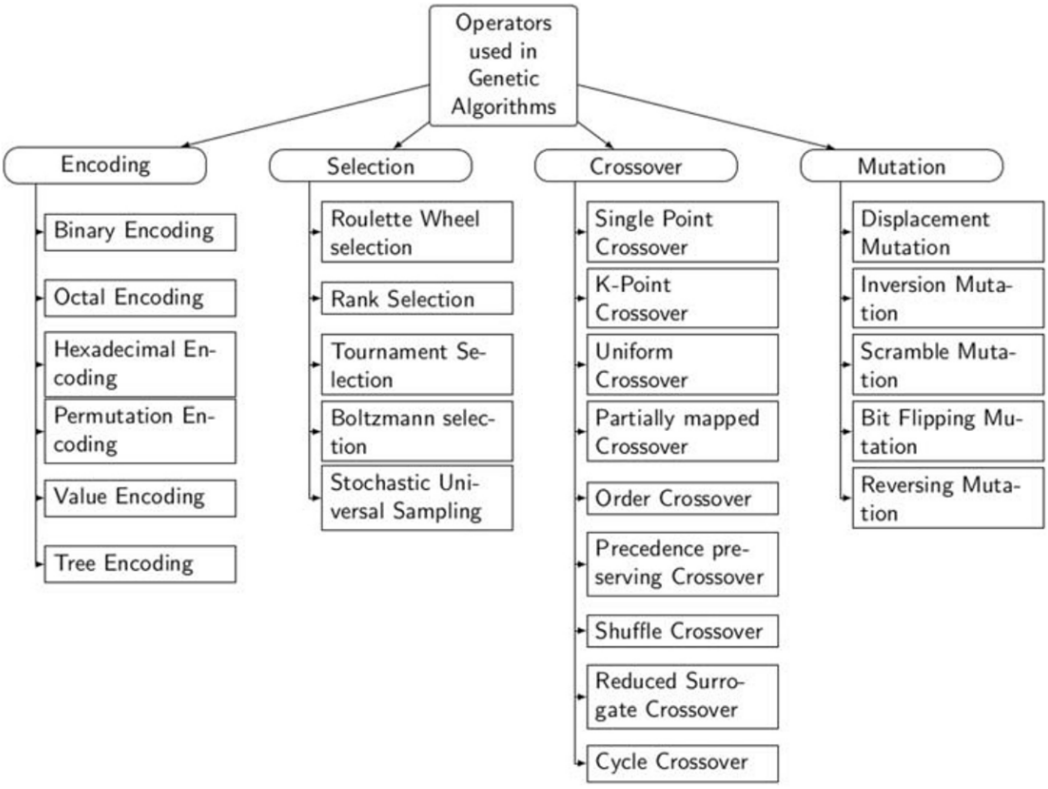

Figure 3.5 Diagram of the possible operators used in GA.

is useful in solving the problems in which more complicated values are involved, that might be difficult to handle with the binary representation. The value encoding refers to the one employed in this work. A classical example of applications are the neural networks for finding the optimal weights. In tree encoding, the chromosome is a tree of functions or commands related to any programming language.

3.3.3 Selection

Selection is a key step in GA that determines whether a particular chromosome will participate in the reproductive process or not. Indeed, selection attempts to apply pressure upon the population in such a way similar to the natural selection of biological systems. The GA emulates the process of evolution in which the strongest elements survive while the weakest ones are discarded. This means that the fitter individuals have a greater chance to be selected for the generation of the offspring which inherit the characteristics of the parents and then they will be added to the next generation. The poorer performing individuals are rejected instead. This process keeps iterating and in the end a population made of the fittest is found. It is to be noted that the

convergence rate of GA depends upon the selection pressure. Good parents drive to a better and fitter solution. However, to prevent one extremely fit solution from taking over the entire population in a few generation, it is crucial to maintain diversity in the population. A premature convergence leads to the solutions to be close to another in the solution space at the expense of the diversity. Among the selection techniques there are roulette wheel, rank, tournament, Boltzmann, and stochastic universal sampling. The first two options are based on the concept of the fitness proportionate selection. The core idea is that every individual can become a parent according to a probability proportional to its fitness. The fitter individuals have a higher chance of mating and propagating their features to the next generation. Starting from a circular wheel, n individuals are considered and each of them gets a portion of the wheel proportional to its fitness score, that is the higher the pie the higher the chance. Two implementation are possible: the roulette wheel selection and the stochastic universal sampling. The former consists of a fixed point chosen on the wheel. Then the wheel is spinned and the region of the wheel that stops in front of the fixed point corresponds to the choice of the first parent. The same process is repeated for the second parent. In the latter selection all parents are chosen in a single spin of the wheel, since the fixed points on the wheel are multiple. The tournament mode selects k random chromosomes and picks the best out of these k to become the parents. Again, the same process is repeated for selecting the next parent. The rank selection is helpful when using the roulette wheel selection is not the best option. This happens for example at the end of a run, when the individuals in the population have very close values of fitness, so they have almost an equal pie in the wheel, that means an equal probability of being selected as a parent. On account of this, every individual is ranked according to their fitness so their selection depends on their rank and not their fitness. The higher-ranked individuals are preferred. A Boltzmann selection is based on entropy and sampling methods in Monte Carlo simulation. It naturally leads to adaptive fitness in which the fitness function does not stay fixed but varies with the environment. Another method for selection is the steady state selection, in which only few individuals are replaced at a time. The population size remains steady because instead of adding the offspring into the next generation, the two best individuals out of the two parents are added back into the population, namely if offspring are better than the worst solution the worst individuals

are replaced with the new offspring, such that the population remains constant.

3.3.4 Fitness function

The fitness function determines how fit an individual is. It expresses the ability of an individual to compete with others, transforming that measure of performance into an allocation of reproductive opportunities. For this reason the fitness function is the driving force of an algorithm. Basically, giving a fitness score to each chromosome at every iteration, it is possible to identify the fittest ones that will be selected for the further processing of reproduction.

3.3.5 Crossover

Crossover operators generate the offspring by combining the genetic information of two chromosomes of the current generation, identified as parents. In the crossover procedure some of the genes from one chromosome are interchanged with the genes fro the corresponding positions in the other one. This process produces two new chromosomes, the offspring. The crossover operators are single-point, two-point, k-point, uniform, partially mapped, order, precedence preserving crossover, shuffle, reduced surrogate and cycle.

In a single point crossover, a random crossover point is selected and the genetic information of both parents that is located beyond that point is swapped with each other. In a two point and k-point crossover, the selection of two or more random crossover points defines segments of genes from parents that will be swapped.

In a uniform crossover each gene from both parents are treated separately. The swap between genes that occupies the same location in different parent chromosome occurs randomly.

Partially mapped crossover is an operator proposed by D. Goldberg and R. Lingle in 1985. In this case to produce the offspring two different cut points are randomly determined and the genetic material between these two reference points that belongs to one parent is replaced with the corresponding part of the other parent. The left out

alleles are copied from the second parent. However, if the same genes are found among the copied genes, they are changed.

Order crossover was proposed by Davis in 1985. Random cut-points are selected in the first parent and the genetic segments are copied to produce a proto-child. To complete the sequence of the offspring the remaining missing genes of the first parent are then transferred, but in the order in which they appear in the second parent.

Precedence preserving crossover preserves the ordering of individual solutions as present in the parent of offspring before the application of crossover. The offspring is initialized to a string of random values that decides whether the individuals from both parents are to be selected or not.

For the shuffle crossover a single crossover position is chosen. However, before performing the crossover, the variables are randomly shuffled in the parents (the same shuffling for each parent), and then the switch is made based on the new positions. Since the shuffle performs on the variables differently each time, any positional bias is removed. The result obtained with this method is similar to the uniform crossover technique.

The reduced surrogate crossover minimizes the unwanted crossover operations in case of the parents having same genes. First, it checks each individual genes in the parents and it creates the list of all possible crossover points, that corresponds to the position where the genes of the both parents are different. Two scenario may occur. If no crossover point is found no action is taken. Otherwise, if parents differ in more than one gene the method randomly selects one crossover point from the list and performs one-point crossover to create the offspring.

The cycle crossover is a permutation technique that looks for cyclic patterns between parental chromosomes. Starting from the gene of one parent a check in corresponding position is performed in the second parent. If the values are different this second value is searched in the first parent sequence and its position is registered. Then again, a new check in the corresponding position but in the second parent sequence is performed

and this new value is searched back in the first parent chromosome. This cycle stops when the same value is found in both parents. The offspring are then created by coping all the genes that are involved in the cyclic pattern from one parent maintaining their positions and by filling the free spaces with the genetic material from the other parent.

3.3.6 Mutation

Mutation is an operator that has the fundamental role in GA to maintain and introduce the genetic diversity within the new generations. The commonest mutation operators are displacement, simple inversion, and scramble mutation.

The displacement mutation cuts the genes between two randomly determined cut-points from the chromosome as a subset and then inserts them back, starting from a randomly selected location. The inversion mutation operator reverses the randomly selected string and places it at a random location. The scramble mutation operator places the elements in a specified range of the individual solution in a random order and checks whether the fitness value of the recently generated solution is improved or not.

To summarize, the biological-inspired operators implemented in GA are selection, crossover, and mutation. In selection, the chromosomes are selected on the basis of their fitness value for further processing. The crossover operators swap substrings of parents' chromosomes to create offspring. In mutation some genes of the chromosomes are randomly flipped on the basis of probability to maintain diversity within the new generation and prevent premature converge.

3.3.7 Detailed aspects of GA computing

Concerning the GA, the method and the operators utilized are described as follows. The PyGAD software has been employed [88–90]. It is an open-source Python 3 library for building the GA and optimizing machine learning algorithms; In addition, in its newest versions, its supports optimizing both single-objective and multi-objective problems. To run the GA code one needs to program in Python 3 the fitness function, which requires multiple test-parameter runs of TALYS (in Fortran) since the fitness function is built upon the χ^2 which compares calculated and experimental multiple

cross-sections. It is a characteristic of GA optimizations that the user has to attempt several GA options to adapt the GA to the particular computational problem one has to face. In this sense, it is not a standard black-box optimization routine where one limits the task to wait for the outputs, but several trials have to be performed before obtaining a reliable optimization result. Several PyGAD options have been attempted to improve the optimization performance of GA. For example, for the selection of parents a few tests have been performed with: *roulette wheel, rank, tournament, stochastic universal sampling, and steady-state selection*. Moreover, various levels of *elitism* have been considered in PyGAD: this is a strategy in GA that preserves the best individuals in a population from one generation to the next. It ensures that the optimal solution found so far is not lost due to crossover or mutation operations. Elitism can speed up the convergence of the GA and improve its performance. In PyGAD, the user can define the level of elitism by specifying the number of elite individuals to be copied to the next generation when creating an instance of the pygad.GA class. Various mutation operators have been tested as well, with the findings that the best performance were obtained with *adaptive mutation*. The mutation probability is usually fixed and does not depend on the quality of the solutions. This can lead to either premature convergence or slow convergence. Adaptive mutation aims to overcome this limitation by varying the mutation probability according to the fitness values of the solutions. The idea is to protect the high-fitness solutions from being disrupted by mutation, while increasing the mutation rate for the low-fitness solutions to escape from local optima. And finally, *uniform crossover* has been employed after testing various options available in PyGAD. In fig.3.6, a convergence test is given comparing the selection of parents using tournament and steady-state selection with two different levels of elitism. Tournament reaches a more rapid increase of the fitness value. As one can see from the figure, with a mild elitism, the fitness function can decrease from one generation to the subsequent. In a typical calculation, a sample population consisted of 40 individuals, and 16 parents were selected for mating for the offspring generation. Iterations were performed from a minimum of 50 generations up to a maximum of 200. Efficiency of GA improves dramatically with parallel computing, and the relevant parallel computations have been performed at the CLOUDVENETO platform (cloudveneto.ict.unipd.it), founded jointly by University of Padua and INFN.

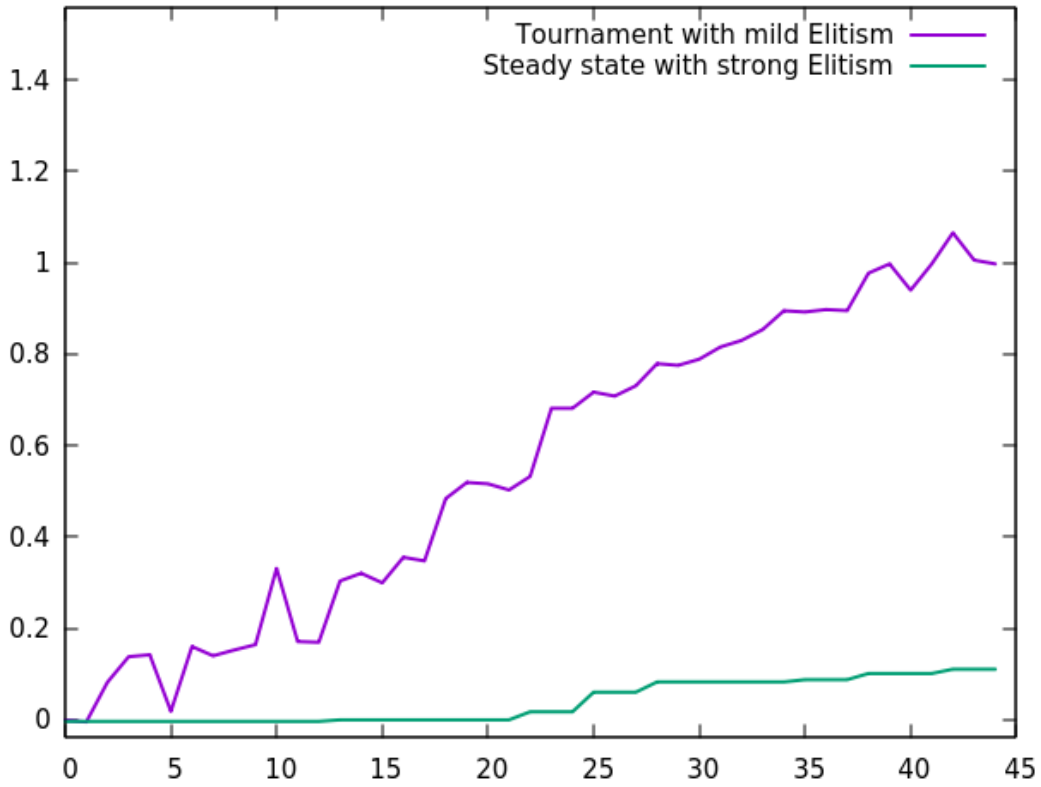

Figure 3.6 Convergence trials with respect to two different selection of GA operators, for optimization of the ^{49}Ti(p,x) cross sections. Horizontal axis: the population generations; vertical axis: normalized fitness function

Isotope	c	p
^{46}Sc	0.164	-0.124
^{47}Sc	-0.138	1.004
^{48}Sc	-0.285	-1.254
^{48}V	0.215	-0.547
^{44}Sc	-0.714	0.763
^{43}Sc	1.469	1.257

Table 3.3 List of the values obtained for the parameters c and p with the genetic algorithm optimization.

In table 3.3 the new *c* and *p* values obtained with the GA are listed. The relative effect of the modification of the nuclear level densities on the ^{47}Sc, ^{46}Sc, and ^{48}Sc cross sections is shown in Fig. 3.7 - 3.9.

For completeness the theoretical analysis has been extended also to the calculations of the radionuclides ^{44g}Sc, ^{44m}Sc, ^{43}Sc, ^{48}V, ^{42}K and ^{43}K, since these radionuclides cross sections have been measured within the REMIX project. Indeed, figs. 3.7 - 3.11 show the comparison between theoretical and measured cross sections. Regarding the

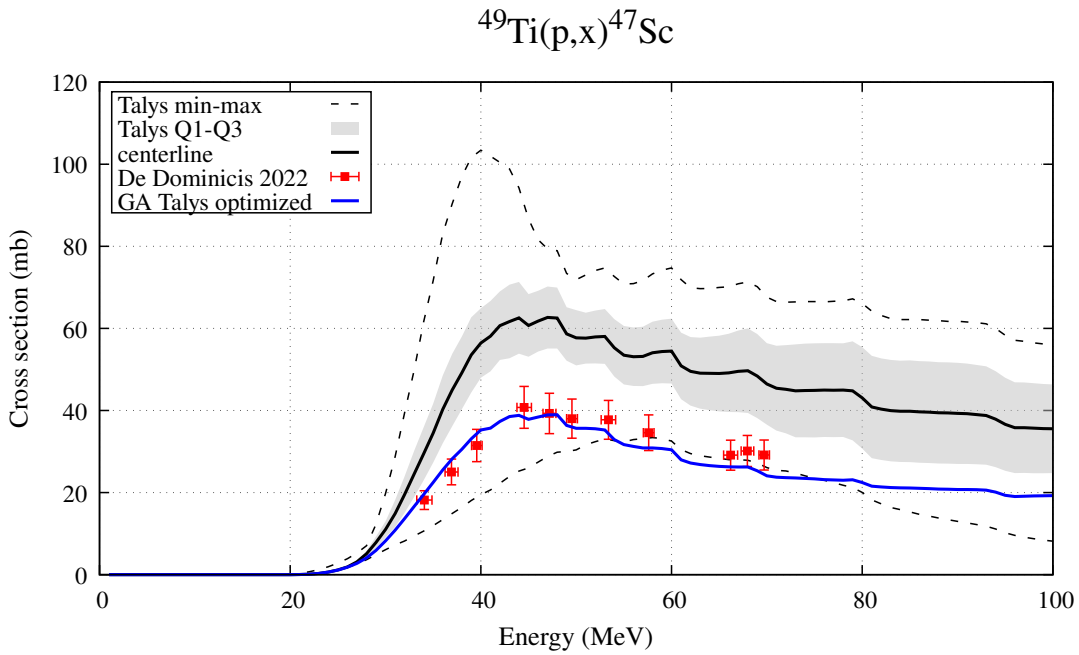

Figure 3.7 ^{47}Sc GA optimized cross sections for the reaction ^{49}Ti(p,x) compared to the statistical analysis.

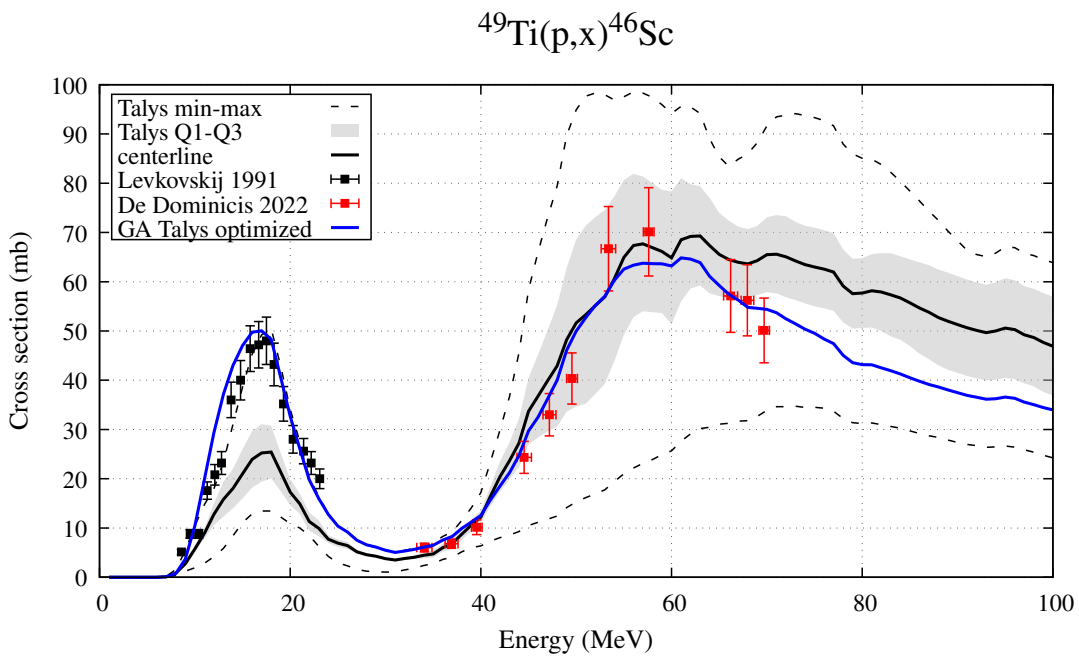

Figure 3.8 ^{46}Sc GA optimized cross sections for the reaction ^{49}Ti(p,x) compared to the statistical analysis.

TALYS calculations, all figures present the min-max of the models as dashed lines, the interquartile gray band, and the centerline as a solid black line. The new GA optimized curves are depicted as solid blue lines. The preliminary REMIX data cover an energy

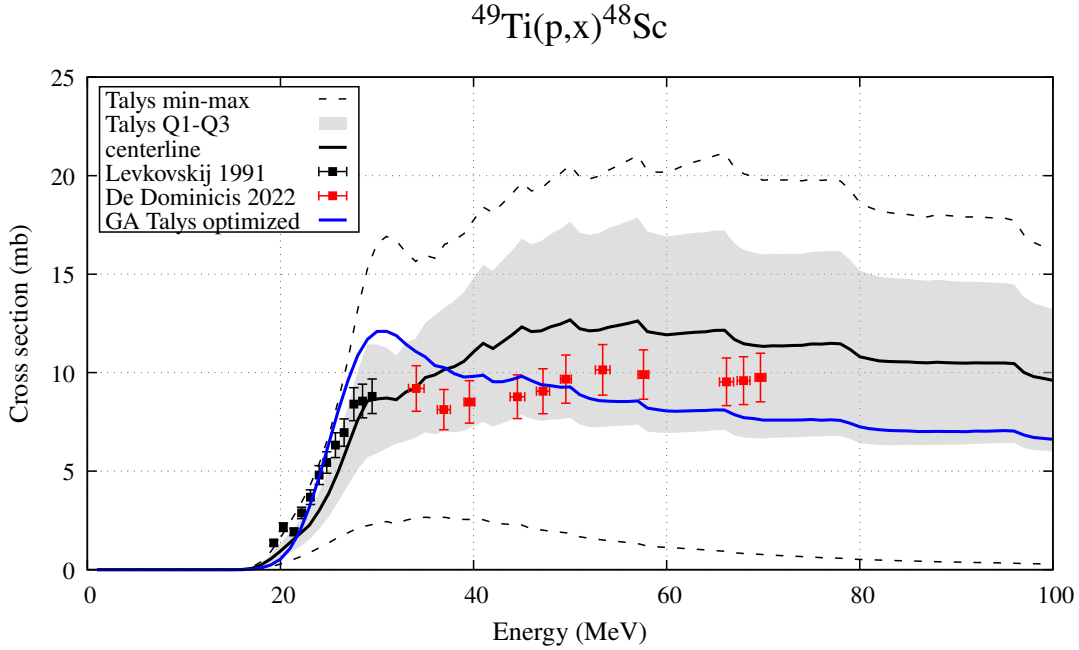

Figure 3.9 ^{48}Sc GA optimized cross sections for the reaction ^{49}Ti(p,x) compared to the statistical analysis.

range between 30 and 75 MeV. Here they are illustrated and compared with data from the literature when available. Generally, the GA fit turn out remarkably close to the data. The agreement between data and theory is overall satisfactory, and even for the radionuclides in which the reproduction is not perfect the use of GA leads anyway to an improvement of the cross sections. Below a more precise description is given for each radionuclide.

The relevance of ^{47}Sc cross section calculations is related to the absence of previous measurements before the preliminary REMIX data. The theoretical analysis has been essential to guide the experiments, allowing to identify the optimal irradiation parameters and conditions that correspond to a maximization of the production yield and a minimization of the co-produced contaminants. Afterwards, the comparison between the newest data and the theoretical cross sections allows to validate the models description and to adjust the models free parameters. The ^{47}Sc case express very clearly the strength of the GA optimization. The blue line reproduces almost perfectly the ^{47}Sc cross section data. It sholud be noted that the GA optimization lowers the cross section if compared to the centerline calculations, with a consequent effect on production yield and activity for the channel ^{49}Ti(p,x)^{47}Sc. The cross

section of the main contaminant ^{46}Sc, Fig. 3.8, displays an evident improvement in the reproduction of low energy data. The peak is well reproduced, the minimum is confirmed at around 30 MeV, and also the region at higher energy shows an better fit of the data. This has important consequences for the evaluation of the ^{47}Sc production for applications in nuclear medicine. The comparison of the GA TALYS optimized curves of ^{47}Sc and ^{46}Sc identifies 32-40 MeV as the optimal energy window for a good production of ^{47}Sc with a low level of contamination from ^{46}Sc, since at around 30 MeV corresponds an increase of the ^{47}Sc cross section and the minimun of ^{46}Sc. Besides, this selection excludes the low-energy ^{46}Sc peak that cloud burden the level of contamination.

The contaminant ^{48}Sc represents another harmful radionuclide due to the energies of its γ-rays, even though its half-life of 43.76 h is relative short when compared to the ^{47}Sc and ^{46}Sc ones. It is extremely important to reduce its presence in the production and a strategy is to limit the energy range to avoid the interval in which ^{48}Sc cross section rises. Between 20 and 30 MeV the ^{48}Sc rises and at higher energies, even if it slightly decreases, it is not negligible. This means that by selecting 32 MeV as the ideal starting value it is not possible to exclude the ^{48}Sc from the production. Therefore its presence in terms of activity has to be included in the evaluation of the reduction of the purity of the production route.

For ^{44g}Sc (Fig. 3.10, panel A) the reproduction of data is slightly imperfect. The set of c and p values found with GA improves the cross section, despite this the data at 40 MeV is not reached from the optimized curve and so the peak is underestimated. Also for the ^{44m}Sc (Fig.3.10, panel B) case the agreement around the peak is not excellent and the curve underestimates the data, while at higher energy the curve overestimates the measurements. Both ^{43}Sc and ^{48}V (Fig. 3.10, panel C and D, respectively) exhibit a general agreement between measured and theoretical cross sections. For the cross sections of ^{42}K and ^{43}K (Fig 3.11)the agreement between theory and the few available data is satisfactory.

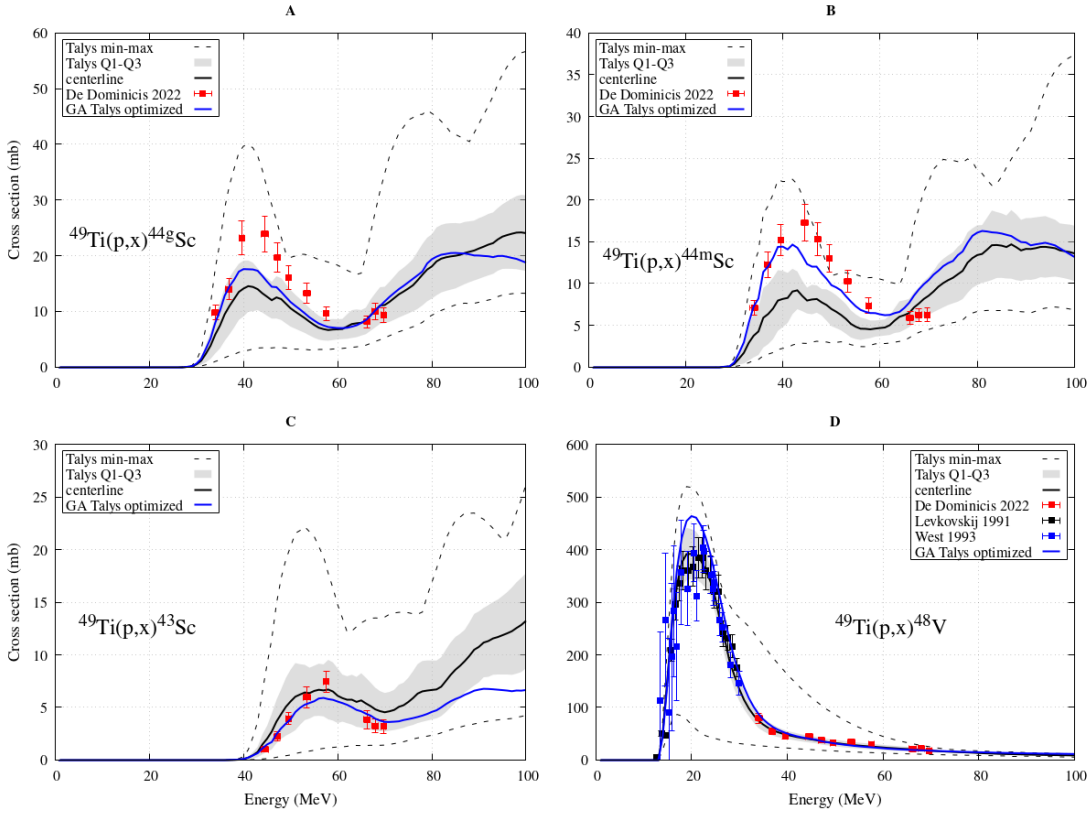

Figure 3.10 ^{44g,44m,43}Sc and ^{48}V GA optimized cross sections for the reaction ^{49}Ti(p,x) compared to the statistical analysis.

3.3.8 The two-steps optimization method

The analysis of the production route ^{49}Ti(p,x)^{47}Sc consists of two main steps. First a theoretical evaluation of the cross sections of the main radionuclides produced during an irradiation experiment, taking into account the variability of the models used to describe the nuclear reaction mechanisms. Secondly, an optimization procedure to achieve a better reproduction of the data in order to be more accurate in the subsequent prediction of the quantities that depends on the calculation of the cross sections. At this stage it is possible to distinguish between a first and a second level of optimization. The former is a visual inspection of the curve after a variation in the free parameters that governs the nuclear level density. The latter is the application of the GA to further improve the reproduction of the cross sections, acting on the same c and p parameters that has been modified roughly in the previous step. This finer tuning has the advantage of a better assessment of the cross sections and from there of the production yields,

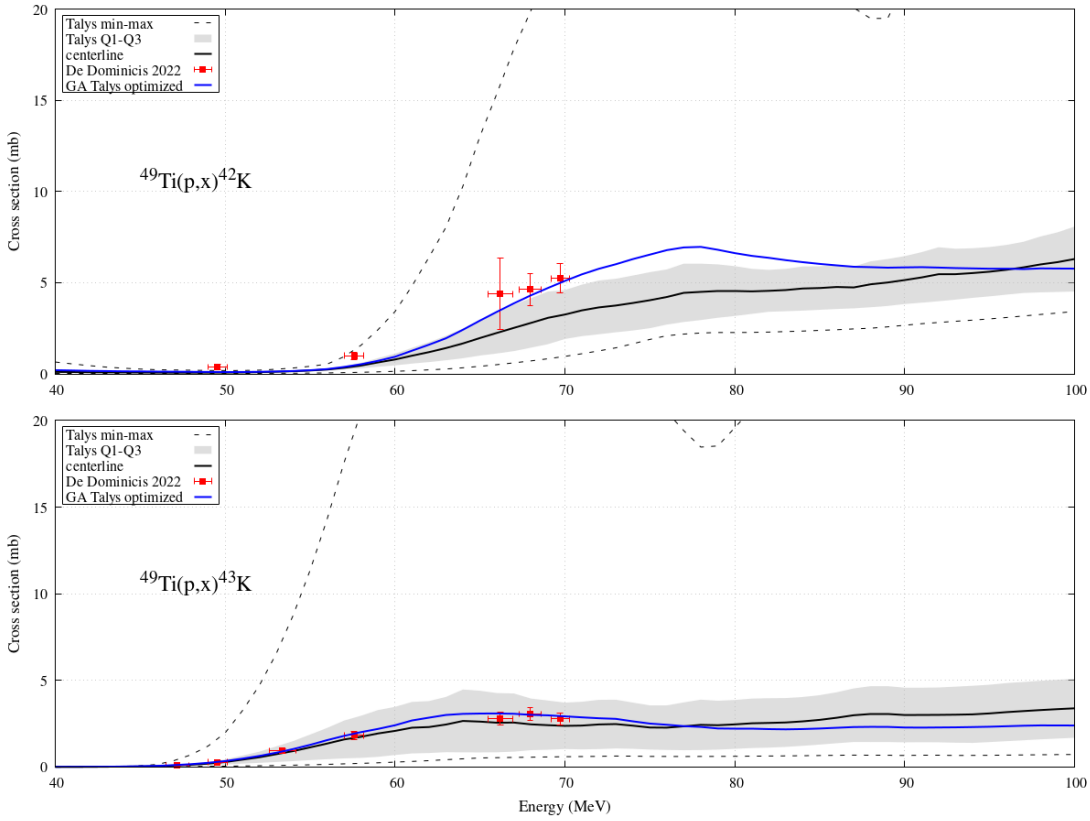

Figure 3.11 ^{42}K and ^{43}K GA optimized cross sections for the reaction ^{49}Ti(p,x) compared to the statistical analysis.

activities and purity. The first step results in a convenient skimming of the c and p values, such that they become one of the first chromosomes that compose the initial population of the algorithm, providing a hint to the optimal solution.

It is interesting to observe the effect and the actual improvements achieved when GA are applied. In figs. 3.12 - 3.14 the comparison of the first (red line) and the second (blue line) step of the optimization method is presented. Basically the red curves represent the staring point of the optimization procedure and the blue curves are the final GA solution.

Fig. 3.12 shows the ^{47}Sc, ^{46}Sc, and ^{48}Sc cross sections. For ^{47}Sc the GA optimization reproduces the cross section better than the red curve at low energies and around the peak region, but not that precisely at higher energies.

Regarding the ^{46}Sc, the improvement is remarkable when the GA is adopted. The peak is well reproduced, the minimum is confirmed, and the agreement at higher energies is

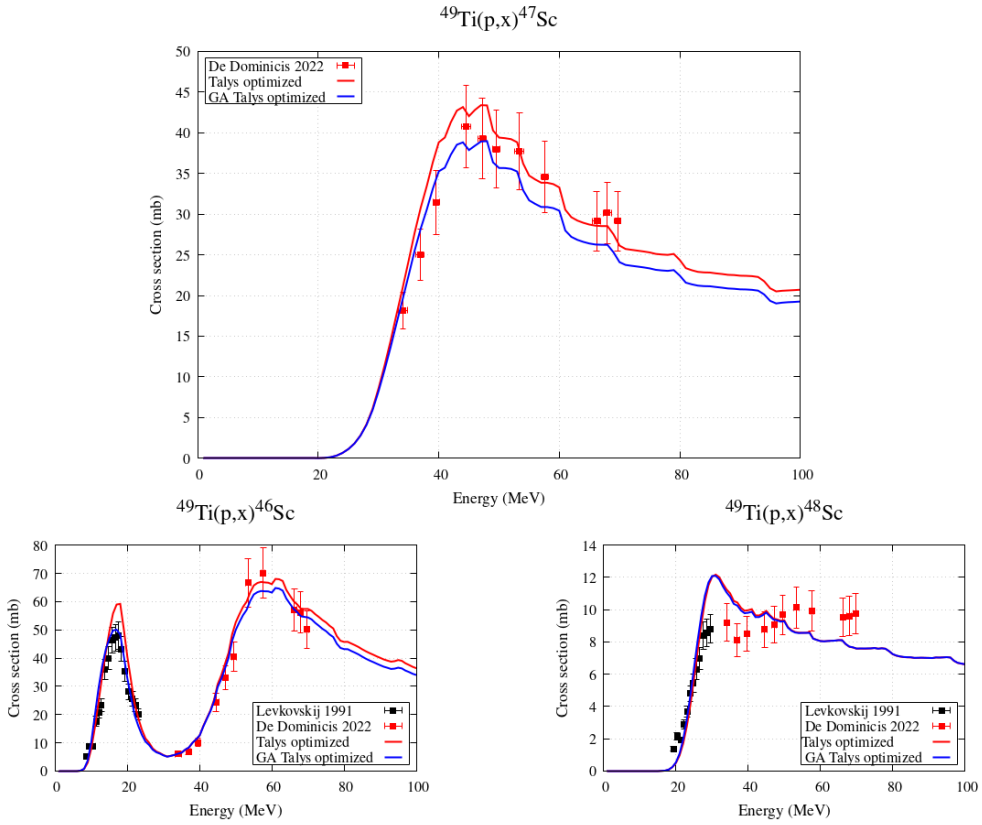

Figure 3.12 The two-steps optimization method for ^{47}Sc, ^{46}Sc and ^{48}Sc. The red curves represent the starting point and the blue lines the final result of the optimization.

satisfactory.

For the ^{48}Sc no differences can be seen between the two optimization steps. In this case the GA does not upgrade the theoretical cross section.

In Fig. 3.13 panel A,B, and C the cross sections of ^{44g}Sc, ^{44m}Sc, and ^{43}Sc are shown. As a general consideration, both optimization steps do not succeed in the improvement of the cross sections. As a matter of fact, the GA seems to worsen the reproduction, especially for the ^{44g}Sc and ^{44m}Sc. For the ^{48}V, panel D, the use of GA involves a better reproduction of the cross section.

Finally, the finer tuning of the c and p parameters obtained with the GA entails a better reproduction of the cross sections for the ^{42}K and ^{43}K, as shown in Fig. 3.14.

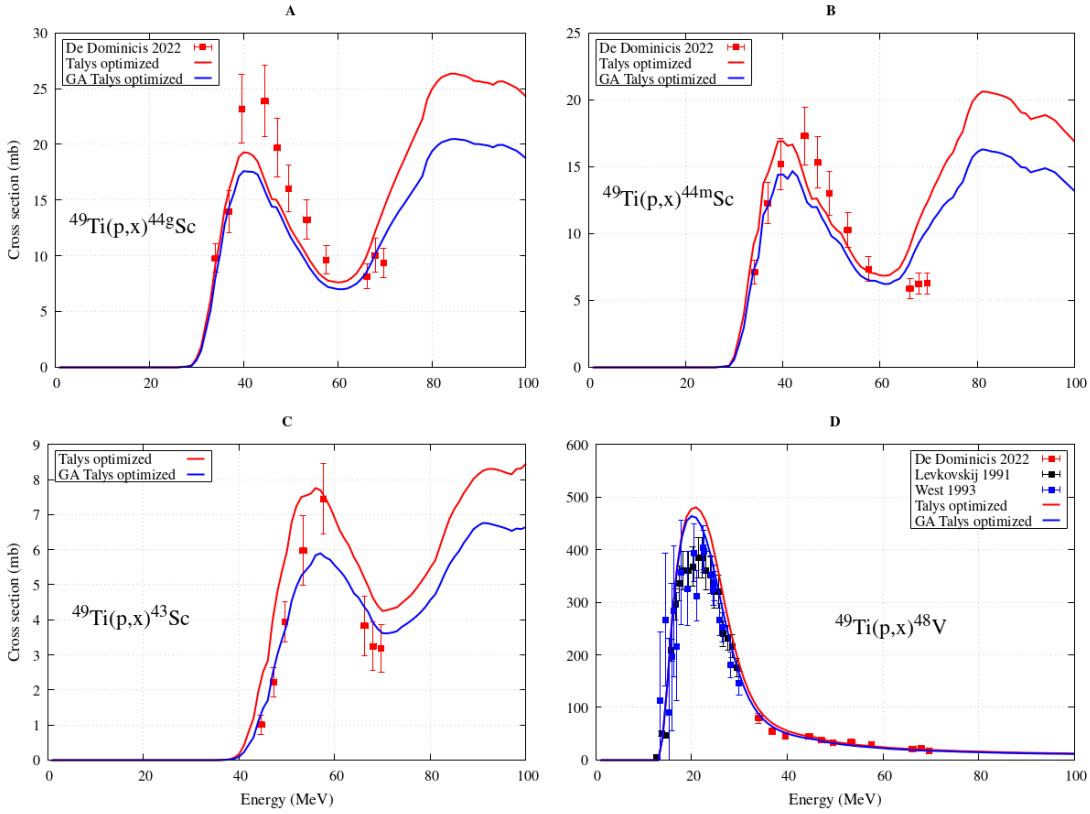

Figure 3.13 The two-steps optimization method for ^{44g,44m,43}Sc and ^{48}V. See Fig. 3.12 for details.

3.3.9 Yields, Activities and Purity

Once the optimized TALYS calculations have been performed the evaluation of the production yields, activities and purity has been investigated. The definitions of all these quantities are summarized in Sect. 2.5 and the numerical method utilized is described in [5]. Fig. 3.15 shows the comparison among ^{46}Sc, ^{47}Sc, and ^{48}Sc yields obtained with the statistical analysis, considering the 30 possible combination of the TALYS models. The gray shades indicate the optimal energy range that maximises the ^{47}Sc yield and reduces at best the contamination. The ^{46}Sc production, illustrated in orange, is almost negligible in the entire selected window, while the ^{48}Sc yield, the red curve, overlaps the blue-colored ^{47}Sc one, even if it is lower.

The assessment of the RNP of the route is necessary to verify if the purity is sufficiently high to satisfy the clinical requirements. According to the European Pharmacopoeia a 99% of RNP is suggested. Lower values could be acceptable providing that the higher

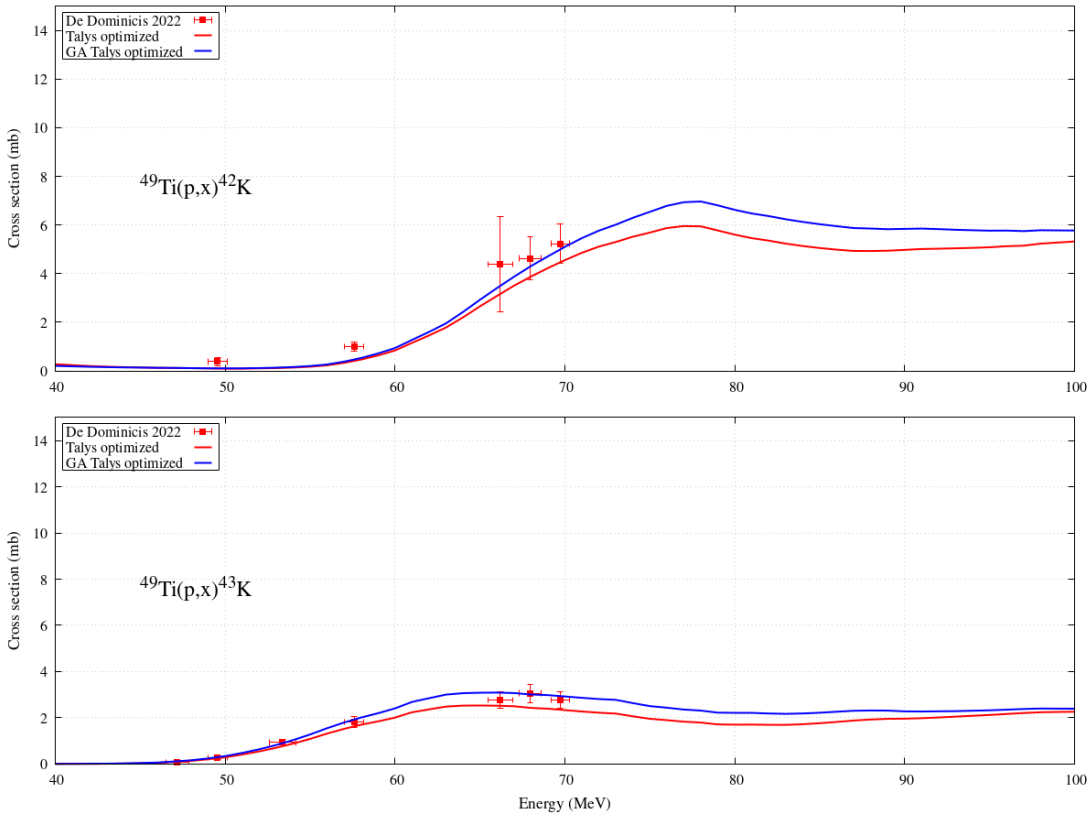

Figure 3.14 The two-steps optimization method for ^{42}K and ^{43}K. See Fig. 3.12 for details.

level of contamination does not entail an increase of the dose beyond the limit of 10%. Fig. 3.16 shows the comparison of the RNP according to the band description (in black) and the optimized calculations (blue line), calculated for E = 32 – 40 MeV, T_{irr} = 1 h, and I = 1 μA. In the former case the maximum RNP value is around 0.75 after 10 days and it rapidly decreases. RNP lowers to a max of 0.6 in the latter condition. Both approaches confirm the inadequacy of the production route in clinics, since such low values involve a level of contamination too high for safe applications.

Therefore, it can be concluded from the present analysis that the reaction ^{49}Ti(p,x)^{47}Sc is not adequate as production route due to fact that the high standards implied by the applications in nuclear medicine cannot be met.

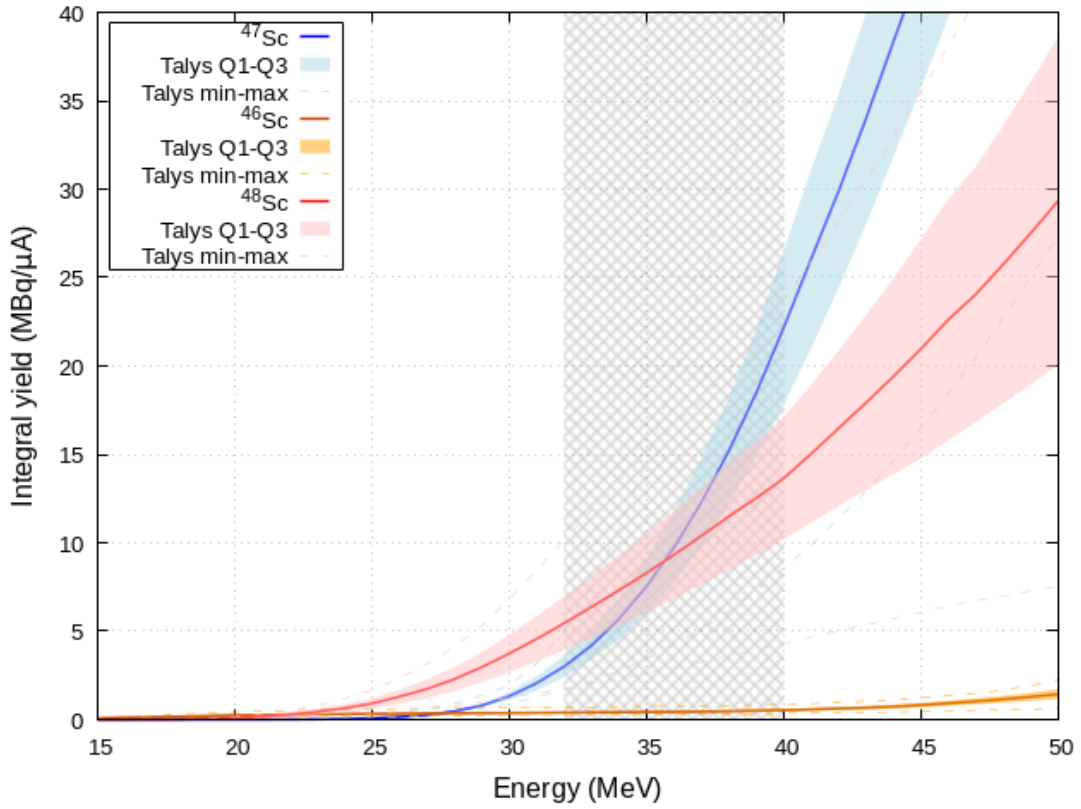

Figure 3.15 Comparison of the production yield for the radionuclide ^{47}Sc and is main contaminants ^{46}Sc and ^{47}Sc.

3.4 The nuclear reaction ^{49}Ti(d,α)^{47}Sc

Since the ^{47}Sc production is of interest for medical applications, an alternative nuclear reaction that still entails enriched ^{49}Ti targets has been investigated. A preliminary analysis identifies the use of deuteron beams impinging ^{49}Ti as an interesting channel to be examined. Nevertheless, for this reaction a sole and old experimental dataset is available in Literature and this demands for new measurements to better understand the potential and efficacy of the production channel, giving also the possibility to deeper investigate the theoretical models used to describe that nuclear reaction. To commence it is necessary to ensure the actual feasibility of the route and to do so a theoretical study has been performed to verify the production yields of ^{47}Sc and contaminants, and the level of purity that can be achieved to confirm if its adequacy for applications in nuclear medicine is real.

Fig. 3.17 (left panel) illustrates the statistical cross section of the radionuclide ^{47}Sc

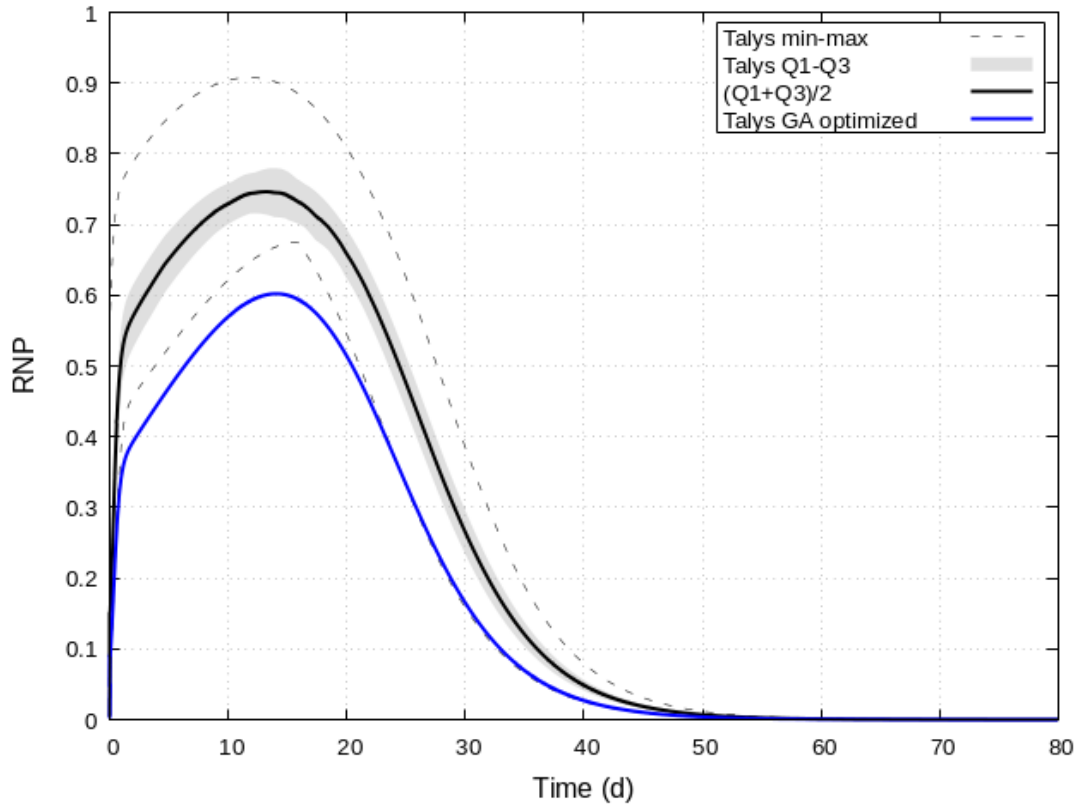

Figure 3.16 Comparison between the radionuclidic purity obtained with the statistical approach that takes into account the variability of the TALYS models and the one calculated from the optimized GA cross sections

(in blue) and its main contaminants, ^{46}Sc (orange) and ^{48}Sc (red). At fist glance the variability described by the TALYS models is wide, especially for the ^{46}Sc cross section for which the min-max distance spanned almost 100 mb. For these reactions the only available data are from Chen et al. [7]. It is evident a poor agreement between measured and theoretical cross section for the ^{46}Sc case. Although, focusing on the contaminant ^{46}Sc, the threshold of the reaction starts at around 10 MeV and it is well described by a thin band. Moreover the first data point, the closest to the threshold, is the only one within the band and that confirms the idea that around that energy the models are able to describe the reaction. This is a key point, because if one trusts the ^{46}Sc result at the threshold it could be possible to limit the production of this contaminant by selecting energies below 10 MeV. By restricting the energy range up to a maximum of 10 MeV one will be in the condition where the peak of ^{47}Sc occurs, that means a maximum production of ^{47}Sc characterized by a very low contamination by ^{46}Sc. This result suggests that considering low-energy deuterons on ^{49}Ti targets is promising, since a

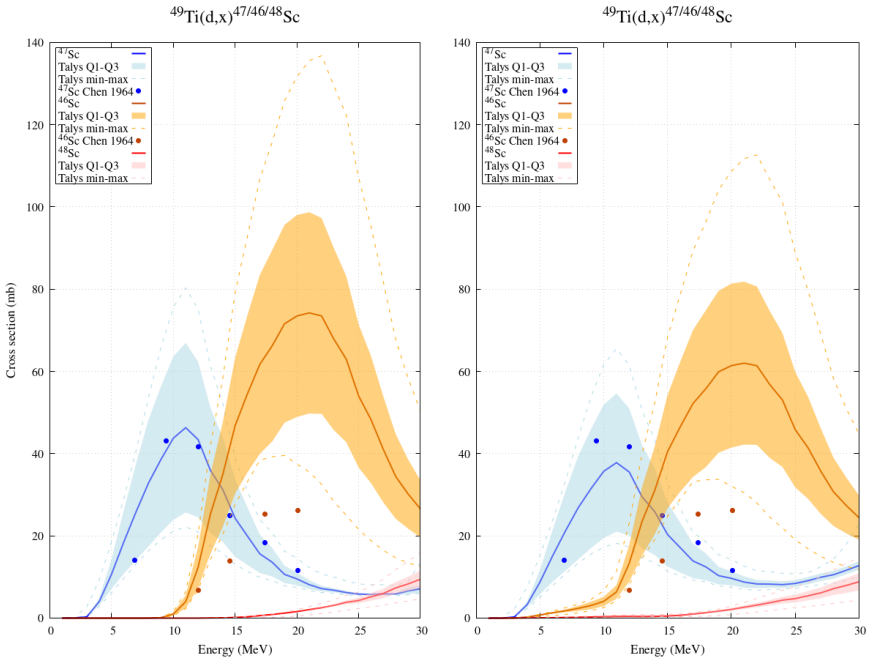

Figure 3.17 Comparison of ^{47}Sc (blue), ^{46}Sc (orange), and ^{48}Sc (red) cross sections by using the statistical representation of the TALYS models. The left panel refers to a 100% enriched ^{49}Ti target, in the right one the isotopic composition of the 82% enriched ^{49}Ti target used by Chen [7] has been considered.

small amount of contaminants is produced and the final purity is not compromised. Moreover, the possibility of the use of hospital cyclotrons makes the route even more interesting.

Fig. 3.17 (right panel) shows again the statistical cross section of ^{47}Sc (in blue), ^{46}Sc (orange), and ^{48}Sc (red), but this time when the isotopic composition of the ^{49}Ti target used by Chen is reproduced. Namely, the target is made of 81.5% of ^{49}Ti, 14.5% of ^{48}Ti, 1.4% of ^{50}Ti and 1.3% of both ^{46}Ti and ^{47}Ti [7]. When compared to the previous case of an ideal target, it is evident that here the production of the contaminant ^{46}Sc starts at lower energies, around 5 MeV. This is due to the quite large fraction of ^{48}Ti isotope contained in the target used by Chen, which produces ^{46}Sc below 10 MeV.

Therefore, it is important to observe that the Chen and Miller data have some limitations that need to be addressed by future research. As said before, their target was not fully enriched in ^{49}Ti and this means that the cross sections include contributions from other reactions involving ^{48}Ti, such as ^{48}Ti(d,α)^{46}Sc. This reaction does affect the accuracy and precision of the cross-section measurements. Therefore, it would be desirable to

repeat the experiment with a target that has a higher enrichment of ^{49}Ti, or to correct the data for the presence of ^{48}Ti. Another important limitation in this study concerns the fact that the nuclear reaction models do not properly account for the deuteron break-up contribution, which is an important process in deuteron-induced reactions. The deuteron break-up contribution refers to the possibility that the deuteron splits into a proton and a neutron before or after interacting with the target nucleus, resulting in additional contributions to final states. Most of the nuclear reaction codes used to calculate the cross sections for this reaction do not include this contribution. Therefore, further work is needed to improve the nuclear reaction models and include the deuteron break-up contribution in a more realistic way, as suggested recently by Avrigeanu [91]. To sum, the production route: ^{49}Ti(d,α) to produce ^{47}Sc is a feasible and attractive option for obtaining this radioisotope, but it requires more experimental and theoretical investigation to overcome some of the limitations of the existing data and models. A new experiment with a highly enriched ^{49}Ti target and a more accurate measurement of the cross sections would be valuable, as well as a better understanding and modeling of the deuteron break-up contribution in this reaction.

To improve the reproduction of the cross sections and reach a good agreement with the measurements to be able to more accurately predict the yields and activities, it is necessary to trust the few information collected from the preliminary analysis. An optimization strategy by means of GA has been carried out. The TALYS combination of models PE3–LD6 has been identified as the most convenient to define the new optimized curves, since without any change in the free level density parameters the cross sections were the one closest to the Chen data. By selecting c = 1.573 MeV$^{-1/2}$ and p = 0.390 MeV for the ^{46}Sc compound nucleus and c = -0.029 MeV$^{-1/2}$ and p = 1.327 MeV for the ^{47}Sc one a good result is obtained. The resulting cross sections are shown in Fig. 3.18

The new optimized cross sections allow to identify 5 - 10 MeV as the optimal energy range to reduce the contamination by ^{46}Sc, because the selected window is below the ^{46}Sc threshold and in correspondence of ^{47}Sc peak, which guarantees to exploit the maximum of the production of ^{47}Sc. Fig.3.19 and 3.20 show the calculated yields

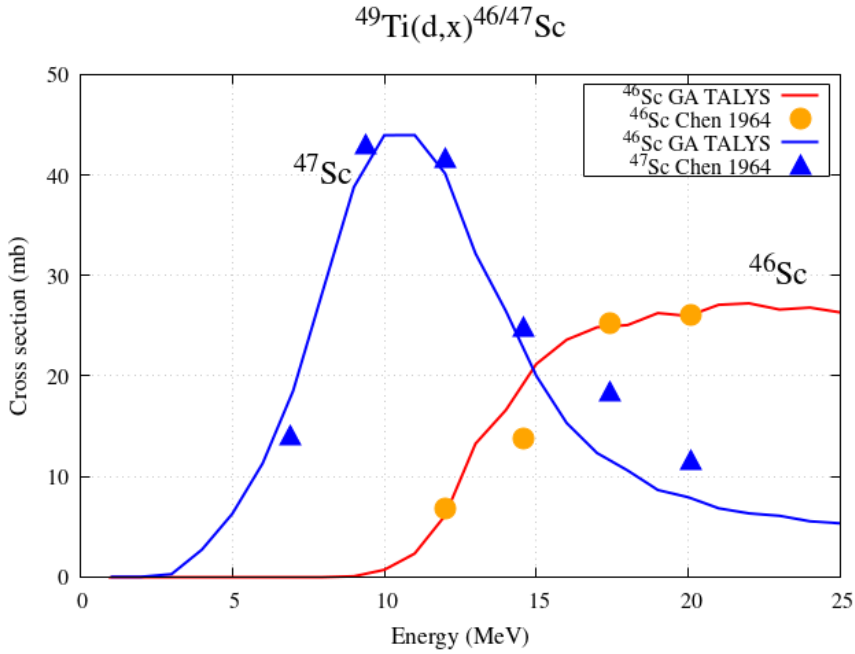

Figure 3.18 ^{47}Sc and ^{46}Sc GA optimized cross section for the reaction ^{49}Ti(d,x).

considering the standard irradiation conditions of T_{irr} = 1h and I = 1 μA, and in both figures the green box points out the ideal energies to optimize the production. The former illustrates the comparison of the ^{47}Sc yield calculated considering all TALYS models and the one obtained starting form the GA cross sections. The centerline of the interquartile band, the solid black line, represents the reference value in the statistical description of the yield, while the red line reproduces the optimized yield. The decrease of the ^{47}Sc cross section when the GA method is applied is responsible for a reduction of the production yield, as seen in Fig.3.19. The second figure compares the yields of ^{47}Sc with the ones of its main contaminants. It is evident that the contamination by ^{46}Sc and ^{48}Sc can be considered negligible in the ideal energy range and that confirms the idea of ^{49}Ti(d,x)^{47}Sc as a high-purity route suitable for clinics, suitable also for hospital cyclotrons. In Table 3.4 the integral yield values are reported for the three radionuclides. Specifically, the yield of 1.418 MBq/μA·h for ^{47}Sc could be enhanced by increasing the irradiation time or the current. The eventual change of the irradiation setups would lead to a rise of the amount of all products of the reaction, but this would not affect the quality of the production itself.

Finally, the evaluation of the RNP indicates a value higher than 99%. Fig. 3.21

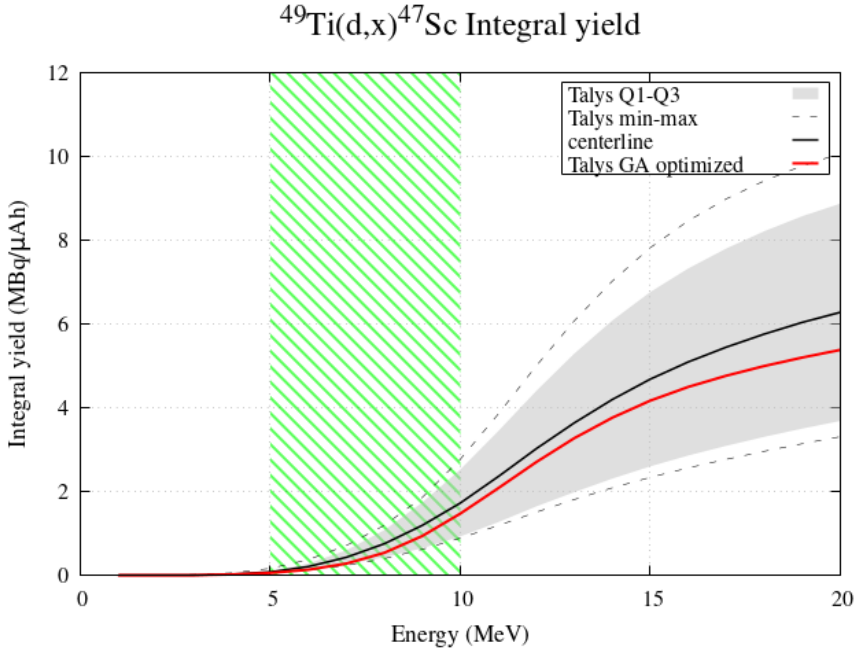

Figure 3.19 Integral yield

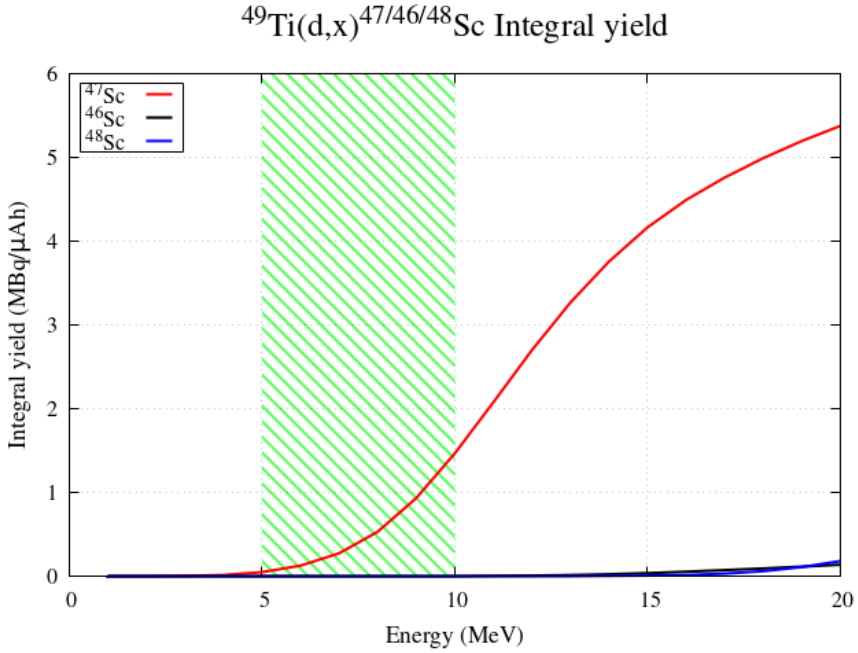

Figure 3.20 Comparison of the integral yield of ^{47}Sc, ^{46}Sc, and ^{48}Sc.

Yield (MBq/μA · h)		
^{47}Sc	^{46}Sc	^{48}Sc
1.418	2.14E-04	0.0

Table 3.4 Integral yield of ^{47}Sc and contaminants calculated for T_{irr} = 1h, I = 1 μA, E_{max} = 10 MeV and E_{min} = 5 MeV.

shows that it is possible to maintain that high purity for almost 20 days. This outcome is convenient for nuclear medicine applications, in particular when the shipment of the radiopharmaceutical to hospitals or research laboratories is needed. Moreover, to be effective for practical purposes it would be sufficient to check the RNP at a time corresponding to one or two ^{47}Sc half-life (~ 4-8 days). It is clear even more so that the 99% limit is satisfied within that reduced time window.

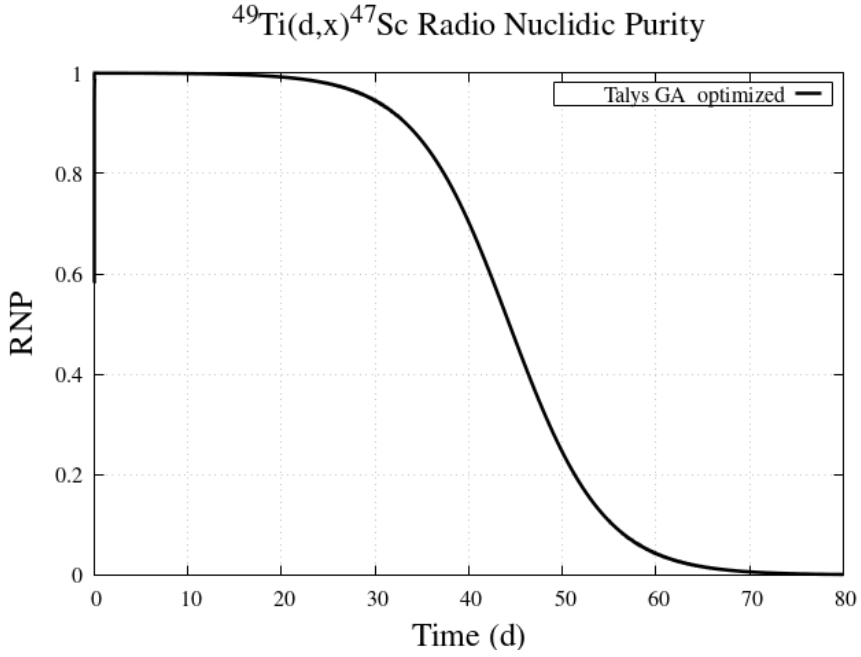

Figure 3.21 Radionuclidic purity for the reaction ^{49}Ti(d,x)^{47}Sc

In addition, the isotopic purity has been computed. According to fig. 3.22 the isotopic purity reaches and maintain a high value within 10 days. This suggests this production route to be basically carrier-free, due to a not significant presence of contaminants.

To conclude, the nuclear reaction ^{49}Ti(d,x) is a promising route thanks to the possibility to produce the radionuclide ^{47}Sc almost pure with a very minimum contamination by ^{46}Sc. Indeed, the theoretical results indicate a RNP above the 99%, which confirms the goodness of this channel for medical investigation. Since clinics is the main goal a good reproduction of the cross sections is fundamental to accurately predict all the derived quantities and then confirm the feasibility of the route. The results achieved so far attest to this. In order to improve the initial agreement of the measured and calculated cross sections, further analysis should be carried out. To this purpose the

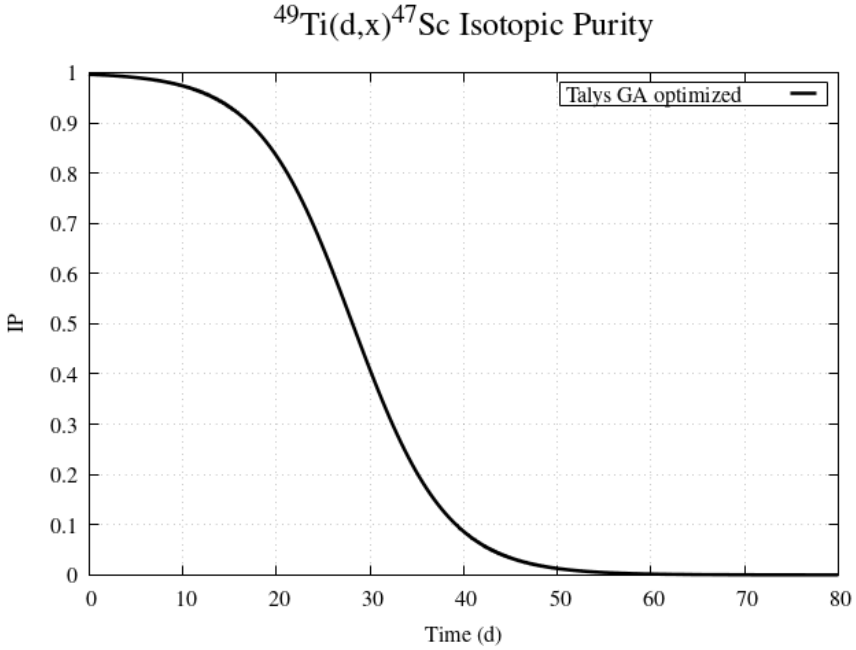

Figure 3.22 Isotopic purity for the reaction ^{49}Ti(d,x)^{47}Sc

need of new experimental data is clear and this would validate the models and would allow to refine their free parameters.

3.5 The nuclear reaction ^{50}Ti(p,α)^{47}Sc

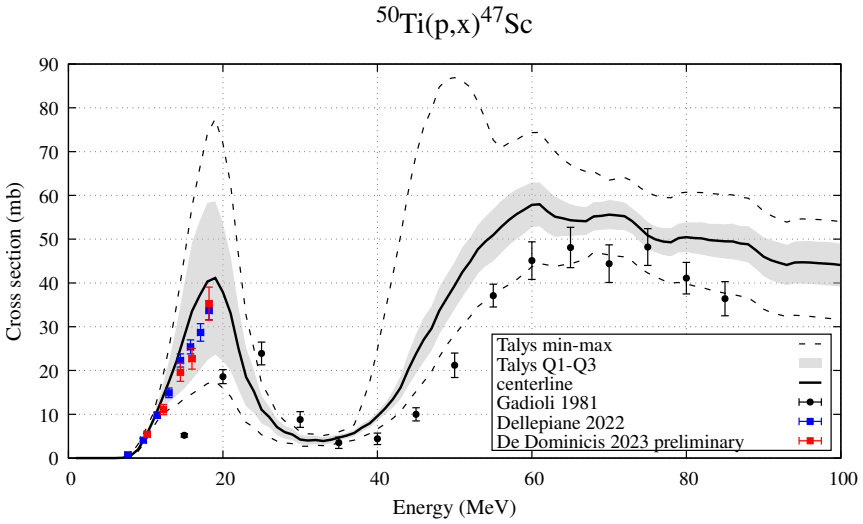

Figure 3.23 Statistical description of ^{47}Sc cross section. The dashed lines are the min-max values of the TALYS models, the gray area is the interquartile band, and the solid black line the centerline of the band that represents the most representative value of the cross section. Theoretical curves are compared to the measured cross section.

The third reaction analysed here for the ^{47}Sc production involved the use of enriched

^{50}Ti targets and proton beams as projectile. Fig. 3.23 describes the statistical cross section of ^{47}Sc and compares it to the experimental data available up to now. For the description of the theoretical curve refers to the figure caption. The black dataset is the old measurements by Gadioli 1981 [72]. The newest data belong to Dellepiane et al., the blue dots, and De Dominicis et al., the red ones. The last ones are preliminary data obtained within the REMIX project. They represents, together with the Dellepiane data, a decisive turning point in the analysis of this nuclear reaction. It is very clear that none of TALYS models is able to reproduce the peak identified by Gadioli at around 25 MeV. According to the centerline, that is the most representative value of the theoretical cross section, it should occur slightly before 20 MeV. An accurate analysis of all possible combination of TALYS models lead to the conclusion that none model is able to reproduce the Gadioli cross section. The availability of the newest datasets clarifies the scenario. Both measurements refer to the same low-energy range and they are in agreement among themselves. When these data are considered, it is evident the good reproduction of the cross section by the models. This result suggests a likely issue related to the Gadioli measurements at the threshold energy.

Since it is important to assess the quality of the production, the analysis has been extended to the evaluation of cross section of the main contaminant ^{46}Sc. Fig.3.24 shows both the theoretical cross section and the experimental data. For both Dellepiane and De Dominicis only one point is measured in correspondence of the threshold energy of the reaction.

Focusing on the newest experimental data and the centerline for ^{46}Sc cross section, their agreement is almost perfect. However, a first level optimization has been performed to refine the steep rise of the cross section between 10 and 20 MeV. The most adequate combination of models to describe it is PE3 - LD4. By changing the c and p parameters for the compound nucleus ^{47}Sc, namely c = 0.0 MeV$^{-1/2}$ and p = 0.5 MeV, an improvement on the reproduction of the cross section is obtained. Actually, c = 0.0 MeV$^{-1/2}$ implies that no normalization factor has been introduced with respect to the original microscopic Hartree-Fock level density, while a shift of 0.5 MeV has been applied towards higher energies, that could originate from shell-model or pairing

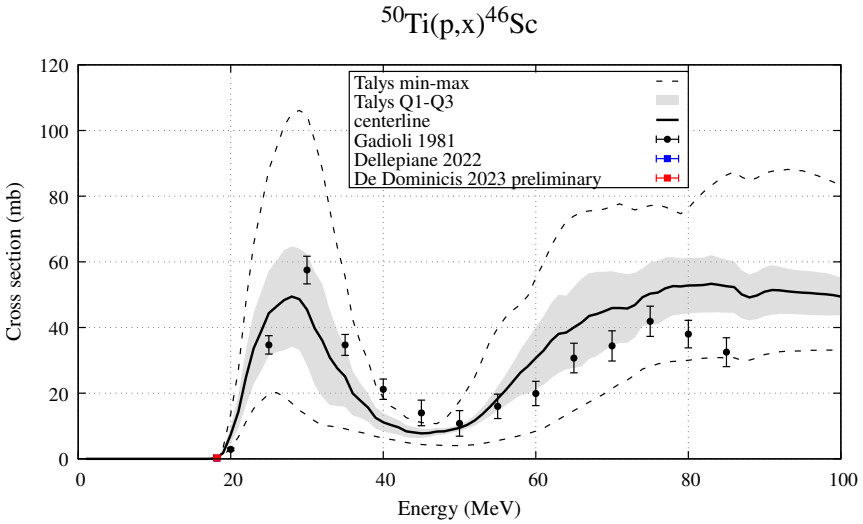

Figure 3.24 ^{46}Sc cross section for the reaction ^{50}Ti(p,x)

effects. The result is shown in Fig. 3.25

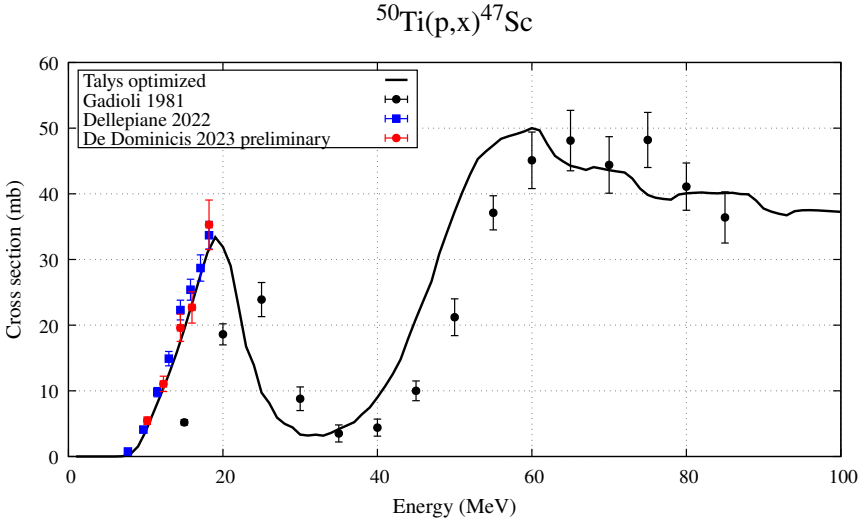

Figure 3.25 ^{47}Sc optimized cross section for the reaction ^{50}Ti(p,x).

The modification of the ^{47}Sc level density parameters has an effect also on the ^{46}Sc cross section, as illustrated in Fig. 3.26. Namely, the variation on ^{47}Sc implies an improvement also in the ^{46}Sc cross section.

It is worth to notice that in both cases the reproduction of the cross section at higher energies are not optimal. At those energies only data from Gadioli are available and they might not be that precise to build on them the optimization of the cross sections. In addition, the interest of the work focuses on the low energies up to 20 MeV, before

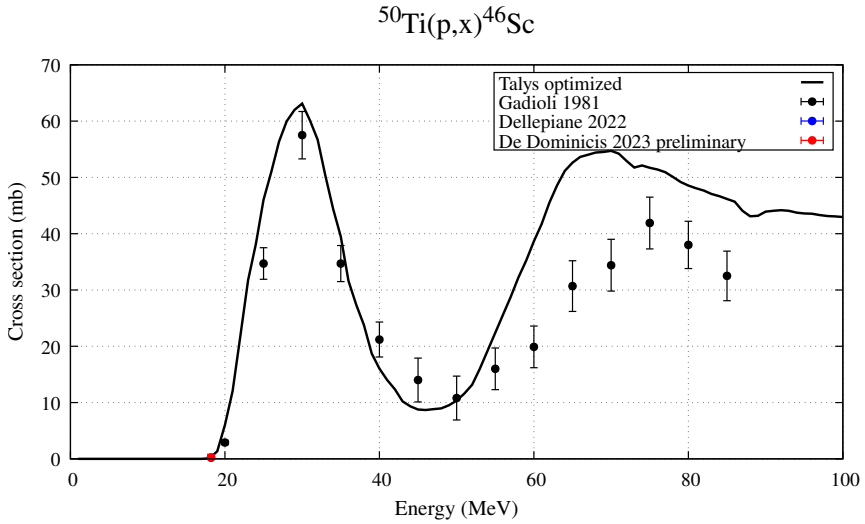

Figure 3.26 ^{46}Sc optimized cross section for the reaction ^{50}Ti(p,x).

the point at which the ^{46}Sc cross section rises and spoils the low level of contamination. For the aim of this study it has been sufficient a good cross section reproduction in that limited range, namely in 8-18 MeV.

From the optimized cross section the evaluation of the yields has been performed considering an irradiation of 1 h and a current of 1 μA. The comparison of ^{47}Sc yields derived from different approaches to the cross section, the statistical and the optimized one, is presented in Fig.3.27. The green area highlights the optimal energy range, 8-18 MeV, that guarantees a low contamination by ^{46}Sc and ^{48}Sc. All the black curve and the gray area refer to the descriptive statistics that carries the information of the variability of the models, while the red line is the optimized calculation. To improve the reproduction of the cross section data the value of the cross section itself has been slightly reduced and this decrease can be seen also in the yield.

To assess the quality of the production the analysis of the yield has been performed also of the main contaminants, ^{46}Sc and ^{48}Sc. In fig. 3.28 the red line refers to the ^{47}Sc yield, the black curve to the ^{46}Sc, and the blue one is the ^{48}Sc. Clearly, the contribution from the contaminants is negligible within the highlighted window. Tab. 3.5 displays in numbers what fig 3.28 already shows.

This comparison implies a clear result: the nuclear reaction ^{50}Ti(p,x)^{47}Sc is an

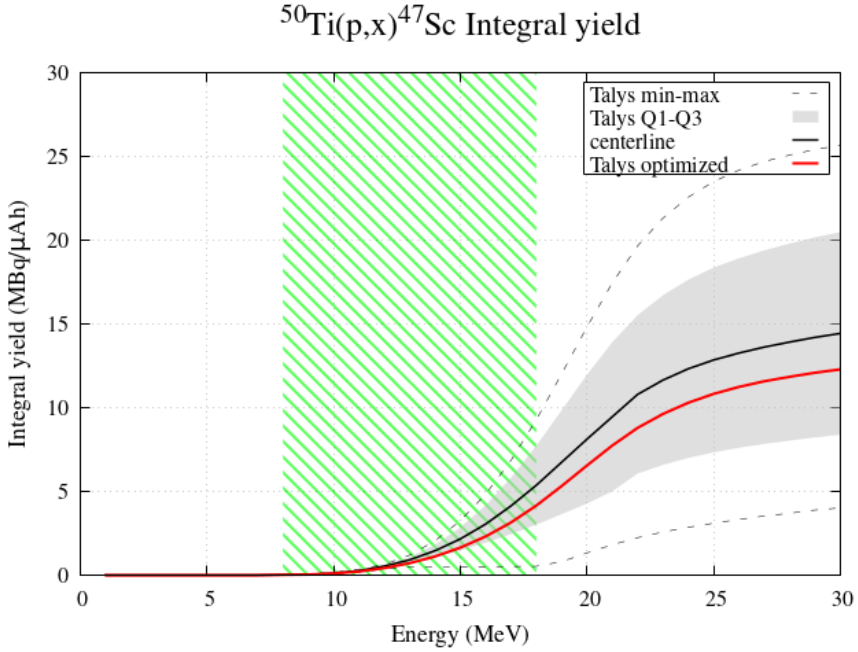

Figure 3.27 ^{47}Sc integral yield.

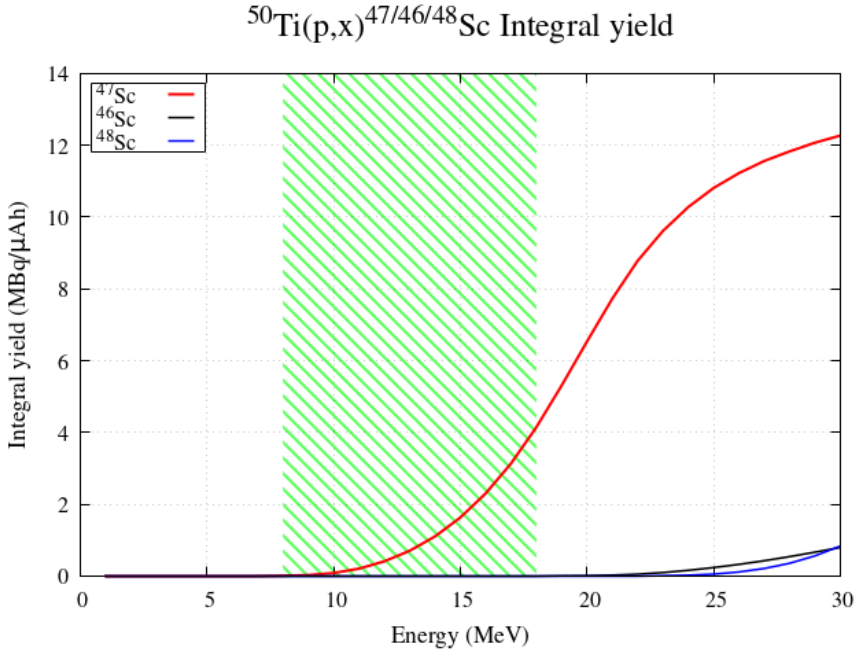

Figure 3.28 ^{47}Sc, ^{46}Sc, and ^{48}Sc integral yield.

Yield (MBq/μA · h)		
^{47}Sc	^{46}Sc	^{48}Sc
4.138	8.35E-05	0.0

Table 3.5 Integral yield of ^{47}Sc and contaminants calculated for the reaction ^{50}Ti(p,x), considering T_{irr} = 1h, I = 1 μA, E_{max} = 18 MeV and E_{min} = 8 MeV.

interesting channel to be considered for the production of high specific activity ^{47}Sc. In terms of activity produced this route appears more advantageous than the reaction with d-beams on enriched ^{49}Ti. Referring to Tables 3.4 and 3.5, a ^{47}Sc yield of 4.138 MBq/μA $\cdot$ h for the case p-^{50}Ti is almost 3 times higher than the corresponding yield for the d-^{49}Ti reaction. Moreover, while the contamination by ^{48}Sc is zero in both cases, the ^{46}Sc contribution to the production is smaller when protons on ^{50}Ti targets are considered. This means that the ^{50}Ti(p,x)^{47}Sc reaction is more favourable both in terms of the amount of activity and quality of the production. Additionally, the widespread use and availability of proton beams promote the p-^{50}Ti route even further. The assessment of the RNP confirms this outcome.

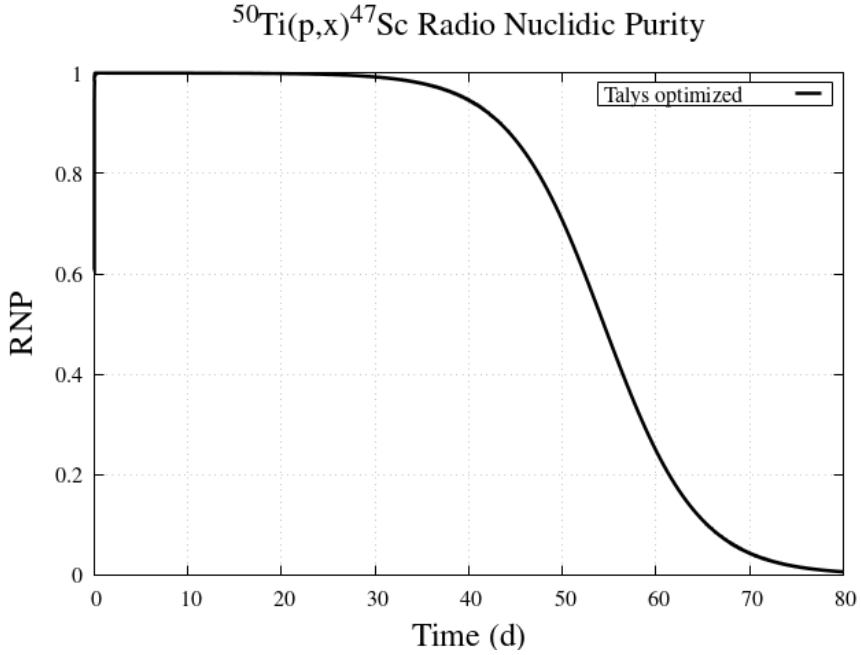

Figure 3.29 Radionuclidic purity of the reaction ^{50}Ti(p,x)^{47}Sc.

Based on all the above considerations, the RNP is expected to be higher than 99%. Indeed, the RNP is almost 1 for at least 30 days, as shown in fig.3.29. The time window in which this high level of purity is maintained is longer than the one previously discussed for the reaction d-^{49}Ti. As already said for the d-^{49}Ti case, to be effective for medical applications it is sufficient to consider the RNP for a maximum of one or two ^{47}Sc half-life. Similarly, the isotopic purity, fig.3.30, results higher for this channel.

These results lead to the conclusion that the nuclear reaction ^{50}Ti(p,x)^{47}Sc is the most

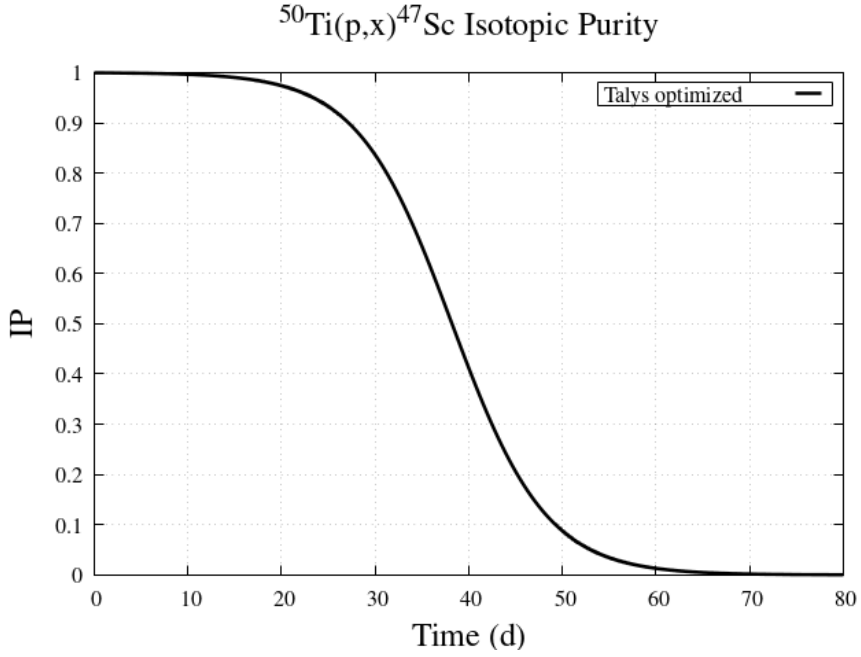

Figure 3.30 Isotopic purity of the reaction ^{50}Ti(p,x)^{47}Sc.

favourable among the three proposal put forward. This means that the two main aspects to be willing to consider any medical application are here satisfied. The clinics demands for a sufficient and high-quality production. Considering the production of ^{47}Sc, the use of proton beams on enriched ^{50}Ti targets represents a interesting option. The high level of purity due to a small co-production of contaminants has been widely discussed above. Concerning the amount of the activity produced, its adequacy depends on the specific medical practise. In case of need, a way to enhance the production to satisfy the medical purpose is to increase the irradiation time and/or the current. Hence, in this instance all conditions for a successful and efficient production are met.

3.6 The bilayer

An interesting method to produce high-quality ^{47}Sc by means of cyclotrons of intermediate energy is the use of bilayer targets. The idea comes from the possibility of utilizing a target made of different subsequent layers of different materials to exploit a wider range of energies of the projectile. The two reactions considered in the study are ^{nat}V(p,x)^{47}Sc and ^{50}Ti(p,x)^{47}Sc. The goal is the maximization of the ^{47}Sc production, while minimizing the co-production of the contaminants ^{46}Sc and ^{48}Sc, by using proton beams of E_{max} = 35 MeV. This study has lead to an industrial

invention of which I am a co-inventor, Patent application No.102023000018477, deposited on 08/09/2023 by the INFN Office for Technological Transfer [92]. The IAEA provides a database [77] that displays the location of cyclotron facilities world-wide with a list of their characteristics. Even though the hospital cyclotrons (E = 16-19 MeV) are greater in number, a significant number of operating cyclotrons, about 40, are able to produce proton beams of 30-35 MeV. Intermediate energy cyclotrons, like the ARRONAX facility in Nantes France and the SPES cyclotron at the LNL (Legnaro, Italy) laboratories, for which the energy beam can reach a max of 70 MeV, are adequate for the delivery of 35 MeV proton beams.

Generally, when the beam energy increases a larger amount of contaminants are produced. The innovation of the bilayer lies in the favourable coincidence of aligned layers of ^{nat}V and ^{50}Ti: at the time when for the rising of energy the production with ^{50}Ti is no more adequate due to the contaminants co-produced, the reaction with ^{nat}V starts to be suitable.

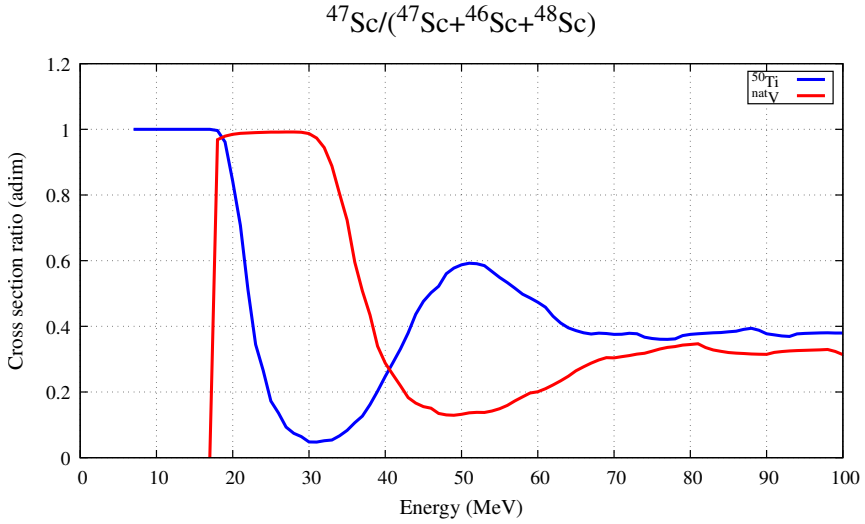

Figure 3.31 Cross sections ratio as a function of the energy of the protons for the reactions ^{nat}V(p,x)^{47}Sc (red line) and ^{50}Ti(p,x)^{47}Sc (blue line).

Fig. 3.31 shows the cross sections ratio as a function of the energy of the protons impinging on the target. The contribution related to each layer is shown separately, the blue line refers to the reaction with ^{50}Ti and the red one to the ^{nat}V layer. A ratio of about 1 means a small presence of contaminants in the production channel. It is evident that there is a difference between the two layers in term of favourable energies and this

clear separation can be exploited to maximize the production by simply adjusting the projectile energy to the corresponding layer. Essentially, a specific range of energy corresponds to a certain thickness of the target.

ISOTOPIA is a software package for the prediction of medical isotope production with charged-particle accelerators. The ISOTOPIA calculations refers to the IAEA medical isotope data library of about 150 reaction channels, complemented by TENDL-2017 for all other reactions [93,94]. The user provides the characteristics of the incident particle source, like the energy range, the specification of the target material, the power of the accelerator, the irradiation time and cooling time. The software returns, virtually and instantaneously, several quantities, like the yield of desired radionulides, information of the contamination, the thickness of the target.

The effective target thickness is here expressed in terms of the stopping power dE/dx. When the projectile travels through the target, its average energy decreases. The spreading of the beam inside the target is neglected. The amount of energy loss inside the target is determined by the target thickness and the stopping power. The limits on the projectile energy, E_{in} and E_{out}, are fixed by the user. The stopping power describes the average energy loss of projectiles in the target by atomic collisions as a function of their energy in [MeV/cm] according to the Bethe-Bloch formula [5]

$$\frac{dE}{dx} = 0.1535\rho\frac{Z}{A}\frac{z_p^2}{\beta^2}[ln(\frac{2m_e\gamma^2v^2W_{max}}{I^2}) - 2\beta^2] \tag{3.2}$$

where Z and A are the atomic number and atomic mass of the target, z_p and v are the charge and the velocity of the incident particle, r_e is the classical electron radius, m_e is the electron mass, c is the speed of light in the vacuum, W_{max} is the maximum energy transfer to an electron of the target by the incident particle with mass M in a single collision that for $M \gg m_e$. The quantities β and γ are the relativistic factors, indeed β

represents a beam particle traveling at a relative velocity

$$\beta = \frac{v}{c} = \sqrt{\frac{E_{beam}(E_{beam} + 2m_0c^2)}{(E_{beam} + m_0c^2)^2}} \tag{3.3}$$

with rest mass m_0.

From the Bethe-Block equation the thickness of the target is derived. Therefore, in the composite target the ^{nat}V has to be the first layer since its optimal energy range is between 35 and 22 MeV, that corresponds to 1.62 mm of thickness. For the second layer made of ^{50}Ti the purer production occurs within 22-9 MeV, namely 1.40 mm. In practise, by using intermediate energy cyclotrons and considering a beam of 35 MeV, the first layer of ^{nat}V guarantees a good ^{47}Sc production. When crossing a defined thickness of the layer the beam is degraded in energy down to a value suitable for being the optimal entrance energy for the second layer of ^{50}Ti. Here again, the reaction is competitive in the production. Hence, this setup is ideal to continuously produce ^{47}Sc with a high level of purity simply by placing side by side two different materials for which the best energies are one after the other. Two distinct setups, that differ in the initial energy, have been investigated and summarized in Table 3.6.

Target	Energy Range (MeV)	^{47}Sc	^{46}Sc	^{48}Sc	RNP
^{50}Ti	9-22	8.759	0.048	0.001	99.38
^{nat}V	22-35	4.203	0.016	0.0005	99.59
Bilayer	9-35	12.962	0.064	0.0015	99.448
^{50}Ti	9-22	8.759	0.048	0.001	99.38
^{nat}V	22-30	1.514	0.0006	0.0000007	99.96
Bilayer	9-30	10.273	0.0486	0.001	99.465

Table 3.6 Estimation of the activities for 1 h irradiation in a multilayer setup. The activities are expressed in MBq/μA.

The first and the second block of the Table differ in the maximum energy considered for the first layer of ^{nat}V and consequently in the results of the bilayer. The ^{50}Ti row is the same, since the energy range is fixed to 22-9 MeV. Under the same irradiation conditions, considering a projectile of 35 MeV that exits the ^{nat}V target with an energy

of 22 MeV, leads to a higher ^{47}Sc activity than the one obtained when 30 MeV is the initial proton energy. Obviously, moving to a wider range implies a larger amount of contaminants, as can be observed also in Fig. 3.31. At 35 MeV the red curve falls to 0.9, that means a significant reduction of the cross-section ratio. However, despite the bigger ^{46}Sc and ^{48}Sc presence, their impact on the final RNP is limited, as specified in the Table 3.6. The consequent lowering of the RNP from 99.448 to 99.465 for 35-22 and 30-22 MeV, respectively, do not alter the final outcome. The level of purity is still high and above the 99%. It follows that, the choice of the initial beam energy is not a matter of the level of purity achieved, but it only depends on the facility, so on the maximum supportable cyclotron energy. Since the higher energy corresponds a larger thickness of the layer, the difference between the two cases is given by the quantity of the employed ^{nat}V to build the target.

Target	Energy Range (MeV)	^{47}Sc	^{46}Sc	^{48}Sc	RNP
^{nat}V	9-35	4.227	0.016	0.0005	99.59
^{nat}V	9-30	1.538	0.0006	0.0000007	99.96

Table 3.7 Estimation of the activities obtained considering a single layer of ^{nat}V and proton beams of different energies. The activities are expressed in MBq/μA.

In addition, it is interesting to compare the differences after an irradiation of a single ^{nat}V target by proton beams and the results of the bilayer. Table 3.7 presents the activities produced when a mono-material target is irradiated. Again, a maximum beam energy of both 35 and 30 MeV has been considered, while the exit energy is fixed at 9 MeV. The wider the energy range the higher the contamination and the lower the RNP, even though it is always above 99% in both cases. Is is interesting to notice that the mono-target implies a higher purity, regardless the max energy, since the contaminants are produced only by the reaction with that specific target and there is no added contribution from a second channel. The drawback relies only on amount of ^{47}Sc produced by the reaction p-^{nat}V. It stands to reason that the bilayer has the advantage of two channels engaged in the ^{47}Sc production, and for both the co-production of contaminants is restricted. Notwithstanding a tiny reduction of the purity, the bilayer is an overwhelming advantage. With the bilayer is possible to achieve an increase of 300% and of 670% of the production for a maximum energy of 35 and 30 MeV,

respectively, guaranteeing in both setups a comparable RNP with the one accomplished in case of a single-layer target.

The previous analysis considers the use of ^{50}Ti targets with a 100% enrichment. Since this level of enrichment is not easily available in the market, a 98% enriched ^{50}Ti target has been investigated, considering the remaining 2% of ^{49}Ti. Among Sc-isotopes the ^{49}Ti produces the most critical contaminant, ^{46}Sc, in larger quantities. Thus, the choice of this isotopic composition of the target allows to examine a less favourable scenario due to a higher contamination and to verify the derived effect on the RNP.

The comparison of the productions at different levels of enrichment of the ^{50}Ti layer has been carried out for 1-h irradiation time, 1-μA current, and considering a proton beam energy of 9-35 MeV. Essentially, the difference lies only in the isotopic composition of the second layer of the target. Table 3.8 shows the variation in the activities and RNP when this change in the manufacture of the target is considered. The case of a 98% enriched ^{50}Ti target entails a 1.36% decrease of the ^{47}Sc production and only a 0.1% decrease of the RNP, although an increase of both ^{46}Sc and ^{48}Sc is observed.

Target	Energy Range (MeV)	^{47}Sc	^{46}Sc	^{48}Sc	RNP
Bilayer with 100% ^{50}Ti	9-35	12.962	0.064	0.0015	99.448
Bilayer with 98% ^{50}Ti	9-35	12.786	0.072	0.0045	99.355

Table 3.8 Comparison between the productions considering a bilayer made of a first layer of ^{nat}V and a second one of 100% enriched ^{50}Ti, or a second layer of 98% enriched ^{50}Ti. The activities are expressed in MBq/μA.

3.6.1 Conclusions

To conclude, the findings revealed that the reaction ^{49}Ti(p,x)^{47}Sc does not satisfy the RNP standard to guarantee a safe clinical application. The contamination, by both ^{48}Sc and ^{46}Sc, is too significant and therefore this route has to be rejected. On the other hand, a high-quality ^{47}Sc production is obtained with the nuclear reactions ^{49}Ti(d,x)^{47}Sc and ^{50}Ti(p,x)^{47}Sc, both characterized by a low contamination by ^{46}Sc and ^{48}Sc. For both cases it is possible to identify an optimal energy range in which the production of contaminants is limited. Specifically, the ideal energies are 5-10 MeV for the case deuterons on ^{49}Ti and 8-18 MeV when protons on ^{50}Ti are considered. It is

worth to notice that both reactions involve the use of low-energy beams, therefore both are eligible for a ^{47}Sc production at hospital cyclotrons. Another interesting method to produce high-quality ^{47}Sc concerns the use of protons from intermediate-energy cyclotrons on a bilayer made of ^{nat}V and ^{50}Ti. The innovation lies in exploiting for each layer the favourable energy ranges in which the co-production of contaminants is limited. Specifically, at the time when the energy is too high and the production with ^{50}Ti is no more adequate due to the co-produced contaminants, the reaction with ^{nat}V starts to be suitable for a high-quality ^{47}Sc production. Hence, the advantage in using the bilayer compared to a mono-element target is the higher production with no compromise on the quality.

Chapter 4

Manganese: from cross section to dosimetry

4.1 MultiModal Imaging: the Manganese case

The search and production of innovative radioisotopes for medical applications concerns also the advancement in multimodal imaging techniques, that is a simultaneous use of two different physical processes to obtain a more detailed diagnostic image information. PET/CT, PET/MRI, and SPECT/CT are examples that facilitates better detection of molecular, pathophysiological, and anatomic changes in a single scan acquisition after the administration of radiopharmaceutical and detection by the appropriate imaging modalities. Manganese is an essential element that participates as a co-factor in numerous enzymatic processes. The most stable oxidation state is manganese (II), the divalent manganese cation (Mn^{2+}). It behaves similarly to calcium and can diffuse through voltage-gated calcium channels in the brain, heart and pancreas. Increased activity in these tissues leads to an increased influx of Mn^{2+}; therefore, this cation can be used to monitor cell activity [95]. In addition, manganese is a unique tool for obtaining in vivo images of neural pathways because Mn^{2+} possesses strong paramagnetic properties and can be transported along the axons in an anterograde manner and cross synapses [96]. Therefore, Mn^{2+} has been used to obtain manganese-enhanced magnetic resonance imaging (MEMRI). This imaging technique enables early detection of neuronal function, intracellular ion balance, and axonal transport; nevertheless, it has not been widely used in clinical practice since the high doses of Mn^{2+} have been found to lead to a neurological disorder called manganism, with psychiatric and neurological syndromes similar to those of the Parkinson's disease [97]. Positron emission tomography (PET) provides increased detection sensitivity compared to MRI and allows all typical information from MEMRI to be obtained using trace levels of Mn^{2+}, thus minimizing its toxic effects [98]. Several radioisotopes of manganese have been studied as radiotracers for PET imaging [99]. Among them ^{52g}Mn appears the most suitable for this purpose because it decays with a low maximum positron energy of about 0.6 MeV, that provides PET imaging resolution similar to that of ^{18}F [95]. In addition, ^{52g}Mn

half-life ($t_{1/2}$ = 5.6 day) is long enough for in vivo imaging of cell tracking at time points as long as days or even weeks post-injection [100].

4.2 Cross section results

The best known production route is based on the reaction ^{nat}Cr(p,x)^{52g}Mn, where "*nat*" refers to the natural-elemental-abundance material. El Sayed et al [101] recently measured the cross-sections of ^{52g}Mn, and the co-produced contaminants ^{54}Mn and ^{51}Cr with the goal of optimizing the routine production of ^{52g}Mn. Experimental data were in good agreement with calculations obtained using the standard simulations with TALYS code, and with previously published data.

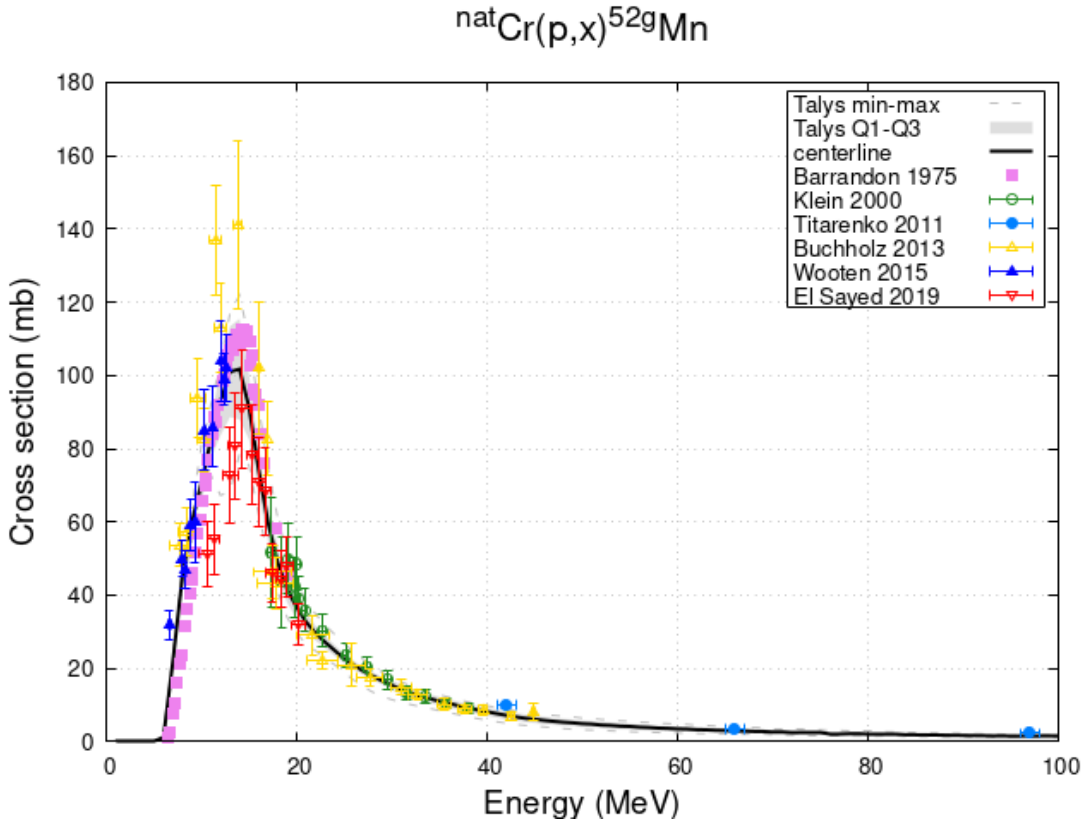

Figure 4.1 ^{52g}Mn cross section for the case protons on ^{nat}Cr.

Fig. 4.1 shows the variability of the TALYS models. For the reaction ^{nat}Cr(p,x) the min-max interval is quite limited and a narrow interquartile bands is observed. Hence, the centerline represents a good solution to reproduce the ^{52g}Mn cross section.

Recently, our group proposed an alternative reaction, ^{nat}V(α,x)^{52g}Mn, with potentially

higher yield and better RNP [22]. To obtain a cross-section in better agreement with the data, the optimization level density method, previously discussed in 3.3 paragraph, has been applied to the ^{nat}V(α,x)^{52g}Mn case. A specific combination of models has been selected on the basis of a general assessment. Since the experimental data are dispersed, the choice of which dataset to be considered to minimize the discrepancies between calculated and measured cross sections depends on the fact that the new c and p parameters should vary just a little to introduce a small perturbation and be more reliable in the description of the physics of the problem (A mention of the cumulatives is presented in [102]). On account of this, the curve of the optimized cross section follows the upper limit of the data bell.

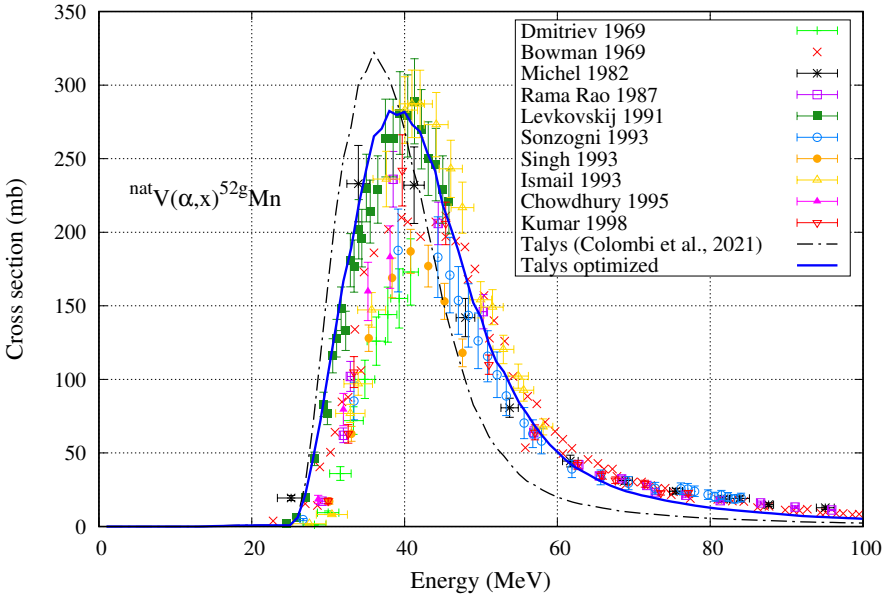

Figure 4.2 ^{52g}Mn cross section for the ^{nat}V case, comparing the available experimental data and two theoretical curves: the newly TALYS optimized curve (solid line) and the one used by Colombi et al. (dash-dot line).

The available experimental data [82, 103–113] reported in figure 4.2 were taken from the EXFOR database [114].

Specifically, the level density TALYS model, denoted as *ldmodel 6*, based on microscopic Hartree-Fock-Bogoliubov theory with the Gogny force, incorporating a temperature dependence in the level density [50], has been considered. Concerning the optical model, the default options for the nucleon-nucleus optical model and for the α-nucleus optical potential, corresponding to the model reported by Avrigeanu et

al [115] has been adopted. The pre-equilibrium reaction mechanisms were incorporated using the exciton model, where the different exciton states were coupled with transition rates calculated numerically starting from the imaginary part of the optical potential, that is *preeqmode 3* in the input parameters of the TALYS code. Starting from this combination of models a two-dimensional search grid to find the best solution for the c and p parameters has been introduced. Considering ^{52}Mn as the compound nucleus, the values $c = 0.0$ MeV$^{-1/2}$ and $p = -1.0$ MeV improve the cross section reproduction, as shown in figure 4.2 by the solid line. However, the $c = 0.0$ MeV$^{-1/2}$ implies that no normalization factor has been introduced with respect to the original microscopic Hartree-Fock level density, while a shift of 1 MeV has been applied towards higher energies, that could originate from shell-model or pairing effects.

In view of possible applications of manganese in medical imaging, it is important to evaluate the production of co-produced contaminants that could represent an obstacle limiting the RNP of the production route. For both reactions, ^{nat}V(α,x) and ^{nat}Cr(p,x), the contamination consists of radionuclides characterized either by a very short, or by a very long, half-life. In particular, ^{48}Mn, ^{49}Mn, $^{50g/m}$Mn, ^{51}Mn, and ^{52m}Mn have half-lives shorter than one hour and their contamination, both in terms of IP and RNP, are negligible just after a few hours. The stable ^{55}Mn is produced in the electromagnetic channel with very low yield, and the quasi stable ^{53}Mn (half-life $\sim 3.6\times10^6$ years) does not affect the RNP in a meaningful way. Finally, ^{54}Mn with an intermediate half-life of about 312 days represents the only radionuclide that could affect the purity of the final product.

Since ^{54}Mn is the main contaminant, its cross section has been assessed, as reported in figure 4.3. The agreement between the optimized theoretical curve and experimental data [82,108,110–113,116–118] is quite satisfactory. The calculations are rather stable with respect to the model variations, while the experimental data are spread within a 30% variability around the peak region.

The analysis of the cross sections allows to identify the optimal energy range that maximizes the production of ^{52g}Mn and minimizes the co-production of ^{54}Mn. For the

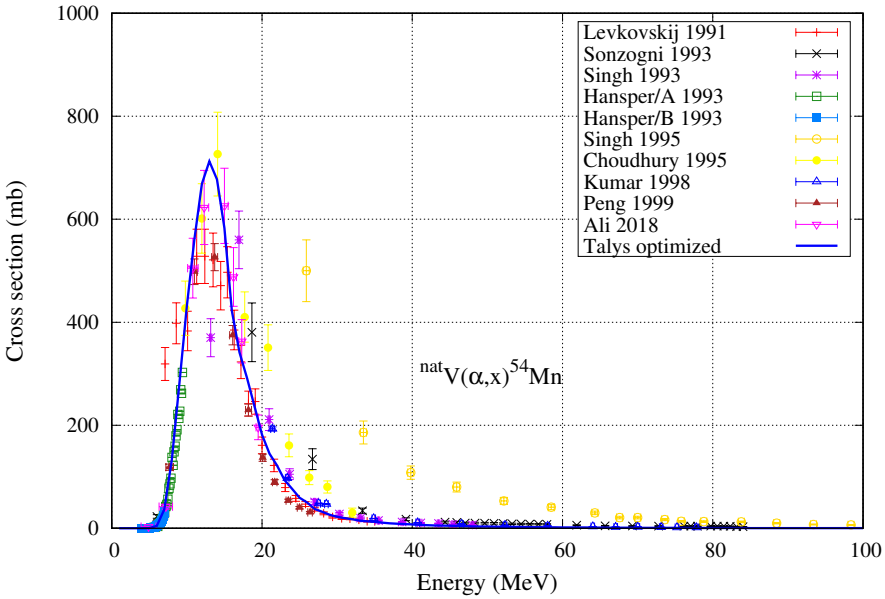

Figure 4.3 ^{54}Mn cross section and theoretical curve obtained with the optimization used in this work.

^{nat}V(α,x) route the peak of ^{52g}Mn is around 40 MeV, that corresponds to a minimum of the ^{54}Mn cross section. For the reaction ^{nat}Cr(p,x), instead, the highest production of ^{52g}Mn is reached around 15 MeV. Concerning the main contaminant, Figure 4.4 shows the ^{54}Mn cross section for the ^{nat}Cr case. The maximum of the production occurs at an energy range around 12 MeV, that is really close to the energy that corresponds to the ^{52g}Mn peak. Even though the ^{54}Mn cross section is smaller in comparison to the ^{52g}Mn one, to limit its contamination that could lessen the purity of the production route, the energy range has been selected by the tail of ^{54}Mn cross section. It follows that the two optimal energy windows that lead to an adequate production characterized by a sufficiently good quality for medical investigations are 48–33.9 MeV for the α–^{nat}V case and 17–14 MeV for the reaction protons on ^{nat}Cr targets. The energy intervals selected to improve the production and reduce the contamination correspond to a target thickness of 200-μm, for both reactions.

There is a crucial point to make: the wide dispersion of the data represents a challenging hindrance for a fully satisfactory reproduction of the ^{52g}Mn cross section. Fig. 4.5 takes into account the normalization of the Levkovskij [82] data by a 0.8 factor, due to the newest monitor analysis. The blue curve, that refers to the optimized calculation mentioned above, is now less precise in the cross section description at low energies,

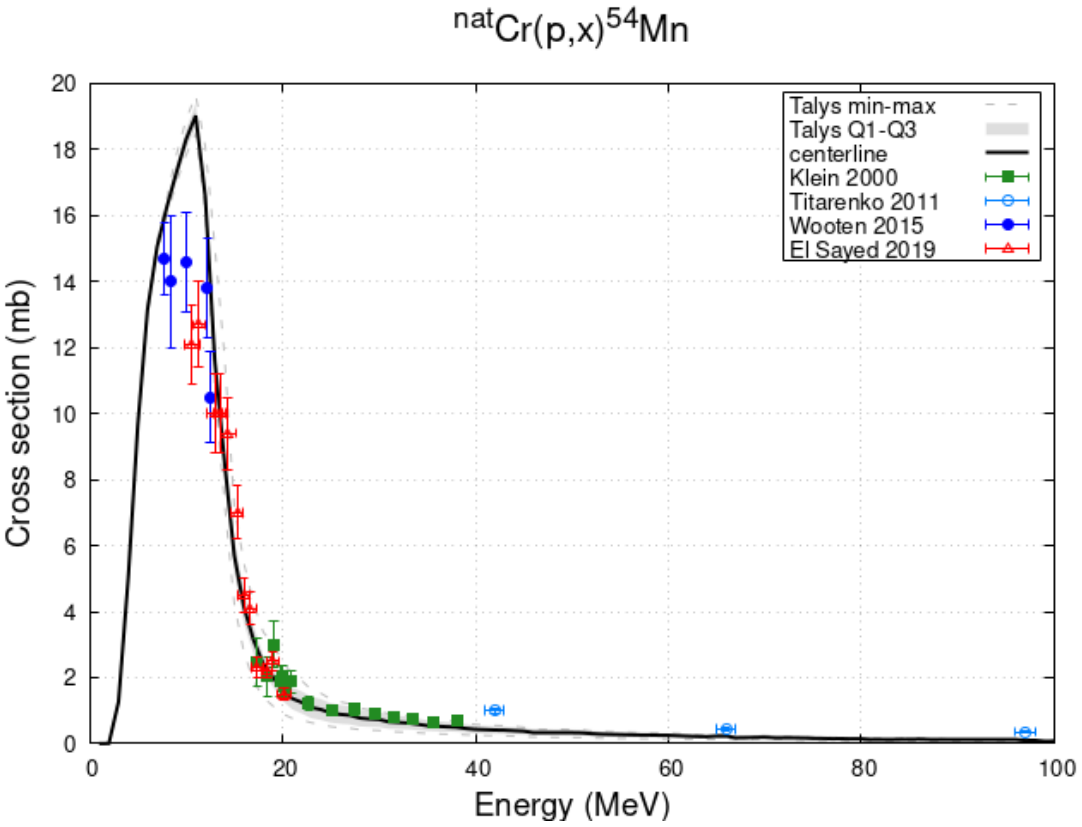

Figure 4.4 ^{54}Mn cross section for the reaction ^{nat}Cr(p,x).

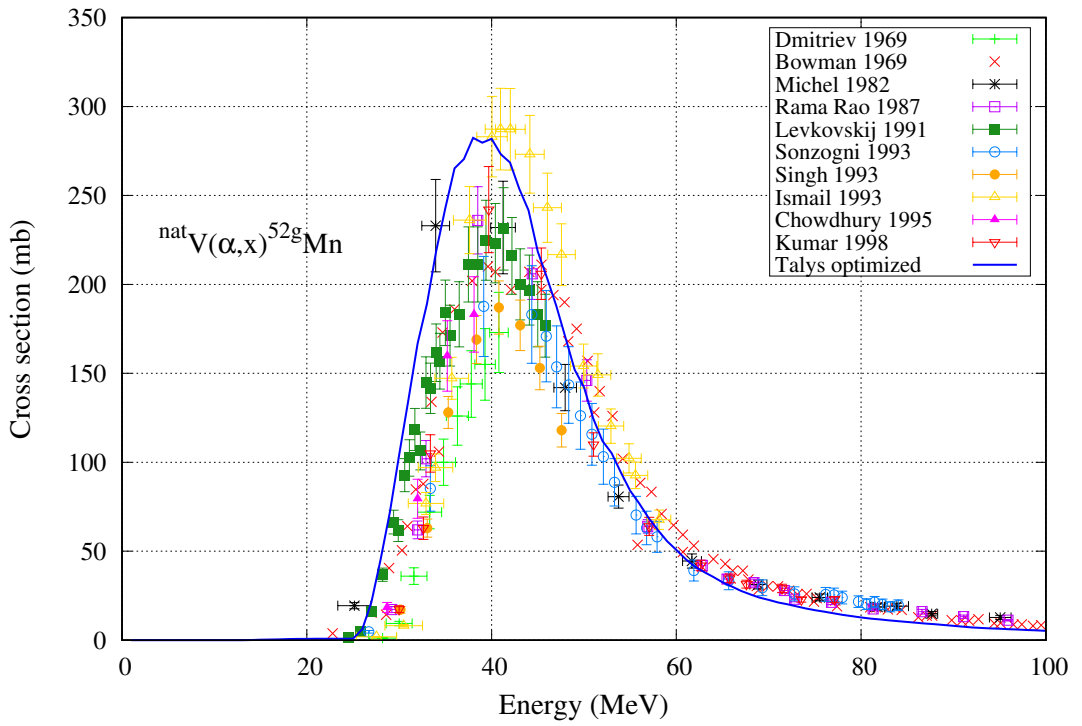

Figure 4.5 ^{52g}Mn cross section for the ^{nat}V case, considering a normalization of the Levkovskij data.

but still quite satisfactory around the peak and at higher energies. However, the re-normalization of a single dataset does not allow to overcome the issue and clarify which measurements are more trustworthy. A proper evaluation of all datasets by nuclear data experts might elucidate the situation. To date, the need of a reliable and recommended ^{52g}Mn cross section is strong.

4.3 Yields

The thick-target ^{52g}Mn production yields has been calculated at the EoB, assuming 1-*h* irradiation time and 1-μA beam current. For the ^{nat}V case the yield evaluation utilizes the newly optimized TALYS calculation of the cross section, discussed in 4.2 paragraph. Instead, for the reaction with the ^{nat}Cr target the predicted yield refers to the statistical analysis of the cross section. A good indicator to compare different reactions is the evaluation of the fraction of co-produced contaminants, that should be as low as possible to ensure a safe medical application. In table 4.1 the activities produced by the two given routes are listed. The ^{52g}Mn activity of 5.77 MBq for the case α-^{nat}V is larger than the activity for the p-^{nat}Cr reaction, that is 4.40 MBq. This greater production of the main radionuclide combined with a lower production of the long-lived ^{54}Mn ($T_{1/2}$ = 312.20 d) determines the ^{nat}V case as the most advantageous. However, even if the expected production of ^{51}Mn is slightly larger, this radionuclide can be eliminated with a few hours of decay post-production since it is a short lived contaminant ($T_{1/2}$ = 46 m).

target	beam	Energy Range (MeV)	A(^{52g}Mn)	A(^{51}Mn)	A(^{53}Mn)	A(^{54}Mn)
^{nat}V	α	[48 - 33.9]	5.77	9.38	1.7×10^{-8}	3.0×10^{-3}
^{nat}Cr	p	[17 - 14]	4.40	8.82	7.5×10^{-9}	4.9×10^{-3}

Table 4.1 Comparison of the activities at EoB for the two production routes. The activities are given in MBq/(μA·*h*).

The time-dependent relative activities of the radionuclides ^{52g}Mn, ^{51}Mn, ^{53}Mn, and ^{54}Mn are reported in figure 4.6. The curves represent the fraction of total activity of each radionuclide, and for the ^{52g}Mn case it corresponds to the standard definition of RNP (see Eq. **2.17**). The figure compares the two productions, the solid red line refers to ^{nat}V targets, the dashed blue one to the ^{nat}Cr. It is evident that the productions of

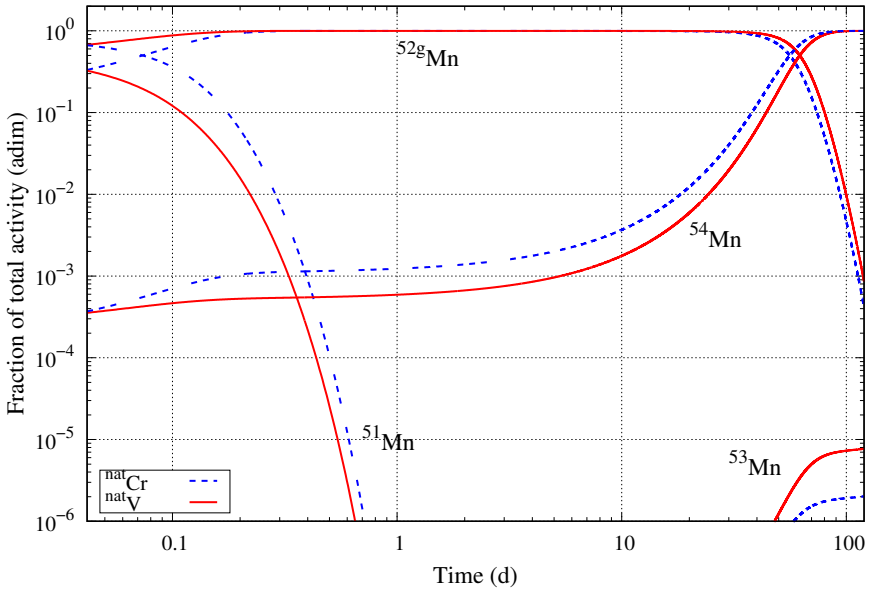

Figure 4.6 Ratio of the activity of the given ^{xx}Mn radionuclide with respect to the sum of all Mn ones. These fractions, in the case of ^{52g}Mn, coincide with the definition of RNP.

^{52g}Mn are comparable, while the use of α on ^{nat}V target provides a smaller contribution of the main contaminant, ^{54}Mn. Concerning the ^{51}Mn, its rapid decay is clear. The assessment of the fraction of the activities confirms the α-^{nat}V route more adequate thanks to a lower level of contamination.

4.4 Dosimetric studies

To ensure the safety of a radiopharmaceutical, the production methods should generate a minimal amount of radiogenic contaminants. The European Pharmacopoeia requires an extremely high RNP (the limit of 99% is suggested but not always mandatory) [53]. The control and the limitation of the fraction of radionuclidic impurities is a pivotal part of the demonstration that a specific route is promising for the production of a medical radionuclide, however it is not enough. It is essential to quantify the increase of the dose deposition in tissues due to the presence of these impurities, that may jeopardize the effectiveness of a treatment. Thus, to assess the validity of the results, it is of fundamental importance to carry out dosimetric studies to evaluate the impact of the produced radionuclides in terms of dose released to the patient, including the contribution of the contaminants. Nowadays, there is not an established limit for the DI, but in general 10% is considered a good starting value [76, 119]. The calculation of the

doses for a generic administration of 1 MBq of a radiopharmaceutical are carried out by using the software code OLINDA [54, 55]. For the evaluation of the total effective dose the activity of each radionuclide, previously calculated from yields, is multiplied by the corresponding absorbed dose obtained from the OLINDA simulations and then summarized over all radionuclides produced during the specific irradiation experiment. The optimization of the model parameters to better describe the cross sections allows to predict more precisely the activities due to a specific irradiation. Hence, merging the dosimetric results with an accurate estimation of the activities related to a certain irradiation is the real breakthrough of this research. Since the dosimetric calculations by OLINDA do not refer to a real experimental case, but are the expression of a general knowledge of the effective dose for a unitary activity of each radionuclide, they are not sufficient to draw solid conclusions, unless a more precise information of activities is included in the evaluation. In addition, the assessment of the dose imparted by the investigated radionuclides allows determining the best balance between activity and purity and to identify the time window after the End of Bombardment, i.e. the time after the end of the target irradiation, to label a radiopharmaceutical product with an acceptable DI to the patient. The effective dose burden in anthropomorphic phantoms due to the use of ^{52g}Mn has been evaluated considering the simple $MnCl_2$ chemical compound. Biodistribution data in healthy mice after [^{52g}Mn]Cl_2 injection [120], after scaling from mice to humans through the relative mass scaling method, were used to establish the biokinetic models used for human evaluation.

Below the dosimetric calculations are described step by step. The organ activity curves have been assessed after fitting the percent of injected activity in the main source organs, [% IA/organ]$_H$, derived from the equation **2.18** for both male and female models. The results show a fast uptake of Mn^{2+} for all the organs, followed by a slow wash-out, except for the salivary gland, where uptake remains quite stable. The number of disintegrations in the source organs per MBq of injected activity of $^{xx}MnCl_2$, obtained after integration of the organ activity curves, are reported in table 4.2 for each radioisotope. The activity reported by Hernandez et al [120] as [%IA/g] in "heart/blood" was assigned to "heart wall" and "heart contents" using equation (**2.18**) and the respective masses. As shown in table 4.2, for each radioisotope, the organ with the highest number of disintegrations

is the liver, followed by the kidneys for the radionuclides with the shortest half-life (^{51}Mn and ^{52g}Mn), by the salivary glands for the long-lived radionuclides ^{53}Mn and ^{54}Mn, due to the slow wash-out in this organ. Considering a total-body biological clearance based on the data of Mahoney and Small [121], the calculated number of disintegrations in the remaining organs clearly increases with the physical half-life of the radioisotope. Besides, the disappearance of manganese from the body in normal subjects is described by a curve having two exponential components. An average of about 70% of the injected material eliminated by a "slow" pathway with a biological half-time of 45 days and the rest through a "fast" pathway, with a half-time of 4 days.

	$[^{51}Mn]Cl_2$		$[^{52g}Mn]Cl_2$		$[^{53}Mn]Cl_2$		$[^{54}Mn]Cl_2$	
Tissue	Female	Male	Female	Male	Female	Male	Female	Male
Heart contents	1.37E-02	1.59E-02	0.882	1.00	3.63	4.12	3.43	3.89
Heart wall	9.38E-03	1.03E-02	0.596	0.647	2.46	2.66	2.32	2.51
Kidneys	2.64E-02	2.46E-02	2.24	2.07	4.75	4.49	4.65	4.39
Liver	8.54E-02	9.02E-02	6.93	7.32	13.2	13.9	13.0	13.7
Pancreas	1.15E-02	1.10E-02	1.20	1.15	2.67	2.58	2.62	2.53
Salivary gland	2.71E-03	2.72E-03	0.601	0.600	6.43	7.64	5.52	6.36
Remaining	9.44E-01	9.38E-01	33	132	1100	1100	963	961.45

Table 4.2 Number of nuclear transitions (MBq-h/MBq) in source organs per MBq of $^{xx}MnCl_2$, for female and male ICRP 89 phantoms.

Data from table 4.2 become the input for the evaluation of the absorbed doses to the organs for unit activity of each radioisotope and for both male and female phantoms. The ED are then derived from the ICRP 103 [59] tissue weighting factors. Results are presented in table 4.3. The organs receiving the highest doses are the kidneys, followed by the pancreas and the liver, in the case of $^{51}MnCl_2$, the pancreas, followed by the kidneys and liver, for $^{52g}MnCl_2$, both for male and female phantoms. The absorbed dose values obtained with the different radioisotopes are clearly correlated to their main decay data for dosimetric interest, reported in tables 4.4 and 4.5. Absorbed doses to different organs are 50-200 and 55-235 fold higher for $^{52g}MnCl_2$ compared to $^{51}MnCl_2$, respectively for male and female. This is due to the higher energy emitted by ^{52g}Mn per nuclear transformation (nt), 3.5335 MeV/nt, compared to 1.9321 MeV/nt for ^{51}Mn [2], and its longer half-life (see table 4.4). In the case of both $^{53}MnCl_2$ and $^{54}MnCl_2$, the organ receiving the highest dose becomes the salivary

glands. For these long half-lives radioisotopes the absorbed dose to the other organs becomes almost uniform, due to the preponderant contribution of total body irradiation (see the number of counts in Remaining organs in table 4.2). Despite the long half-life of ^{53}Mn, organ absorbed doses due to $^{53}MnCl_2$ are comparable to those due to $^{51}MnCl_2$, due to the very low radiation emission of this radioisotope, 0.0053 MeV/nt (ICRP107) (see table 4.4, 4.5). The total energy emitted per ^{54}Mn decay is about 4 times lower compared to ^{52g}Mn due to the absence of high-energy gamma emission, therefore organ absorbed doses due to $^{54}MnCl_2$ are only slightly higher than those due to $^{52g}MnCl_2$ despite the quite longer half life of ^{54}Mn. As already reported for other radiopharmaceuticals [122], organ absorbed doses are in general about 20% higher for female than for male, resulting in increased ED values between 33 and 38%, depending on the radioisotope. De Nardo et al. already reported in [123] that the ED values due to $^{51}MnCl_2$ injection are quite low and comparable to the ED of ^{18}F-FDG (0.0192 mSv/MBq; gender-averaged value) [56], and about two orders of magnitude lower than those of $^{52g}MnCl_2$. The ED values due to $^{53}MnCl_2$ are less than a factor 3 higher than those due to $^{51}MnCl_2$, while those of $^{54}MnCl_2$ are about a factor 1.5 higher than those due to $^{52g}MnCl_2$.

The main decay data of interest for the present analysis are reported in tables 4.4 and 4.5. These data were extracted with the software package DECDATA provided by the ICRP 107 publication [2].

Figure 4.7 compares the time evolution of DI for both production routes and considering both anthropomorphic OLINDA phantoms. Specifically, the red lines refers to the ^{nat}V target and the blue ones to the ^{nat}Cr case. The distinction between solid and dashed lines shows the differences in the DI for female and male OLINDA phantoms, respectively. Table 4.6 completes and simplifies the discussion of the results.

In general, both production routes satisfy the requirement of having a RNP greater than 99% for a long time window, as reported in Tab.4.6. The lower time limit depends on the ^{51}Mn fast decay and the upper extreme on the slow decay of ^{54}Mn. More precisely, the comparison shows a longer time interval that matches the RNP limit for

	$[^{51}Mn]Cl_2$		$[^{52g}Mn]Cl_2$		$[^{53}Mn]Cl_2$		$[^{54}Mn]Cl_2$	
Tissue	Female	Male	Female	Male	Female	Male	Female	Male
Adrenals	1.83E-02	1.67E-02	2.65	2.27	4.22E-02	3.47E-02	3.39	2.69
Brain	1.14E-02	9.27E-03	1.43	1.15	4.22E-02	3.47E-02	2.46	1.98
Breasts	1.14E-02	-	1.35	-	4.22E-02	-	2.14	-
Esophagus	1.32E-02	1.09E-02	1.76	1.56	4.22E-02	3.47E-02	2.48	2.31
Eyes	1.14E-02	9.26E-03	1.43	1.14	4.22E-02	3.47E-02	2.45	1.95
Gallbladder Wall	1.49E-02	1.44E-02	2.41	2.24	4.22E-02	3.47E-02	3.24	2.75
Left Colon	1.37E-02	1.15E-02	2.22	1.90	4.22E-02	3.47E-02	3.57	2.97
Small Intestine	1.33E-02	1.13E-02	2.07	1.88	4.22E-02	3.47E-02	3.27	3.06
Stomach Wall	1.39E-02	1.19E-02	2.21	1.87	4.22E-02	3.47E-02	3.37	2.70
Right Colon	1.38E-02	1.14E-02	2.26	1.89	4.22E-02	3.47E-02	3.61	2.91
Rectum	1.30E-02	1.06E-02	2.12	1.74	4.22E-02	3.47E-02	3.66	2.99
Heart Wall	3.56E-02	3.02E-02	2.16	1.82	3.39E-02	2.78E-02	2.98	2.33
Kidneys	5.66E-02	4.71E-02	3.12	2.58	3.96E-02	3.33E-02	3.19	2.61
Liver	4.05E-02	3.34E-02	2.90	2.37	2.17E-02	1.78E-02	2.77	2.18
Lungs	1.33E-02	1.07E-02	1.82	1.44	4.22E-02	3.47E-02	2.83	2.20
Ovaries	1.31E-02	-	2.17	-	4.22E-02	-	3.71	-
Pancreas	5.75E-02	4.68E-02	3.70	3.00	5.12E-02	4.24E-02	3.78	3.11
Prostate	-	1.06E-02	-	1.72	-	3.47E-02	-	2.94
Salivary Glands	2.17E-02	1.83E-02	2.27	2.01	2.11E-01	2.07E-01	3.93	3.73
Red Marrow	1.01E-02	8.32E-03	1.84	1.47	4.22E-02	3.47E-02	3.05	2.46
Osteogenic Cells	8.01E-03	7.59E-03	1.88	1.55	1.54E-02	1.65E-02	3.25	2.81
Spleen	1.42E-02	1.11E-02	2.18	1.71	4.22E-02	3.47E-02	3.29	2.66
Testes	-	9.64E-03	-	1.33	-	3.47E-02	-	2.29
Thymus	1.31E-02	1.09E-02	1.87	1.49	4.22E-02	3.47E-02	2.98	2.32
Thyroid	1.19E-02	1.00E-02	1.60	1.45	4.22E-02	3.47E-02	2.68	2.45
Urinary Bladder Wall	1.19E-02	1.05E-02	1.56	1.70	4.22E-02	3.47E-02	2.65	2.94
Uterus	1.31E-02	-	2.14	-	4.22E-02	-	3.68	-
Total Body	1.35E-02	1.10E-02	1.70	1.37	4.34E-02	3.58E-02	2.72	2.28
ED (ICRP 103)	1.36E-02	1.02E-02	1.79	1.35	3.89E-02	2.82E-02	2.73	2.02

Table 4.3 The absorbed doses (mSv/MBq) calculated for ^{xx}MnCl2 with the OLINDA v2.2 software for female and male ICRP 89 phantoms using the data of table 4.2, and ED (mSv/MBq) values based on the ICRP 103 tissue weighting factors.

the ^{nat}V case due to a larger production of ^{52g}Mn and a lower ^{54}Mn contamination, as inspected also from figure 4.6. The large production of the short-lived ^{51}Mn affects the purity only in the short term, while the ^{53}Mn has a negligible impact well beyond the time interval of interest. On the other hand ^{51}Mn could be considered an additional (fast-decaying) radionuclide for PET diagnostics [21] to be used in co-prodution with ^{52g}Mn. Concerning the DI, it increases with time in both cases. However, the use of α particles on ^{nat}V targets guarantees a remarkably longer time window during which the total effective dose is less than 110% with respect to an hypothetical pure ^{52g}Mn injection. The time ranges that satisfy the DI condition (increase of the dose due to the impurities below the 10% limit) are reported in table 4.6 and, again, for the ^{nat}V

Radioisotope	^{51}Mn; Half-life: 46.2 m; Decay: EC, β^+			^{52g}Mn; Half-life: 5.591 d; Decay: EC, β^+		
Radiations	Yield (/nt)	E (MeV/nt)	Mean E (MeV)	Yield (/nt)	E (MeV/nt)	Mean E (MeV)
Gamma rays	5.242×10^{-3}	5.451×10^{-3}	1.040	3.000	3.154	1.051
X rays	1.943×10^{-1}	3.968×10^{-5}	2.042×10^{-4}	4.697	9.588×10^{-4}	2.042×10^{-4}
Annh. Photons	1.942	9.922×10^{-1}	5.11×10^{-1}	5.932×10^{-1}	3.031×10^{-1}	5.11×10^{-1}
Tot photons	-	0.9977	-	-	3.4585	-
β^+	9.709×10^{-1}	9.342×10^{-1}	9.623×10^{-1}	2.966×10^{-1}	7.172×10^{-2}	2.418×10^{-1}
β^-	-	-	-	-	-	-
IC electrons	1.130×10^{-6}	9.231×10^{-7}	8.165×10^{-1}	6.004×10^{-4}	5.109×10^{-4}	8.509×10^{-1}
Auger electrons	1.580×10^{-1}	1.167×10^{-4}	7.388×10^{-4}	3.818	2.820×10^{-3}	7.386×10^{-4}
Tot electrons	-	0.9344	-	-	0.0750	-
Tot	-	1.9321	-	-	3.5335	-

Table 4.4 Main decay data of the ^{51}Mn and ^{52g}Mn radionuclides extracted with the software package DECDATA provided by the ICRP 107 publication. For each radiation type, the yield or number per nuclear transformation (nt), the total emitted energy (MeV per nt), the mean (average) emitted energy (MeV) are reported.

Radioisotope	^{53}Mn; Half-life: 3.7×10^6 y; Decay: EC			^{54}Mn; Half-life: 312.12 d; Decay: EC, β^+, β^-		
Radiations	Yield (/nt)	E (MeV/nt)	Mean E (MeV)	Yield (/nt)	E (MeV/nt)	Mean E (MeV)
Gamma rays	-	-	-	9.998×10^{-1}	8.346×10^{-1}	8.348×10^{-1}
X rays	6.662	1.356×10^{-3}	2.035×10^{-4}	6.670	1.360×10^{-3}	2.039×10^{-4}
Annh. Photons	-	-	-	1.120×10^{-8}	5.723×10^{-9}	5.11×10^{-1}
Tot photons	-	0.0014	-	-	0.8360	-
β^+	-	-	-	5.600×10^{-9}	1.019×10^{-9}	1.820×10^{-1}
β^-	-	-	-	2.448×10^{-4}	2.03×10^{-4}	8.293×10^{-1}
IC electrons	-	-	-	2.448×10^{-4}	2.03×10^{-4}	8.293×10^{-1}
Auger electrons	5.415	3.989×10^{-3}	7.367×10^{-4}	5.422	4.001×10^{-3}	7.379×10^{-4}
Tot electrons	-	0.0040	-	-	0.0042	-
Tot	-	0.0053	-	-	0.8402	-

Table 4.5 Main decay data of the ^{53}Mn and ^{54}Mn radionuclides. For explanation see table 4.4.

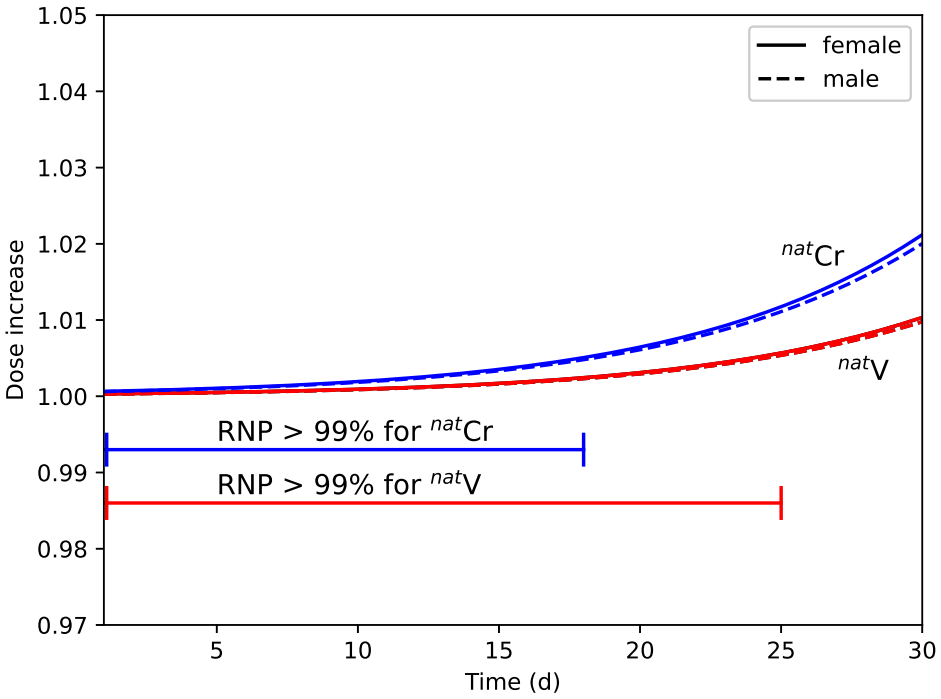

Figure 4.7 Time evolution of the DI for the two production routes and for female/male phantoms. The blue and red lines refer to the ^{nat}Cr(p,x) and ^{nat}V(α,x) reactions, respectively. The horizontal lines indicate the time ranges allowed by the 99% RNP limits.

Target	Radionuclidic purity	Dose Increase	
	Time range (day)	Time range (day)	
		female	male
^{nat}V	0.28 - 24.35	0 - 50.21	0 - 50.78
^{nat}Cr	0.29 - 18.28	0 - 44.14	0 - 44.71

Table 4.6 Time range that satisfies the requirement of at least 99% RNP for both production routes. Time range for which the DI is maintained within the limit of 10% for both Adult Female and Male OLINDA phantoms.

case it is longer. Nevertheless, on the basis of the time ranges identified from the calculations of the RNP and DI, the results on RNP settle a more stringent condition than the DI outcome, as also put in evidence in figure 4.7 by the two horizontal bars. The DI obtained in the hypothesis of injecting $^{52g}MnCl_2$, within the time window corresponding to a RNP greater than 99%, is lower than 0.1% and 0.3%, respectively for ^{nat}V and ^{nat}Cr targets. This excellent result suggests and confirms the advantage in using the α on ^{nat}V targets thanks to the very low increase of the dose to the patients' organs. It should be remembered that the result concerning the DI are specific for

each radiopharmaceutical, since it depends on its biokinetics. The injection of another compound, due to the diverse coordination chemistry, would lead to a distinct kinetics and then a different outcome.

To conclude, the favourable findings describe the nuclear reaction ^{nat}V(α,x)^{52g}Mn as a valid and promising alternative to the standard production route. Although, it must be acknowledged that the use of α particles at intermediate energies requires more complex (and less widespread) facilities than those providing low-energy proton beams, like standard hospital cyclotrons. Moreover, the discussion has been limited here to the use of natural targets which are easily available and usually inexpensive. It is known that enriched targets perform more efficiently but require more expensive materials and complicated target-recovery approaches [22].

Chapter 5

Terbium

5.1 Background

Terbium is one of the few rare earth radiometals that could be used in nuclear medicine for tumor diagnosis and treatment, due to the favorable physical decay properties such as half-lives, type and energy of emissions. The four Tb radionuclides with higher clinical interest are ^{152}Tb and ^{155}Tb, positron and gamma emitters respectively, relevant for diagnostic purposes, and ^{149}Tb and ^{161}Tb, α and β^- emitters respectively, suitable for therapeutic applications [124]. The advantage lies in the possibility to match radioisotopes that belong to the same element to produce therapy-diagnostic pairs with no differences in chemical and pharmacokinetics behaviours in compliance with the keynote of theranostic, namely the absolute certainty to reach the sensitive target visualized through imaging scans even at the therapy stage [11]. On the contrary, the drawback of using pairs made of diverse elements for diagnostics and therapy may not accomplish the theranostic goal, since each metal ion has specific chemical characteristics and this influences the pharmacological properties of the labelled molecules [125].

Among Tb isotopes, only ^{155}Tb is suitable for SPECT imaging, thanks to its two γ emissions at 87 keV (32%) and 105 keV (25%). Preclinical studies in nude mice bearing tumor xenograft demonstrated that ^{155}Tb-labelled biomolecules were able to visualize tumor sites using a small-animal SPECT/CT scanner even 7 days after radiocomplexes administration [126]. ^{155}Tb has been produced by different methods although most of them generated a large number of isotopes. First investigations on the production of ^{155}Tb via proton-induced reactions on Gd targets date back to 1989 with the work by Dmitriev et al. [127]. In this case, no cross section measurements were performed, but rather irradiation experiments of ^{nat}Gd thick targets for yields and activities, with incident proton energies between 11 and 22 MeV. Using ^{nat}Gd targets, cross-section measurements were performed in 2012 by Vermeulen et al. [128]. Besides the detailed experimental work that included the measurement of cross sections for the formation

of a variety of terbium radionuclides, theoretical calculations were also performed for all contributing reactions. Since natural Gd (^{nat}Gd) has seven isotopes it is not suited as target material for radioisotope production with high radionucludic purity (RNP). Therefore, comparisons were made with accurate theoretical simulations in order to identify the most promising reactions that could be effectively employed in studies with enriched targets. More recently Formento-Cavaier et al. [129] extended the measurements with ^{nat}Gd targets up to 70 MeV. Experimental investigations with enriched targets of ^{155}Gd and ^{156}Gd have been undertaken by Favaretto et al. [130], with the result that ^{156}Gd(p,2n)^{155}Tb provides high production yields, but implies the use of higher-energy cyclotrons and a significant contamination by the co-production of ^{156}Tb. The ^{155}Gd(p,n)^{155}Tb reaction, on the other hand, can be performed with medical cyclotrons, with incident protons up to around 18 or 20 MeV, and has the potential to provide significant yields with high purity. In a subsequent publication Dellepiane et al. [131] used the same enriched gadolinium oxide (^{155}Gd 91.9% enrichment or ^{156}Gd 93.3% enrichment) as target materials, measuring the ^{155}Tb production cross sections as well as a variety of contaminants produced for such highly enriched targets. In the most favorable case of the ^{155}Gd target, using an input energy of 10.5 MeV, contamination from ^{156}Tb was still significant, leading to a maximum RNP not greater than 93% after a decay time of about 96 h. Thus it was suggested, as possible solution, to purify the final product through an off-line mass separation technique at the expense of a lower production yield, due the low efficiency of the current mass separation approaches. The production of ^{155}Tb and other Tb-isotopes (^{149}Tb and ^{152}Tb) has been explored also at CERN-ISOLDE using spallation of high-energy p-beams on Tantalum targets, followed by ionization and mass separation [124, 132]. At CERN-MEDICIS external target produced in cyclotrons such as at ARRONAX are also used to go through a mass separation process and separate Tb-155 from all other Tb present in the target [17]. ^{161}Tb is instead produced by irradiation of enriched ^{160}Gd targets for 3 weeks at the spallation-induced neutron source (SINQ) at PSI (Villigen-PSI, Switzerland) or by irradiation for 1 week at the high-flux nuclear reactor of ILL (Grenoble, France) [133]. ^{161}Tb is also routinely produced at SCK CEN in Mol, Belgium. The drawback stands in the limited quantity of ^{155}Tb that can be produced with this method, due to the observed low efficiency of the accumulation procedure [134, 135]. It has been

Table 5.1 Main decay data (decay mode, half-life, emitted energy per nuclear transformation (nt) in the form of electron, photon, and the total one) of ^{xxx}Tb radionuclides. These data were extracted with the software package DECDATA provided by the ICRP 107 publication [2], while data for ^{154m1}Tb and ^{154m2}Tb were obtained by NUDAT3 database. Recently the ^{155}Tb half-life has been re-assessed [3], however all calculations refer to the old evaluation reported in this Table.

Radionuclide	Decay mode (%)	$T_{1/2}$	Emitted energy (MeV/nt)		
			Electron	Photon	Total
^{153}Tb	EC (100%)	2.34 d	0.0481	0.3318	0.3800
^{154g}Tb	EC (100%), $\beta^- < 0.10\%$	21.5 h	0.0681	2.2831	2.3512
^{154m1}Tb*	EC (78.20%),IT (21.80%), $\beta^- < 0.10\%$	9.4 h	—	—	—
^{154m2}Tb*	EC (98.20%), IT (1.80%)	22.7 h	—	—	—
^{155}Tb	EC (100%)	5.32 d	0.0434	0.1777	0.2211
^{156g}Tb	EC (100%)	5.35 d	0.0835	1.9371	2.0206
^{156m1}Tb	IT (100%)	24.4 h	0.0171	0.0370	0.0540
^{156m2}Tb	IT (100%)	5.3 h	0.0874	0.0048	0.0922

* data not provided by [2].

suggested also to irradiate a ^{159}Tb target by intermediate energy (60, 70 MeV) p beams [136, 137]. This would open the possibility to have a ^{155}Dy/^{155}Tb generator system, similarly to the renowned ^{99}Mo/^{99m}Tc one. However, the double separation chemistry among lanthanides represents a crucial step that still needs to be solved and the possible co-production of very long-lived terbium contaminants could imply a too low specific activity.

5.2 Cross section

The analysis of the cross section focuses on the production of ^{155}Tb and the contaminants ^{153}Tb, ^{154g,m1,m2}Tb, and ^{156g,m1,m2}Tb via the nuclear reaction ^{155}Gd(p,x). In table 5.1 the main decay data of the radionuclides of interest are reported. It is evident that ^{156g}Tb, whose half-life is 5.35 days, comparable with the ^{155}Tb one of 5.32 days, is the contaminant of greater concern for this production route. This means that the potential reduction of the purity of the final product may be ascribed to the ^{156g}Tb presence. The cross sections evaluation allows to achieve the goal of tracing the origin of its production in terms of irradiation conditions and level of enrichment of the target.

For the theoretical reproduction of the cross sections the same composition of the enriched ^{155}Gd targets employed by Dellepiane has been simulated. Specifically, ^{152}Gd $< 0.02\%$; ^{154}Gd 0.5%; ^{155}Gd 91.90%; ^{156}Gd 5.87%; ^{157}Gd 0.81%; ^{158}Gd 0.65%; ^{160}Gd

0.27%. In Fig. 5.1 the gray band represents the models variability between Q1 and Q3, the dashed lines are the minimum/maximum values of the cross section obtained with all models, and the blue solid line is the TALYS default option (PE2-LD1), commonly referred to as the standard simulation in the Literature. For the ^{155}Tb case all models reproduce equally the cross section up to 10 MeV, and for higher energy the band is relatively thin and this corresponds to a limited model variabiality, as expected from a typical (p,n) reaction. On account of this, and because the TALYS default reproduces the very recent data measured by Dellepiane et al. [131] quite satisfactorly, the analysis will be presented considering the TALYS default as the benchmark calculation.

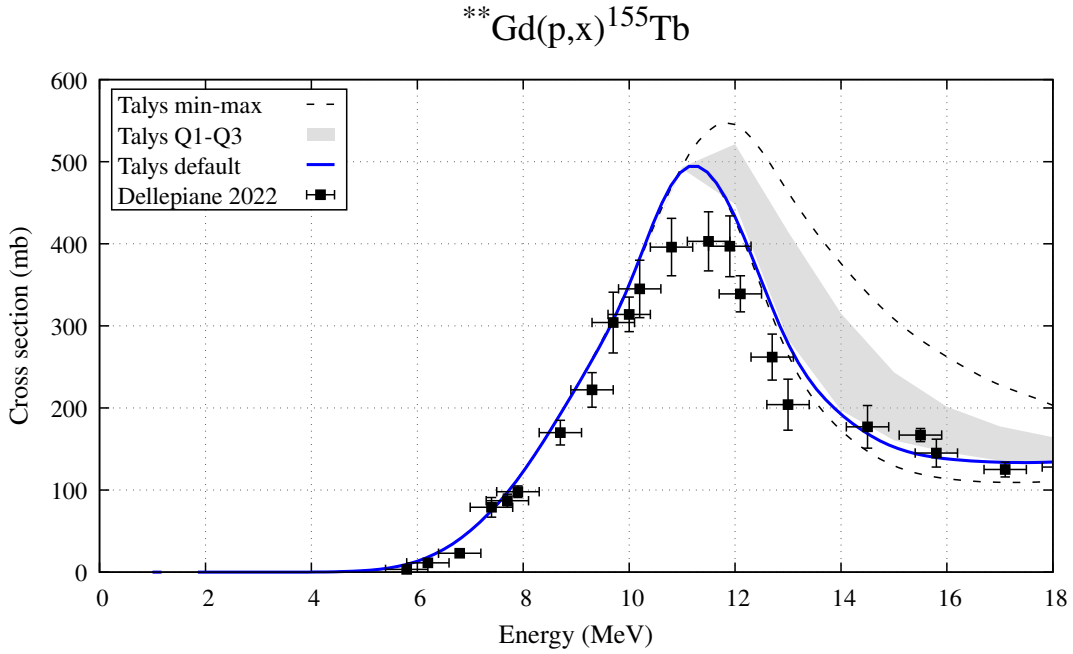

Figure 5.1 ^{155}Tb cross section from enriched ^{155}Gd target and theoretical curve. The two stars (**) refer to the target isotopic composition used by Dellepiane.

Once the agreement between theoretical cross section and data has been verified, it is of great interest to assess how the Terbium radionuclides production is related to the isotopic components of the target. Fig.5.2 shows the Gadolinium isotopes that produce ^{155}Tb.

The main contribution to the ^{155}Tb cross-section comes, as should be expected, from the (largest) ^{155}Gd component of the target. At about 10 MeV, also the contribution from the ^{156}Gd component becomes significant, and this explains the increase of the experimental data with respect to an ideal target with 100% ^{155}Gd enrichment. The

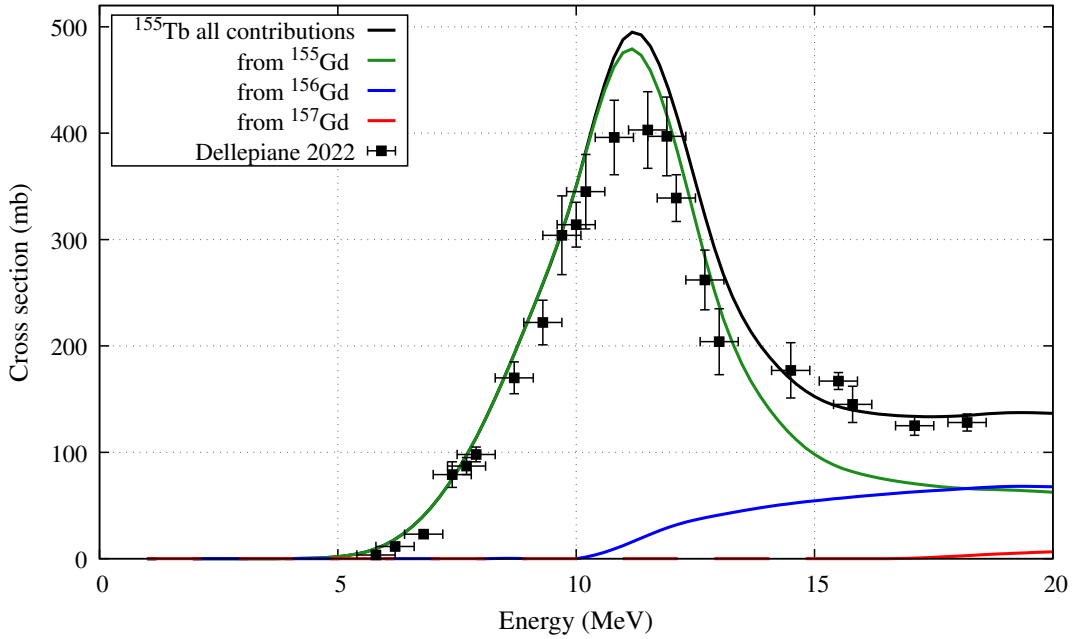

Figure 5.2 ^{155}Tb cross section from enriched ^{155}Gd target: TALYS calculations and contributions from different Gd isotopes in the target.

contribution from ^{157}Gd is quite small and that from other Gadolinium components of the targets, such as ^{154}Gd, is negligible.

The production of the main contaminant ^{156}Tb is presented in Fig. 5.3. Panel A refers to the ^{156t}Tb total cross-section, the cumulative cross sections of ^{156g,156m1,156m2}Tb (ground and the first two metastable states). The curve including all contributions is in agreement with the data measured by Dellepiane. It is evident that the principal contribution belongs to the ^{156}Gd component of the target, followed by the ^{157}Gd component at slightly higher energies. At even higher energies, about 19 MeV, also the contribution from ^{158}Gd becomes significant. Instead, the effect to the ^{156}Tb cross section from the main ^{155}Gd component of the target remains quite small in the entire range of considered energies. Panels B, C, and D describe the ^{156}Tb production cross sections for ground and the two metastable states, respectively. For the ground state, the model calculations are in fair agreement with the measurements, although at higher energies there is a tendency to underestimate the data. For the first metastable state there are no measured production data, while for the second one the curves underestimate the measurements. In all cases, by separating in the Gd target the individual isotopic components, it is evident that the main contributions to the

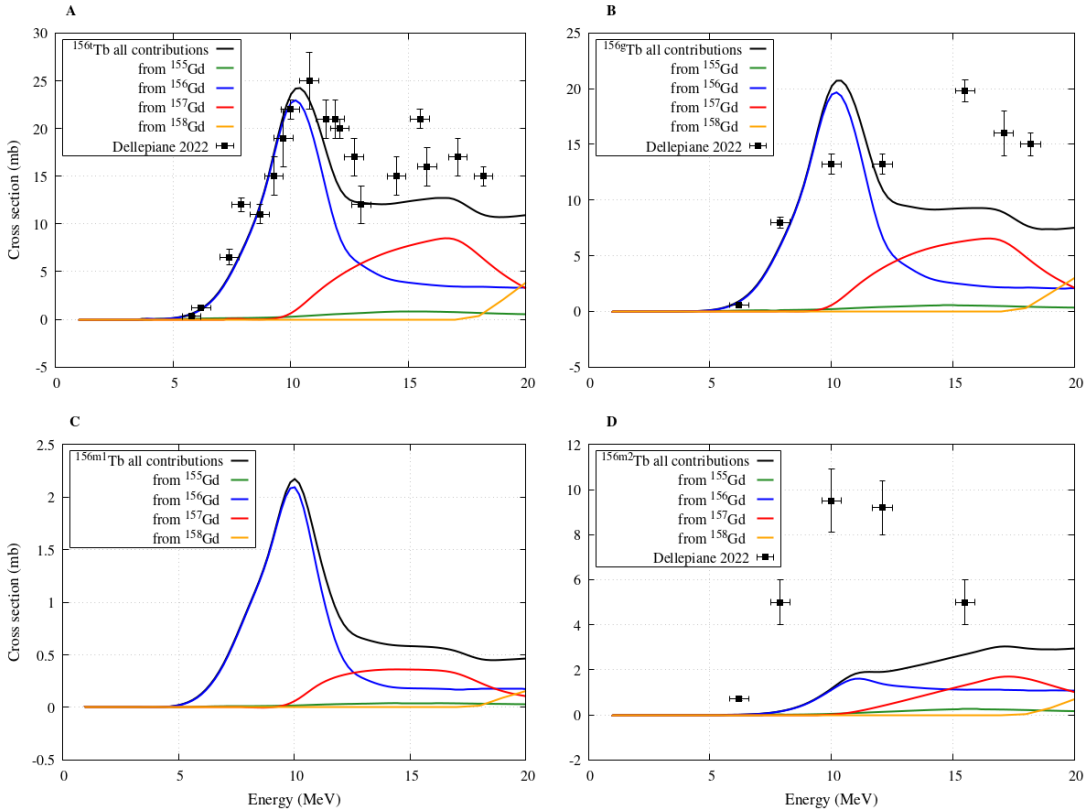

Figure 5.3 ^{156g,156m1,156m2,156t}Tb (where t is the cumulative cross section of ^{156g,156m1,156m2}Tb) cross sections from enriched ^{155}Gd target: TALYS calculations and contributions from different Gd isotopes in the target.

production of the contaminants derive from the Gd isotopes heavier than 155.

The remaining contaminants that may have an impact on the quality of the production are ^{153}Tb and ^{154}Tb (separated in ground and the first two metastable states) and their cross sections are given in Fig. 5.4. The theoretical curves are in clear agreement with the measurements, with the exception of ^{154m2}Tb where slight discrepancies can be observed. In all figures it is evident that the contamination at energies lower that 10 MeV can be entirely ascribed to the small presence of ^{154}Gd in the target, responsible of a characteristic bump seen in the lower energy data. At higher energies, ^{155}Gd becomes the principal contributor to the production of these contaminants.

5.3 Yields

The analysis of the cross section bring to the conclusion that the ^{156}Tb contamination grows proportionally with the fraction of ^{156}Gd in the target. To examine which target enrichment is necessary to obtain a sufficient and high-quality production four cases

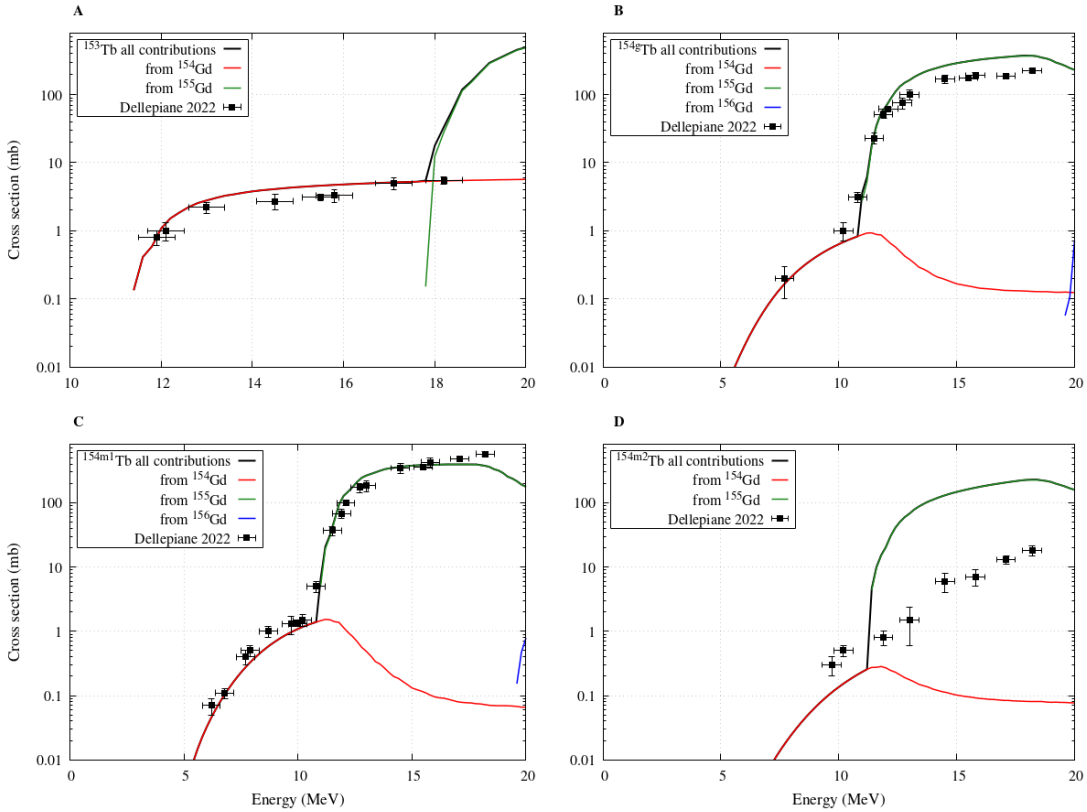

Figure 5.4 ^{153,154g,154m1,154m2}Tb cross sections from enriched ^{155}Gd target: TALYS calculations and contributions from different Gd isotopes of the target.

have been investigated. By listing, a 91.90% enrichment that refers to the Dellepiane target, a 98% and 99% with an impurity made of only ^{156}Gd, and the ideal target 100% enriched. The yields, isotopic, and radionuclidic purities have been assessed for all different target compositions. For all cases the irradiation conditions have been set to 1 µA current, 1 h irradiation time and 10.5-8 MeV energy interval.

Table 5.2 reports the yields of the main Tb radionuclides involved in the production. The ^{156}Tb contamination grows proportionally with the fraction of ^{156}Gd in the target. The ^{154g,m1,m2}Tb contamination remains small and stable at varying the ^{156}Gd component in the target. It increases only if the target contains a fraction of ^{154}Gd, as is the case for the target employed by Dellepiane, with a 0.5% contribution. At the selected energy range the production of ^{153}Tb is negligible in all cases, therefore it is not reported in the table. In addition, yields at 72 h and 96 h after EoB are shown. At these times the activities of ^{154g}Tb and all metastable states are considerably reduced, since their half lives are about 1 d or less.

Table 5.2 ^{xxx}Tb radioisotopes yields (MBq/μA·h) for different ^{155}Gd- enriched targets at the EoB, 72, and 96 h after.

	Yield (MBq/μA· h)						
Target enrichment	^{155}Tb	^{156g}Tb	^{156m1}Tb	^{156m2}Tb	^{154g}Tb	^{154m1}Tb	^{154m2}Tb
^{155}Gd-100% [EoB]	4.383	0.0027	0.0013	0.0121	0.0293	0.121	0.0
^{155}Gd-99% [EoB]	4.3424	0.03743	0.0217	0.05467	0.0290	0.120	0.0
^{155}Gd-98% [EoB]	4.3021	0.07209	0.04214	0.0972	0.0287	0.119	0.0
^{155}Gd-91.90% [EoB]	4.04829	0.2123	0.12422	0.2682	0.07016	0.274	0.008
^{155}Gd-100% [72 h]	2.9648	0.00239	0.00017	9.85E-7	0.00479	0.0006	0.0
^{155}Gd-99% [72 h]	2.9375	0.02977	0.00281	4.4496E-6	0.00475	0.0006	0.0
^{155}Gd-98% [72 h]	2.910	0.057	0.0054	7.91E-6	0.004698	0.0006	0.0
^{155}Gd-91.90% [72 h]	2.73853	0.16776	0.01144	2.183E-5	0.01125	0.0013	0.0009
^{155}Gd-100% [96 h]	2.6026	0.002118	8.63E-05	4.26905E-8	0.00224	0.0001	0.0
^{155}Gd-99% [96 h]	2.57866	0.02639	0.0014	1.928E-7	0.00222	0.0001	0.0
^{155}Gd-98% [96 h]	2.5547	0.05067	0.00276	3.4296E-7	0.002196	0.0001	0.0
^{155}Gd-91.90% [96 h]	2.40399	0.14878	0.00812	9.4601E-7	0.00526	0.0002	0.0004

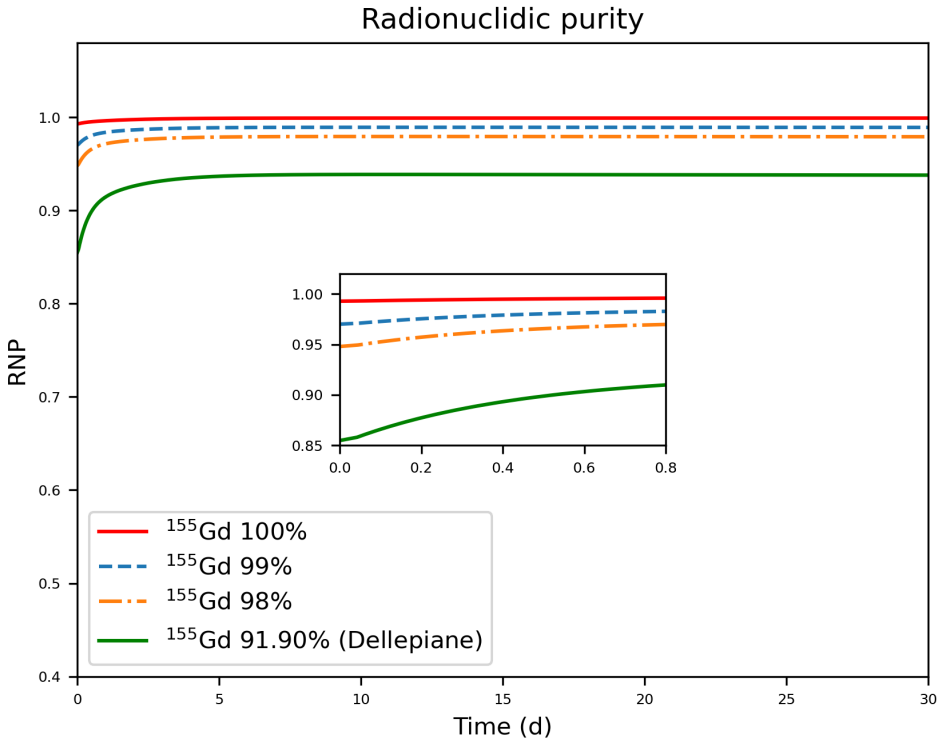

Figure 5.5 ^{155}Tb radionuclidic purity for the different target enrichments.

The time evolution of the ^{155}Tb RNP considering the four different target enrichment is shown in Fig. 5.5. For the target with the larger ^{156}Gd contamination (5.87%), RNP settles around 93.5% (solid green line), in agreement with the level measured after 96 h from EoB [131]. Significantly higher values are reached in the other three cases. In particular, 97.8, 98.8, and 99.8% RNP is obtained, after 96 h, with a target enrichment

of 98, 99, and 100%, respectively. This proves that the contamination of the target with ^{156}Gd directly affects the ^{155}Tb RNP, so it is crucial to limit it as much as possible. To complete the analysis the isotopic purity has been also evaluated. IP reaches values of 93.9, 97.9, 98.9, and 99.9% after 96 h from EoB and for an enrichment of 91.90, 98, 99, and 100% respectively. This implies that the production route is essentially carrier-free, without the presence of contaminants, including those stable or with long half-lives.

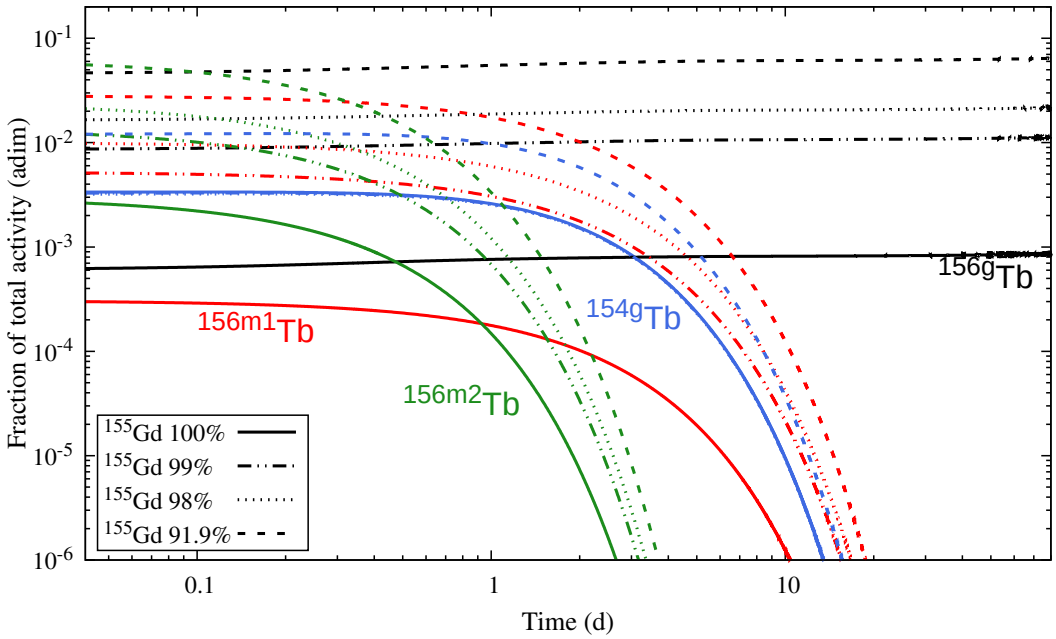

Figure 5.6 Fraction of total activity for the main contaminants ^{154g}Tb (blue curves), ^{156g}Tb (black curves), ^{156m1}Tb (red curves), ^{156m2}Tb (green curves), for different enrichment of the ^{155}Gd targets.

The fraction of total activity of ^{154g}Tb (blue curves), ^{156g}Tb (black curves), ^{156m1}Tb (red curves), ^{156m2}Tb (green curves) is shown in Fig. 5.6. It is evident that the main problem is the ^{156g}Tb due to its long half-life comparable to the ^{155}Tb one. Clearly, the amount of ^{156}Gd in the target proportionally influences the activity of all three states of ^{156}Tb. Conversely, the production of ^{154g}Tb represents a minor issue, thanks to its shorter half-life. It is noteworthy that in the selected energy region ^{154g}Tb is not produced by ^{156}Gd, therefore its percentage increase in the target does not affect the ^{154g}Tb production. As a matter of facts, increasing ^{156}Gd implies a reduction of the ^{155}Gd component thus causing a tiny decrease of ^{154g}Tb. However, ^{154g}Tb is produced mainly by ^{154}Gd, and this leads to an increase of the ^{154g}Tb activity with the less enriched target, comprising a 0.5% abundance of ^{154}Gd.

5.4 Dosimetric assessments

Biodistribution data of the DOTA-folate conjugate ^{161}Tb-cm09 in IGROV-1 tumour-bearing mice has been used for the dosimetric evaluation [60]. The cm09 is composed by a targeting vector (which selectively binds to the folate receptor expressed on a variety of tumour types) conjugated to small-molecular-weight albumin (which improves the blood circulation time and tissue distribution profile of folate conjugates) and to the DOTA chelating agent. Dosimetric calculation has been performed considering the cm09 labelled with the Tb-radioisotopes expected to be produced by proton irradiation of ^{155}Gd enriched targets. To estimate the absorbed doses to humans due to different Tb-radioisotopes biodistribution data of ^{161}Tb-cm09 acquired in a time window of 7 days post injection in IGROV-1 tumour-bearing female nude mice have been used. The differences in human and animal organ masses compared to the total body masses are assessed by means of the relative mass scaling method. The activity concentrations in the different animal source organs (blood, lung, spleen, kidneys, stomach, intestines, liver, salivary glands, muscle and bone), reported as per cent of injected activity per gram of tissue ($[\%IA/g]_A$), were scaled from mice to adult male humans to obtain the decay-corrected per cent of injected activity for each human source organ ($[\%IA/organ]_H$) for the ICRP 89 male phantom of 73 kg. The total volume of the blood (5110 ml) was obtained using the specific volume value of 70 ml/kg. Figure 5.7 shows the biodistribution data as a function of post injection (p.i.) time and fitted by a tri-exponential equation, representing the phase of accumulation and the possibility of both a fast and a slow elimination of the radiopharmaceutical, with CoKiMo software. A fast blood clearance followed by a quickly radiopharmaceutical uptake by the main organs, with a slow wash-out is observed. Liver and kidneys were the organs with slower clearance.

By assuming that the injected radiopharmaceutical was labelled each time with only one of the Tb-radioisotopes produced, the number of disintegrations in the source organs has been calculated. Results are summarized in table 5.3 for ^{153}Tb ^{154g}Tb, ^{155}Tb, ^{156}Tb, ^{156m1}Tb and ^{156m2}Tb. The two metastable states ^{154m1}Tb and ^{154m2}Tb are not included in the OLINDA software, thus they are not in the dosimetric analysis

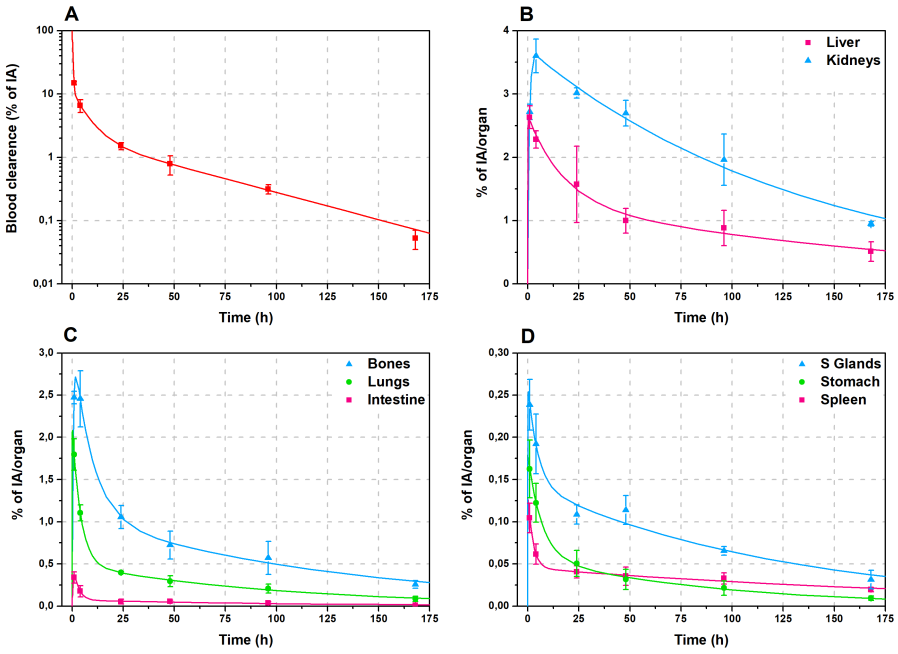

Figure 5.7 Experimental data from biodistribution studies and calculated time-activity curves of Tb-cm09 in the main source organs.

accordingly. Nevertheless, at the irradiation energy of 10.5 MeV the two metastable state of ^{154}Tb are produced only by ^{154}Gd, which is not an impurity of the targets with an enrichment $\geq 98\%$. Besides, since the energy of these two metastable states is very close to that of the ground state, their contribution to the absorbed dose occurs mainly through the decay of the ground state, properly taken into account through application of the Bateman equations.

For the dosimetric assessment, the total activity in the intestines was distributed in left colon, small intestine, right colon and rectum, according to their mass ratio with respect to the total intestine mass. The mean maximum volume of blood that could be contained in the four chambers of the heart, two atria and two ventricles, of an adult man is about 505 ml, therefore, just the 10% of the blood activity was assigned to the "heart contents" and the rest to "Remaining". The activity in the mice muscle was extrapolated to human considering that the human muscle is the 40% of the total body weight. Muscle activity was also assigned to the 'Remaining' organs when performing calculations with OLINDA 2.2.3, because this tissue is not included in the source organs

Table 5.3 Number of nuclear transitions (MBq × h/MBq) in source organs per unit administered activity of ^{xxx}Tb-cm09 labelled with ^{153}Tb, ^{154g}Tb, ^{155}Tb, ^{156}Tb, ^{156m1}Tb and ^{156m2}Tb, for male ICRP 89 human phantom.

Organ/Tissue	^{153}Tb-cm09	^{154g}Tb-cm09	^{155}Tb-cm09	^{156}Tb-cm09	^{156m1}Tb-cm09	^{156m2}Tb-cm09
Heart contents	0.148	0.118	0.168	0.168	0.122	0.075
Lung	0.288	0.177	0.391	0.392	0.190	0.079
Spleen	0.029	0.014	0.048	0.048	0.016	0.005
Kidneys	1.861	0.912	2.885	2.891	1.012	0.244
Stomach	0.033	0.020	0.043	0.044	0.022	0.008
Left colon	0.0052	0.0031	0.0072	0.0072	0.0033	0.0014
Small intestine	0.0240	0.0146	0.0335	0.0335	0.0156	0.0066
Right colon	0.0103	0.0062	0.0144	0.0144	0.0067	0.0028
Rectum	0.0052	0.0031	0.0072	0.0072	0.0033	0.0014
Liver	0.937	0.498	1.443	1.446	0.545	0.166
Cortical bone	0.698	0.405	0.991	0.993	0.438	0.152
Salivary glands	0.076	0.041	0.112	0.113	0.044	0.014
Remaining	7.494	3.985	8.819	8.833	4.274	1.719

of the ICRP 89 phantom model. For each ^{xxx}Tb-radiopharmaceutical, the organs with the highest number of disintegrations were the kidneys, followed by the liver and the cortical bone. Comparing the different radioisotopes, the ones with the highest number of disintegrations were ^{155}Tb and ^{156g}Tb, due to their long half-life. On the contrary ^{156m2}Tb showed the lowest number of disintegrations because of its relatively short half-life.

Thereafter these disintegrations data are used as the input values in the OLINDA software to perform dosimetric evaluations and calculate the organ absorbed doses per unit of administered activity and, in this case, for an adult male phantom. Results for the specific ^{xxx}Tb-cm09 are reported in Table 5.4.

For all the Tb-radioisotopes, the organs receiving the highest absorbed dose are the kidneys, followed by the osteogenic cells for ^{155}Tb, ^{156m1}Tb and ^{156m2}Tb, by the adrenals for ^{154}Tb and ^{156g}Tb. ^{156g}Tb is the radioisotope giving the highest values of absorbed doses, due to its long half-life and the large amount of energy emitted per decay (see Table 5.1). The absorbed doses due to ^{154}Tb administration are also higher than those of ^{155}Tb, because, even if the ^{154}Tb half-life is much shorter than that of ^{155}Tb, the energy emitted per decay is about ten times higher. The absorbed doses due to ^{156m1}Tb and ^{156m2}Tb are about one order of magnitude lower than those of ^{155}Tb (see Table 5.1). From the absorbed doses the effective doses has been derived. As reported in the last row

Table 5.4 Organ absorbed doses (mGy/MBq) and ED values (mSv/MBq) per unit administered activity calculated for ^{XXX}Tb-cm09 with the OLINDA 2.2.3 software for male ICRP 89 phantoms using the data reported in Table 5.3.

Target organ	^{153}Tb-cm09	^{154}Tb-cm09	^{155}Tb-cm09	^{156g}Tb-cm09	^{156m1}Tb-cm09	^{156m2}Tb-cm09
Adreanals	6.73E-02	1.68E-01	6.56E-02	4.69E-01	6.78E-03	1.44E-03
Brain	1.11E-02	2.61E-02	9.25E-03	5.68E-02	1.38E-03	1.22E-03
Esophagus	1.81E-02	4.93E-02	1.52E-02	1.10E-01	1.98E-03	1.24E-03
Eyes	1.10E-02	2.58E-02	9.09E-3	5.57E-02	1.36E-03	1.22E-03
Gallbladder wall	2.96E-02	7.75E-02	2.66E-02	1.97E-01	3.05E-03	1.27E-03
Left colon	2.34E-02	5.91E-02	2.04E-02	1.44E-01	2.50E-03	1.71E-03
Small intestine	2.00E-02	5.10E-02	1.67E-02	1.19E-01	2.11E-03	1.71E-03
Stomach wall	2.17E-02	5.60E-02	1.87E-02	1.29E-01	2.49E-03	2.05E-03
Right colon	2.18E-02	5.59E-02	1.87E-02	1.34E-01	2.31E-03	1.71E-03
Rectum	1.64E-02	4.13E-02	1.33E-02	9.11E-02	1.80E-03	1.70E-03
Heart wall	2.53E-02	6.75E-02	2.14E-02	1.35E-01	3.64E-03	4.98E-03
Kidneys	2.85E-01	3.92E-01	3.48E-01	1.29E00	4.27E-02	3.99E-02
Liver	4.73E-02	1.01E-01	5.06E-02	2.77E-01	6.10E-03	4.74E-03
Lungs	2.10E-02	4.78E-02	1.99E-02	1.10E-01	3.00E-03	3.36E-03
Pancreas	2.31E-02	6.14E-02	1.97E-02	1.46E-01	2.37E-03	1.22E-03
Prostate	1.58E-02	4.15E-02	1.23E-02	9.27E-02	1.55E-03	1.22E-03
Salivary Glands	4.16E-02	6.42E-02	4.67E-02	1.74E-01	6.57E-03	8.32E-03
Red Marrow	1.49E-02	4.11E-02	1.15E-02	9.39E-02	1.41E-03	1.03E-03
Osteogenic cells	7.45E-02	6.00E-02	8.61E-02	1.75E-01	1.78E-02	1.04E-02
Spleen	3.26E-02	7.72E-02	3.27E-02	2.12E-01	3.53E-03	1.75E-03
Testes	1.12E-02	2.92E-02	8.58E-03	6.09E-02	1.20E-03	1.21E-03
Thymus	1.55E-02	4.31E-02	1.22E-02	8.86E-02	1.75E-03	1.24E-03
Thyroid	1.37E-02	3.55E-02	1.10E-02	7.60E-02	1.54E-03	1.22E-03
Urinary bladder wall	1.46E-02	3.82E-02	1.12E-02	8.24E-02	1.48E-03	1.22E-03
Total body	1.54E-02	3.57E-02	1.36E-02	8.13E-02	1.91E-03	1.74E-03
Effective dose	1.96E-02	4.44E-02	1.86E-02	1.09E-01	2.47E-03	2.06E-03

of Tab 5.4, the ED after administration of ^{156m1}Tb-cm09 and ^{156m2}Tb-cm09 are lower than the one of ^{155}Tb-cm09. This suggests that the contamination of the production by these two metastables will not increase the dose to the patient. In contrast, labelling the radiopharmaceutical with ^{156g}Tb or ^{154}Tb entails an ED 5.9 and 2.4 times greater than the ED obtained with ^{155}Tb-cm09. Hence, to maintain the increment of the dose per unit of activity administered below the limit 10%, the presence of ^{156g}Tb or ^{154}Tb as contaminants must be lower than about 2% or 7% respectively.

5.5 Dose increase

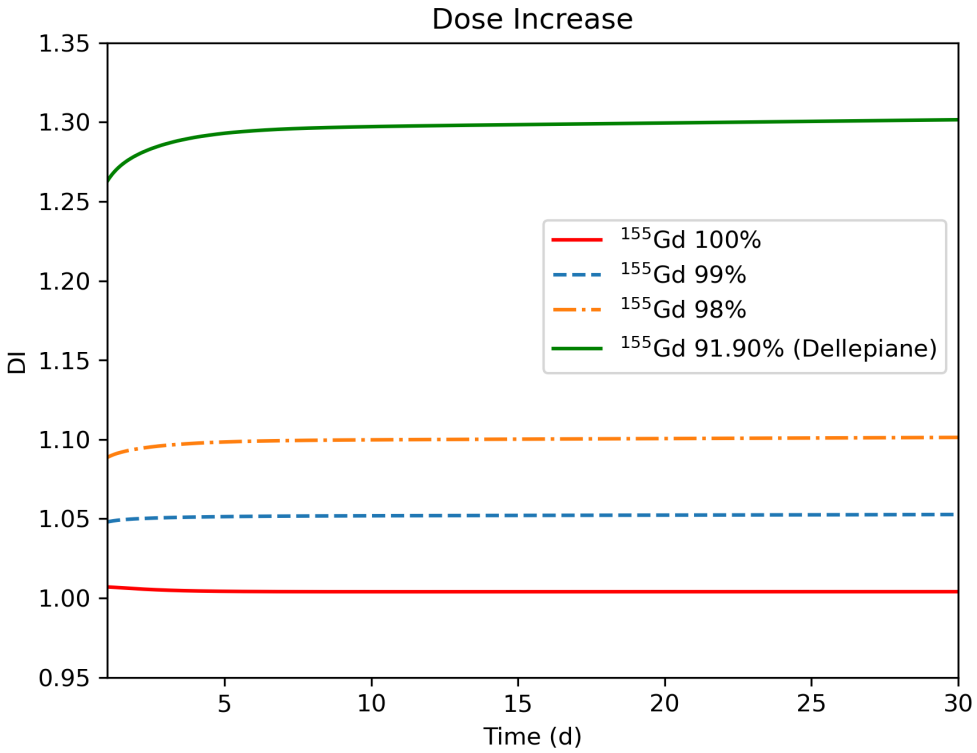

Figure 5.8 Dose increase for ^{155}Tb-cm09 radiopharmaceutical labeled at different times after the end of irradiation of different ^{155}Gd-enriched targets.

The dosimetric analysis gives an information of the effective dose calculated per unit of activity of a specific ^{xxx}Tb-cm09 administered. Once these values are obtained, it is necessary to match and complete the analysis including an actual amount of activity that is produced during an irradiation experiment. In this work, in terms of enrichment of the target, four are the case of studies, as exhaustively discussed in this chapter. As is known a certain nuclear reaction, under precise irradiation conditions, gives rise to

a specific production. A small variation in the target composition causes a change in the resulting activity, namely the potential production of contaminants that could affect the final purity. It follows that this may have an effect on the DI due to the presence of impurities in the production, and this is a crucial point if medical applications are the goal to be achieved. To meet the medical demand and to comply with the safe limits is mandatory.

Fig. 5.8 compares the DI due to ^{155}Tb-cm09 obtained with different levels of target enrichment. For the 91.9% target enrichment the DI is well above 25% and this confirms that the isotopic contamination of that target is inadequate for medical purposes. The ideal case of a ^{155}Gd target with 100% enrichment, described by the solid red line, corresponds to a negligible increase of the dose. Referring to the RNP, this is the case for which the purity is very close to 100%. Quite interesting are the dashed and dot-dashed curves obtained with 99% and 98% enrichment. The former reaches a 5% DI, while the latter remains within the 10% limit. Considering the last three cases (100, 99, and 98%) and focusing on the very start of the plot, at short time t post-production, it is evident the difference in the trend of the curves. For the ideal target the initial decrease of the DI before it stabilizes depends on the decay of the short-lived radionuclides produced during the irradiation. Whereas, the other two cases show an opposite behaviour, the DI starts rising and then it stabilizes. This effect depends on the increase of the ^{156g}Tb production from the ^{156}Gd component of the target. Specifically, the enhanced population of the ground state is due to the decay of the two metastables ^{156m1,m2}Tb. Since the half life of ^{156g}Tb is comparable to the ^{155}Tb one, thus it does not decay quickly, and since the emitted energy by ^{156g}Tb is 10 times higher than the ^{155}Tb one (see Tab 5.1 for details) its presence results into a higher DI.

5.6 Analysis of the imaging properties of ^{155}Tb in the presence of other contaminant isotopes

The quality of SPECT images is crucial for obtaining a precise medical diagnosis. For this reason the noise produced by the Compton scattering of high energy gamma rays may be a big issue. For the nuclear reaction ^{155}Gd(p,x)^{155}Tb the imaging properties of

^{155}Tb in the presence of other γ-emitting contaminant isotopes have been investigated. Indeed, using an energy window to acquire only the gamma rays of interest might not be enough to bypass the problem, because higher energy γ-rays can be Compton scattered and registered by the acquisition system. The effect of such signals results in blurry and bad contrast images. Therefore, a study of the noise contribution of high-energy γ-rays emitted by Tb-contaminants has been carried out using a preclinical PET/SPECT/CT system (VECTor 5, Milabs) as a model of the acquisition system. To simulate the γ-ray spectrum of each Tb radionuclide in VECTor 5, a homemade menu-driven spreadsheet software Visual Gamma has been used. It deploys specific initial system parameters, such as efficiency and peak shape and simulates the spectrum of the radionuclides, considering as input data the energy and the intensity of the γ-ray from the NUDAT3 database [1]. Parameters such as γ-ray efficiency, the peak width, and the shape of the Compton area as a function of the γ-rays energies have been determined using standard calibration point-like sources in air, i.e. ^{57}Co, ^{22}Na, ^{60}Co and ^{137}Cs . To evaluate the image quality, assessed by using a particular γ-ray peak, two main factors are considered: the intensity of the γ-ray emission and the presence of Compton scattered γ-rays in the energy window in correspondence of the selected peak for imaging. An energy window of 10% interval around the peak barycenter has been chosen. To estimate the influence of Compton scattered γ-rays on the final quality of the image, the ratio $\delta = \frac{N_{extr}}{N_{intr}}$ has been employed, where N_{extr} is the number of all higher-energy γ-rays that underwent Compton scattering and fell into the selected energy window, N_{intr} is the number of γ-rays from the selected photo-peak that fell into the energy window, i.e. not including Compton scattering contribution. It is convenient to use such Compton-to-peak ratio since in the ideal case (lack of other noises) its value directly corresponds to the amount of the noises in the image. Since for the ^{155}Tb production from the proton irradiation of ^{155}Gd targets a comparison among different levels of target enrichment has been investigated, the same analysis has been carried out for the evaluation of the imaging quality. Specifically, the 100, 99 and 98% enrichment have been considered and the calculations refer to both the EoB and 96 h later.

5.6.1 Impact on the image quality

The imaging quality of ^{155}Tb produced with the different enriched ^{155}Gd targets was assessed at the EoB and 96 h later by considering the ^{156g}Tb and ^{154g}Tb yields reported in Table 2. The metastable states ^{156m1}Tb, ^{156m2}Tb and ^{154m1}Tb were disregarded in the simulations because of their lower energy gamma ray emission. A typical γ-ray spectrum is shown in Fig. 5.9. It has been simulated for ^{155}Tb produced at the EoB from the irradiation of 100% enriched ^{155}Gd target. The gamma rays with the energies of 86.55 keV and 105.318 keV emitted from ^{155}Tb and the low intensity 88.97 keV gamma ray emitted by ^{155g}Tb are situated close with respect to the energy resolution of the imaging system and form a compound peak with a barycenter of 88.5 keV. Other four peaks from ^{155}Tb with energies of 148.64 keV, 161.29 keV, 163.28 keV and 180.08 keV form a less intense compound peak with a barycenter of 167 keV. A smaller ^{155}Tb peak at 262 keV (5.3%) is exposed to the higher energy gamma rays from the isotopes of ^{154g}Tb and ^{156g}Tb only. For imaging purposes, the compound peak with the energy of 88.5 keV is most convenient, for its higher intensity, though the other two peaks at 167 keV and 262 keV can also be used for imaging. Table 5 shows the calculated Compton-to-peak ratio for the three principal peaks of ^{155}Tb with respect to the gamma-ray background, generated by the contaminant isotopes ^{156g}Tb and ^{154g}Tb. The analysis of the data reveals that in all cases the level of noises in the gamma ray images reconstructed using a 10% energy window around the barycenter of the peaks does not exceed 27%. For the intense peak at 88.5 keV the Compton-to-peak ratio remains within the interval of 19%– 23% for all kind of targets immediately after the EoB and no significant improvement could be achieved 96 h later. Somewhat lower Compton-to-peak values below 20% are obtained for the compound peak at 167 keV. This suggests its use as a single peak for image reconstruction in some particular cases. The lower intensity of the peak at 262 keV makes the ratio more affected by the presence of the contaminant nuclides ^{156g}Tb and ^{154g}Tb though its maximum value still remains below 27%. However, it is worth noting that the present image quality estimation is made for point-like gamma-ray sources in air, hence the values quoted refer to the imaging system only and do not take into account Compton scattering inside the tissues. To estimate this contribution for the case of small animals imaging, a water phantom

Table 5.5 Compton-to-peak ratio calculated from the simulation of ^{155}Tb gamma-ray spectra, obtained for 100%, 99% and 98% enrichment of ^{155}Gd targets, at the EoB and 96 h later.

	Compton-to-peak ratio at the EoB			Compton-to-peak ratio 96 h after EoB		
Peak energy (keV)	100% ^{155}Gd	99% ^{155}Gd	98% ^{155}Gd	100% ^{155}Gd	99% ^{155}Gd	98% ^{155}Gd
88.5	19.44%	20.99%	22.59%	18.89%	21.52%	22.61%
167	10.24%	14.54%	19.06%	8.91%	15.95%	19.32%
262	5.84%	16.12%	26.9%	1.71%	19.8%	26.55%

was used in our laboratory, obtaining a noise increase level smaller than 5%.

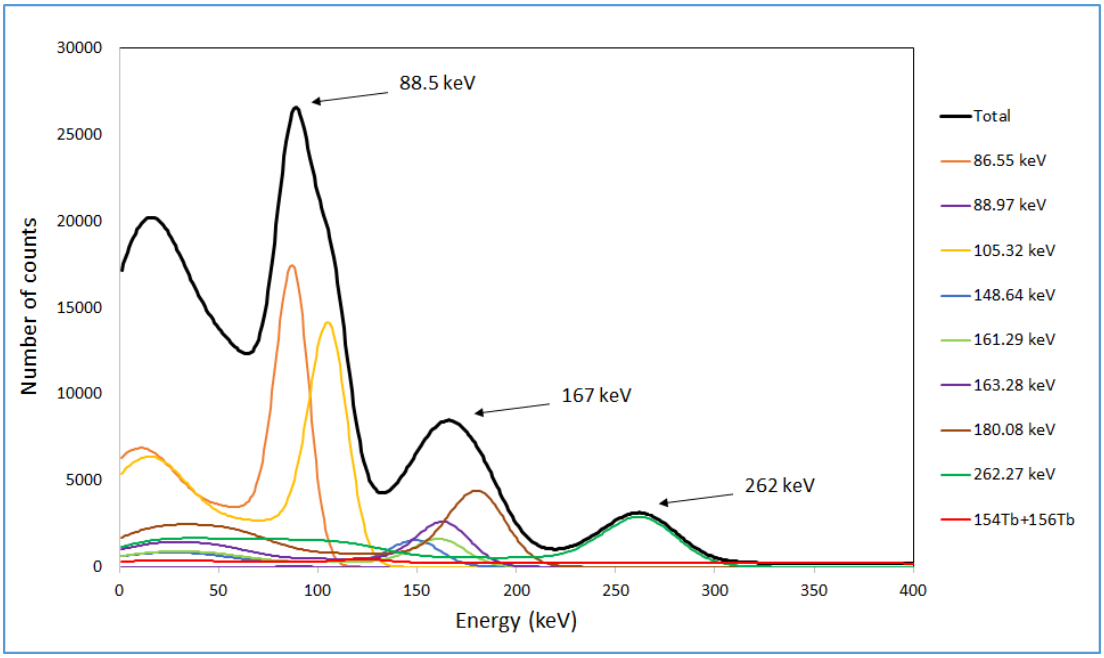

Figure 5.9 Simulated spectrum for ^{155}Tb, obtained immediately after the proton bombardment of 100% enriched ^{155}Gd target. The predicted observable spectrum is presented with a thicker black line.

5.6.2 Comparison between ^{155}Tb and ^{111}In: applications

The targeted theranostic agents currently used in nuclear medicine are based on biological structures such as peptides, monoclonal antibodies and their fragments, coupled to α and β emitters radionuclides. However, due to their nature, these agents exhibit maximum absorption time range from several hours to a few days after injection. ^{111}In is the only radionuclide currently used in the clinic to perform SPECT imaging of these radiocomplexes since its half-life (2.8 d) is long enough for image acquisition even several days after the radiocomplex administration. Therefore, to evaluate the ^{155}Tb potential as matched pair for targeted theranostic agents labelled with ^{149}Tb and ^{161}Tb, it is interesting to compare its imaging and dosimetric

properties with those of ^{111}In. Imaging simulations for pure ^{111}In have been performed considering the main photon emissions at energies of 171 keV (91%) and 245 KeV (94%) to compare its Compton-to-peak ratio with those of ^{155}Tb. The Compton-to-peak ratio of the peak at 171 keV, the closest in energy to the 88.5 keV and 167 keV peaks of ^{155}Tb, turned out to be 22.6%, which is slightly larger than the values obtained for ^{155}Tb, although they are comparable. These results are supported by the excellent imaging properties of ^{155}Tb reported by Favaretto [130], where a spatial resolution up to 1 mm was obtained from a Derenzo phantom. Moreover, Muller et al. [124] published a comparison between SPECT images of Derenzo phantoms filled with solutions of pure ^{155}Tb (2.6 MBq) and ^{111}In (4 MBq), demonstrating comparable spatial resolution and the ability to produce equal images with lower activity of ^{155}Tb. Dosimetric properties of ^{111}In-labelled cm09 were estimated with OLINDA by assuming the same biodistribution of Tb-cm09 compound. The calculated ED of ^{111}In-cm09 was 0.0217 mSv/MBq, very similar to that of ^{155}Tb-cm09 (0.0186 mSv/MBq). These results are a consequence of the fact that ^{155}Tb total energy emission per decay is about 2 times lower compared to ^{111}In (0.4409 MeV/nt), despite its the half-life of is almost 2 times longer than that of ^{111}In. It should therefore be expected the imaging and dosimetric properties of ^{155}Tb-radiocomplexes to be comparable and even better of those of ^{111}In ones.

5.7 Discussion

^{155}Tb is a promising radionuclide for medical applications and its production by using low-energy proton beams on ^{155}Gd-enriched target represents a valid possibility. However, the isotopic composition of the target strongly influences the amount of co-produced radioisotopes. Indeed, depending on the impurities of the target, harmful radioisotopes could contaminate the production, endangering the purity of the route. The contaminant ^{156g}Tb, due to its half-life comparable to that of ^{155}Tb and its γ emissions that could have a severe impact on the dose released and on the quality of the SPECT images, is the most troublesome. That is why its production should be kept as low as possible. One solution to minimize the co-production of ^{156g}Tb is to limit the ^{156}Gd content in the target. The analysis of the RNP suggests to limit the

^{156}Gd component to a maximum of 1%. Precisely, for a 99% ^{155}Gd enriched target, a RNP higher than 98.5% is reached from about 30 h after the EoB and then it slowly approached a maximum value of 99%. Recalling the 10% limit in DI due to the contaminants, the evaluation of the only RNP might be too restrictive or too permissive. The reaction ^{155}Gd(p,n)^{155}Tb falls within the first case. Indeed, to guarantee a DI within the 10% limit the maximum content of ^{156}Gd in the target could be increased to 2%, even though the RNP at this enrichment level is slightly below the 99%. It is worth to note that in this case the DI does not exceed the 10% value in the entire time range shown in Fig. 5.8, namely from 0 to 30 days. Therefore the available activity can be utilized much earlier with respect to the timing when the RNP is close to 98%, and specifically, the product can be available right after the time needed to perform a radiochemical purification [130].

Moreover, it is important to address the target issue from the market point of view. Enriched ^{155}Gd is currently commercially available from various companies (ISOFLEX, CIL, AMT, etc) with ^{155}Gd purity greater than 90%, but with a ^{156}Gd component larger than 2%, not yet sufficient for the production of ^{155}Tb with the necessary purity for medical application. Gd-isotopes separation is performed commercially using the "Calutron method", namely using a very large mass spectrometer for electro-magnetic separation. Since this technique is very energy inefficient, the prices for the enriched Gd material are high. However, it is possible to tune the Calutron to produce high enriched ^{155}Gd with isotopic enrichment >98.0%, or with 156Gd content <2%. To make a producer interested in changing the operational plan implies an economical return and profitability which presently is not yet expected by the isotope-producer companies (Allan Pashkovski, Managing Director, Isoflex, Private communications, 6th July, 2023). A scenario of a diffuse worldwide production of ^{155}Tb by hospital cyclotrons may be much more favorable for the expectations of economical return by the producer companies.

5.8 Conclusion

To conclude, ^{155}Tb is a real candidate for SPECT diagnosis, thanks to its physical features and the favourable dosimetric and imaging outcomes, largely discussed in this chapter. To summarise, a high-quality production is possible by using low-energy proton beams, suitable for hospital cyclotron, and ^{155}Gd-enriched targets, beware of a maximum of 2% of ^{156}Gd impurity. Under these conditions the DI, due to the presence of contaminant radioisotopes, remains below the 10% limit. In addition, from the analysis of the imaging properties and the comparison with ^{111}In currently used in clinics, good quality images are guaranteed.

Chapter 6

Conclusions

This research on the cyclotron production of the innovative radionuclides is placed inside a multidisciplinary context where theoretical and experimental nuclear physics, dosimetry, radiochemistry, radiopharmacy and diagnostic imaging are strongly interconnected. Scandium and Terbium are both very promising for precision medicine and the scientific community currently debates about feasible production routes that guarantee the fulfillment of the clinical standards.

The potential of ^{47}Sc ($T_{1/2}$ = 3.35 d) stems from its favorable β^- decay properties accompanied by the emission of γ-rays of an ideal energy for SPECT imaging. Moreover, it may be easily combined with positron emitters ^{43}Sc ($T_{1/2}$ = 3.9 h) and ^{44}Sc ($T_{1/2}$= 4.0 h) for production of PET/β^- theranostic radiopharmaceuticals.

^{155}Tb ($T_{1/2}$ = 5.32 d) is an emerging radionuclide of considerable interest for metabolic radiotherapy. As γ-emitter, it is suitable for SPECT imaging and it might be a possible radionuclide also for targeted therapy due to its emission of both Auger and conversion electrons. The possibility to pair ^{155}Tb with other Terbium-isotopes makes it more attractive and flexible in nuclear medicine applications. Currently, ^{155}Tb is new entry in the international market and its production via ^{155}Gd(p,n)^{155}Tb is at its infancy. Therefore, theoretical calculations of the production cross section are essential to guide the experiments.

The advantage of a single element radiopharmaceutical is the chemically identical composition of the drug used for both imaging and therapy. This means same biodistribution of the radiopharmaceutical for both medical investigations, ensuring the treatment effectiveness based on a precise diagnostic information. Theranostics allows personalized treatments on the concept “what we see is what we treat (almost)”. Patients with similar disease could respond to a radiopharmaceutical differently. The use of a small amount of radiopharmaceutical for an imaging scan

makes it possible to measure the uptake of the compound and so to determine in advance the effectiveness of the therapy for the specific patient. Therefore, imaging techniques plays a leading role in relevant clinical applications, since for a precise delivery of therapy high-quality images are essential. A more detailed information gained through the acquisition of more images leads to a better planning of the medical treatments. MultiModal Imaging is a branch of nuclear medicine that combines morphological and functional images acquired from different modalities for a more detailed image. In this context Manganese is an element of interest. It benefits from its paramagnetic property that suits magnetic resonance imaging (MRI) of neuronal function. However, high concentrations of Mn^{2+} can be neurotoxic. ^{52g}Mn may be a valid alternative as a PET (positron emission tomography) imaging agent, to obtain information similar to that delivered by MRI but using trace levels of Mn^{2+}, thus reducing its toxicity. Its decay properties (β^+) and quite long half-life ($T_{1/2}$ = 5.6 day) make this radionuclide very promising as PET tracer, with an image resolution similar to that of ^{18}F. The standard cyclotron-based production of ^{52g}Mn relies on the nuclear reaction ^{nat}Cr(p,x) ^{52g}Mn. In this research the comparison with the alternative reaction ^{nat}V(α,x)^{52g}Mn has been proposed.

The production of ^{47}Sc has been investigated considering three cyclotron routes with enriched ^{49}Ti and ^{50}Ti targets. For the reaction with protons on enriched ^{49}Ti targets the theoretical cross sections of both ^{47}Sc and its main contaminants have been compared with the very first production measurements within the REMIX project. The preliminary data suggest an overestimation of the theoretical ^{47}Sc cross section. For a better description of the cross sections the nuclear level density has been investigated for a set of compound nuclei. To optimize the input parameters of the nuclear reaction code I set up a two-step procedure. First a grid analysis to roughly identify the best choice for the initial set of level density parameters and, secondly, a powerful optimization scheme based on genetic algorithms (GA). GA define a metaheuristic optimization strategy inspired by Darwin's theory of natural selection. The algorithm adopts biological-inspired operators based on the mechanisms of natural evolution where the fittest individuals of a population survive to produce offsprings for the next generation. From the optimized cross sections the activity for

each radionuclide, the integral yields, and the radionuclidic purity (RNP) are derived to verify the feasibility of the production route. However, for the reaction with protons on ^{49}Ti targets, RNP reaches a maximum value of about 75% due to the large contribution of the two contaminants. This reveals that the production route ^{49}Ti(p,2pn)^{47}Sc is not adequate for clinical investigations. This unfavorable outcome drove the research to another nuclear reaction: ^{49}Ti(d,α)^{47}Sc. The analysis suggests this route as a valid alternative to the one with a proton beam. The small contamination by ^{46}Sc and ^{48}Sc to the ^{47}Sc production around 10 MeV makes the d-^{49}Ti channel a promising reaction, possibly also for a ^{47}Sc production by low-energy (hospital) cyclotrons. Similar outcomes are obtained for the reaction with protons on enriched ^{50}Ti targets. In this case the new preliminary REMIX data, together with the newest data available in literature, have validated the models and have allowed the slight improvement of the cross sections. The results indicate this reaction suitable for applications since the medical requirements of purity are satisfied. Another interesting and convenient method to produce high-quality ^{47}Sc concerns the use of protons from intermediate-energy cyclotrons (like SPES cyclotron at the INFN-Legnaro Laboratories) on a bilayer made of ^{nat}V and ^{50}Ti. The innovation lies in exploiting for each layer the favorable energy ranges in which the co-production of contaminants is limited. Specifically, when the energy is too high and the production with ^{50}Ti is no more adequate due to the co-produced contaminants, the reaction with ^{nat}V starts to be suitable for a high-quality ^{47}Sc production. In this way the purity required for clinics is guaranteed and the production is enhanced, when compared to a mono-element target production. This study has led to an industrial invention, Patent application No. 102023000018477 by the INFN Office of Technological Transfer, of which I am one of the inventors.

Regarding Manganese, a comparison between the two production routes, p-^{nat}Cr and α-^{nat}V, has been carried out. Once the RNP has been assessed, the dose increase (DI) due to the co-produced radioactive contaminants versus pure $^{52g}MnCl_2$ administration has been evaluated. To improve the comparison, an optimized calculation within the TALYS code has been developed, where the parameters of the nuclear level densities in the microscopic Hartree-Fock formalism have been adjusted to the measured cross

sections. Thick-target yields have been calculated from the expression of the rates as energy convolution of cross sections and stopping powers, and finally integrating over the time evolution of the relevant decay chains. Dosimetric evaluations have been accomplished by means of the OLINDA software in both adult female and male phantoms. Finally, by means of a PYTHON code I developed, the DI has been calculated by combining the yield of ^{xx}Mn radioisotopes estimated for both reactions with the dosimetric outcomes given for the injected activity of 1 MBq. The computational dosimetric analysis shows that both ^{nat}V(α,x) and ^{nat}Cr(p,x) production routes provide clinically acceptable ^{52g}MnCl 2 for PET imaging. However, with the ^{nat}V(α,x)^{52g}Mn reaction the DI is systematically lower than the one obtainable with ^{nat}Cr(p,x)^{52g}Mn and the time window in which it can be used clinically (RNP greater than 99%) is longer.

Lastly, the production of ^{155}Tb has been investigated. All steps from the evaluations of the cross sections to the dosimetric calculations have been carried out. The interest of ^{155}Tb for clinics and the lack of its availability in the market with adequate purity for medical applications, put the attention on the level of enrichment of the targets. Results show a small co-production of contaminants in the energy range favorable for the ^{155}Tb production, making this reaction a promising low energy production route, suitable for hospital cyclotrons. However, when enriched ^{155}Gd targets are not ideally enriched (100%), the presence of impurities, particularly of ^{156}Gd, may contribute to a rise of the contamination. The study aimed at identifying the right isotopic composition of the target and so the minimum level of target enrichment for lowering the contamination and ensuring sufficient purity for clinics. Findings suggest that with an enrichment of 98% the medical requirements are met. Previous studies have drawn not favorable conclusions according to which the inevitable contamination by ^{156}Tb could be decreased only by a subsequent use of a mass separator. This change of perspective, namely, to avoid high contamination thanks to an appropriate enrichment of the target, might have a tangible effect on the market production methods.

REFERENCES

[1] NuDat 3, "NuDat 3 - National Nuclear Data." [Online]. Available: https://www.nndc.bnl.gov/nudat3/

[2] ICRP 107, "Nuclear Decay Data for Dosimetric Calculations. ICRP Publication 107. Ann. ICRP 38 (3)." 2008. [Online]. Available: https://www.icrp.org/publication.asp?id=ICRP%20Publication%20107

[3] Collins S. M., Robinson A. P., Ivanov P. *et al.*, "Half-life determination of 155Tb from mass-separated samples produced at CERN-MEDICIS." *Applied Radiation and Isotopes*, vol. 190, p. 110480, 2022.

[4] "PRISMAP," 2021, retrieved Jan 6, 2024. [Online]. Available: https://www.prismap.eu/

[5] Canton L. and Fontana A., "Nuclear physics applied to the production of innovative radiopharmaceuticals." *Eur. Phys. J. Plus*, vol. 135, p. 770, 2020.

[6] Alanazi N. L., "Studying the Fusion Evaporation Reaction (α,n) with ^{54}Fe, ^{56}Fe, ^{57}Fe, and ^{58}Fe." *PhD thesis*, 2018.

[7] Chen K. L. and M M., "Comparison Between Reactions of Alpha Particles With Scandium-45 and Deuterons with Titanium-47." *Phys. Rev.*, vol. 134, p. B1269, 1964.

[8] Sudhakar A., "History of Cancer, Ancient and Modern Treatment Methods," *Journal of Cancer Science Therapy*, vol. 1, pp. i–iv, 2009.

[9] Peltek O. O., Muslimov A. R., Zyuzin V. M., and Timin A. S., "Current outlook on radionuclide delivery systems: from design consideration to translation into clinics." *J Nanobiotechnol*, vol. 17, p. 90, 2019.

[10] www.iaea.org/publications, *Guidance for Preclinical Studies with Radiopharmaceuticals IAEA RADIOISOTOPES AND RADIOPHARMACEUTICALS SERIES No. 8.* IAEA RADIOISOTOPES AND RADIOPHARMACEUTICALS SERIES No. 8, 2023.

[11] Sadler, A W E, H. L. F. B. *et al.*, "Cutting edge rare earth radiometals: prospects for cancer theranostics." *EJNMMI radiopharm. chem.*, vol. 7, p. 21, 2022.

[12] Naskar N. and Lahiri S., "Theranostic Terbium Radioisotopes: Challenges in Production for Clinical Application." *Front. Med. Imaging*, vol. 8, p. 675014, 2021.

[13] Lewis J. S., Windhorst A. D., and Zeglis B. M., *Radiopharmaceutical Chemistry.* Springer Nature Switzerland AG, 2019.

[14] Türler A., "Matched pair theranostics." *Chimia*, vol. 73, p. 947–9, 2019.

[15] Jalilian A. R., Gizawy M. A., Alliot C. *et al.*, "IAEA Activities on ^{67}Cu, ^{186}Re, ^{47}Sc Theranostic Radionuclides and Radiopharmaceuticals." vol. 14, pp. 306–314, 2020.

[16] Müller C., Domnanich K., Umbricht C., and van der Meulen N., "Scandium and terbium radionuclides for radiotheranostics: current state of development towards clinical application." *Br J Radiol*, vol. 91, p. 20180074, 2018.

[17] Duchemin C., "CERN-MEDICIS: A Review Since Commissioning in 2017." *Front. Med.*, vol. 8, 2021.

[18] Esposito J., Bettoni D., Boschi A. *et al.*, "LARAMED: A Laboratory for Radioisotopes of Medical Interest," *Molecules*, vol. 24, no. 1, 2019.

[19] Pupillo G. *et al.*, "Research on Emerging Medical radIonuclides from the X-sections (REMIX): The Accelerator-based Production of ^{47}Sc, ^{149}Tb, ^{152}Tb, ^{155}Tb and ^{161}Tb," *Phys. Conf. Ser.*, vol. 2586, p. 012118, 2023.

[20] Martí-Bonmatí L., Sopena R., Bartumeus P., and Sopena P., "Multimodality imaging techniques." *Contrast Media Mol Imaging*, vol. 5, pp. 180–9, 2010.

[21] Brandt M. *et al.*, "Manganese in PET Imaging: Opportunities and Challenges." *J. Label Compd. Radiopharm.*, vol. 62, p. 541, 2019.

[22] Colombi A., Carante M., Barbaro F., Canton L., and Fontana A., "Production of High-Purity ^{52g}Mn from ^{nat}V Targets with α Beams at Cyclotrons." *Nucl. Technol.*, vol. 208, pp. 735–752, 2022.

[23] Leo W. R., *Techniques for Nuclear and Particle Physics Experiments. A How-to Approach*. Springer-Verlag, 1987.

[24] Koning A., Hilaire S., and Goriely S., *TALYS-1.96/2.0 - Simulation of nuclear reactions*, 2021.

[25] Koning A. J., Hilaire S., and Goriely S., "TALYS: modeling of nuclear reactions." *Eur. Phys. J. A*, vol. 59, 2023.

[26] Glendenning N. K., *Direct Nuclear Reactions*. Academic Press, Inc. (Elsevier), 1983.

[27] Mumpower M. R., Neudecker D., Sasaki H., Kawano T., Lovell A. E., Herman M. W., Stetcu I., and Dupuis M., "Collective enhancement in the exciton model." *Phys. Rev. C*, vol. 107, p. 034606, 2023.

[28] Gadioli E. and Hodgson P. E., *Pre-equilibrium Nuclear Reactions*. Oxford University Press, New York, 1992.

[29] Cline C. and Blann M., "The pre-equilibrium statistical model: description of the nuclear equilibration process and parameterization of the model." *Nucl Phys A.*, vol. 172, pp. 225–259, 1971.

[30] Bertulani C. A., "Nuclear Reactions," 2010, arXiv:0908.3275 [nucl-th].

[31] Hauser W. and Feshbach H., "The inelastic scattering of neutrons." *Phys. Rev.*, vol. 87, p. 366, 1952.

[32] Goriely S., Hilaire S., and Koning A. J., "Improved predictions of nuclear reaction rates with the TALYS reaction code for astrophysical applications." *Astron. Astrophys.*, vol. 487, p. 767, 2008.

[33] Hilaire S., Koning A. J., and Goriely S., "Microscopic cross sections: An utopia?." *EPJ Web Conf.*, vol. 8, p. 02004, 2010.

[34] Feshbach H., Kerman A., and Koonin S., "The statistical theory of multi-step compound and direct reactions." *Ann Phys.*, vol. 125, pp. 429–476, 1980.

[35] Blann M., “Importance of the Nuclear Density Distribution on Pre-Equilibrium Decay.” *Phys. Rev. Lett.*, vol. 28, p. 757, 1972.

[36] Blann M. and Vonach H. K., “Global test of modified precompound decay models.” *Phys. Rev. C*, vol. 28, p. 1475, 1983.

[37] Konobeyev A. Y., Fischer U., Pereslavtsev P. E., Koning A., and Blann H., *Implementation of GDH model in TALYS-1.7 code*, 2016.

[38] Koning A. J. and Rochman D., “Modern Nuclear Data Evaluation with the TALYS Code System.” *Nucl. Data Sheets*, vol. 113, pp. 2841–2934, 2012.

[39] Gilbert A. and Cameron A. G. W., “A composite nuclear-level density formula with shell corrections.” *Can. J. Phys.*, vol. 43, pp. 1446–1496, 1965.

[40] Ericson T., “The statistical model and nuclear level densities.” *Advances in Physics*, vol. 9, no. 36, pp. 425–511, 1960.

[41] Ignatyuk A. V., Smirenkin G. N., and Tishin A. S., “Phenomenological description of energy dependence of the level density parameter.” *Sov. J. Nucl. Phys.*, vol. 21, no. 3, p. 255, 1975.

[42] Koning A., Hilaire S., and Goriely S., *TALYS-1.95 - A nuclear reaction program, user manual*, 2019.

[43] Ignatyuk A. V., Weil J. L., Raman S., and Kahane S., “Density of discrete levels in ^{116}Sn.” *Phys. Rev. C*, vol. 47, pp. 1504–1513, 1993.

[44] Dilg W., Schantl W., Vonach H., and Uhl M., “Level density parameters for the Back-Shifted Fermi gas model in the mass range 40 < A < 250.” *Nucl. Phys. A*, vol. 217, no. 2, pp. 269–298, 1973.

[45] Demetriou P. and Goriely S., “Microscopic nuclear level densities for practical applications.” *Nucl. Phys. A*, vol. 695, p. 95, 2001.

[46] Minato F., “Nuclear level densities with microscopic statistical method using a consistent residual interaction.” *J. Nucl. Sci. Technol.*, vol. 48, p. 984, 2011.

[47] Hilaire S. and Goriely S., "Global microscopic nuclear level densities within the HFB plus combinatorial method for practical applications." *Nucl. Phys. A*, vol. 779, pp. 63–81, 2006.

[48] Goriely S., Hilaire S., and Koning A. J., "Improved microscopic nuclear level densities within the Hartree-Fock-Bogoliubov plus combinatorial method." *Phys. Rev. C*, vol. 78, p. 064307, 2008.

[49] Hillman M. and Grover J. R., "Shell-Model Combinatorial Calculations of Nuclear Level Densities." *Phys. Rev.*, vol. 185, pp. 1303–1319, 1969.

[50] Hilaire S., Girod M., Goriely S., and Koning A. J., "Temperature-dependent combinatorial level densities with the D1M Gogny force." *Phys. Rev. C*, vol. 86, p. 064317, 2012.

[51] Koning A. J., Hilaire S., and Goriely S., "Global and local level density models." *Nucl. Phys A*, vol. 810, p. 13, 2008.

[52] Capote R., Herman M., Obložinský P. *et al.*, "RIPL: Reference Input Parameter Library for Calculation of Nuclear Reactions and Nuclear Data Evaluations." *Nucl. Data Sheets*, vol. 110, p. 3107, 2009.

[53] EANM, "EANM 2019 Radiopharmacy: An Update. Published by European Association of Nuclear Medicine," 2019. [Online]. Available: https://www.eanm.org/publications/technologists-guide

[54] Stabin M. and Farmer A., "OLINDA/EXM 2.0: The new generation dosimetry modeling code." *J. Nucl. Med.*, vol. 53, pp. 585–585, 2012.

[55] Stabin M., Sparks R. B., and Crowe E., "OLINDA/EXM: the second-generation personal computer software for internal dose assessment in nuclear medicine." *J. Nucl. Med.*, vol. 46, pp. 1023–1027, 2005.

[56] Stabin M. and Siegel J. A., "Radar dose estimate report: a compendium of radiopharmaceutical dose estimates based on OLINDA/EXM version 2.0." *J. Nucl. Med.*, vol. 59, pp. 154–60, 2017.

[57] Stabin M., Xu X. G., Emmons M. A., Segars W. P., Shi C., and Fernald M. J., "RADAR Reference Adult, Pediatric, and Pregnant Female Phantom Series for Internal and External Dosimetry." *J. Nucl. Med.*, vol. 53, pp. 1807–1813, 2012, doi:10.2967/jnumed.112.106138.

[58] ICRP 89, "Basic anatomical and physiological data for use in radiological protection reference values. ICRP Publication 89. Ann. ICRP 2002;32(3-4)." 2002, doi:10.1016/0146-6453(81) 90127-5.

[59] ICRP 103, "ICRP 2007 The 2007 Recommendations of the International Commission on Radiological Protection. ICRP Publication 103. Ann. ICRP 37 (2–4)." 2007. [Online]. Available: www.icrp.org/publication.asp?id= ICRPPublication103

[60] Müller C., Bunka M., Haller S., Koster U., Groehn V., Bernhardt P., van der Meulen N., Turler A., and Schibli R., "Promising prospects for ^{44}Sc-/^{47}Sc-based theragnostics: application of ^{47}Sc for radionuclide tumor therapy in mice." *J. Nucl. Med.*, vol. 55, pp. 1658–64, 2014.

[61] Siwowska K. *et al.*, "Therapeutic potential of ^{47}Sc in comparison to ^{177}Lu and ^{90}Y: preclinical investigations." *Pharmaceutics*, vol. 11, p. 424, 2019.

[62] Mikolajczak R. *et al.*, "Production of scandium radionuclides for theranostic applications: towards standardization of quality requirements." *EJNMMI Radiopharmacy and Chemistry*, vol. 6, p. 19, 2021.

[63] Qaim S. M., Scholten B., and Neumaier B., "New developments in the production of theranostic pairs of radionuclides." *J. Radioanal. Nucl. Chem.*, vol. 318, p. 1493–1509, 2018.

[64] Agency I. A. E., "cyclotron produced radionuclides: principle and practise." *Technical Reports series No.*, vol. 465, 2008.

[65] Loveless C. S. *et al.*, "Photonuclear production, chemistry,and in vitro evaluation of the theranostic radionuclide ^{47}Sc." *EJNMMI Research*, vol. 9, p. 42, 2019.

[66] Rane S., Harris J. T., and Starovoitova V. N., "^{47}Ca production for ^{47}Ca/^{47}Sc generator system using electron linacs." *Appl Radiat Isot*, vol. 97, pp. 188–192, 2015.

[67] Starovoitova V. N., Cole P. L., and Grimm T. L., "Accelerator-based photoproduction of promising beta-emitters ^{67}Cu and ^{47}Sc." *J Radioanal Nucl Chem*, vol. 305, p. 127–132, 2015.

[68] Rotsch D. A., Brown M. A., Nolen J. A., Brossard T., Henning W. F., Chemerisov S. D., Gromov R. G., and Greene J., "Electron linear accelerator production and purification of ^{47}Sc from titanium dioxide targets." *Appl Radiat Isot*, vol. 131, p. 77–82, 2018.

[69] Mamtimin M., Harmon F., and Starovoitova V. N., "Sc-47 production from titanium targets using electron linacs." *Appl Radiat Isot.*, vol. 102, pp. 1–4, 2015.

[70] Snow M. S., Foley A., Ward J. L., Kinlaw M. T., Stoner J., and Carney K. P., "High purity ^{47}Sc production using high-energy photons and natural vanadium targets." *Appl Radiat Isot.*, vol. 178, p. 109934, 2021.

[71] Minegishi K., Nagatsu K., Fukada M., Suzuki H., Ohya T., and Zhang M., "Production of scandium-43 and -47 from a powdery calcium oxide target via the $^{nat/44}$Ca(α,x)-channel." *Appl Radiat Isot.*, vol. 116, pp. 8–12, 2016.

[72] Gadioli E., Gadioli E. E., Hogan J. J., and Burns K. I., "Emission of α particles in the interaction of 10-85 MeV protons with ^{48,50}Ti." *Z. Phys. A-Hadron. Nucl.*, vol. 301, pp. 289–300, 1981.

[73] Misiak R., Walczak R., B W. *et al.*, "^{47}Sc production development by cyclotron irradiation of ^{48}Ca." *J Radioanal Nucl Chem*, vol. 313, p. 429–434, 2017.

[74] Pupillo G., Mou L., Boschi A. *et al.*, "Production of ^{47}Sc with natural vanadium targets: results of the PASTA project." *Journal of Radioanalytical and Nuclear Chemistry*, vol. 322, pp. 1711–1718, 2019.

[75] Barbaro F., Canton L., Carante M. P. *et al.*, "New results on proton-induced reactions on vanadium for ^{47}Sc production and the impact of level densities on theoretical cross sections," *Phys. Rev. C*, vol. 104, p. 044619, 2021.

[76] De Nardo L. *et al.*, "Preliminary dosimetric analysis of DOTA-folate radiopharmaceutical radiolabelled with ^{47}Sc produced through ^{nat}V(p,x)^{47}Sc cyclotron irradiation." *Phys. Med. Biol.*, vol. 66, p. 025003, 2021.

[77] "IAEA Database of cyclotrons for radionuclide production," 1983, retrieved Sept 8, 2023. [Online]. Available: https://nucleus.iaea.org/sites/accelerators/Pages/Cyclotron.aspx

[78] Pupillo G., Mou L., Manenti S., Groppi F., Esposito J., and Haddad F., "Nuclear data for light charged particle induced production of emerging medical radionuclides." *Radiochim. Acta*, vol. 110, p. 689–706, 2022.

[79] Tárkányi F., Ditrói F., Takács S., Hermanne A., Baba M., and Ignatyuk A. V., "Investigation of activation cross-sections of deuteron induced reactions on vanadium up to 40 MeV." *Nuclear Instruments and Methods in Physics Research Section B: Beam Interactions with Materials and Atoms*, vol. 269, no. 15, pp. 1792–1800, 2011.

[80] Duchemin C., Guertin A., Haddad F., Michel N., and Métivier V., "Production of Medical Isotopes from a Thorium Target Irradiated by Light Charged Particles up to 70 MeV." *Phys. Med. Biol.*, vol. 60, p. 931, 2015.

[81] De Dominicis L., Mou L., Cisternino S., Campostrini M., Rigato V., Nigron E., Haddad F., and Pupillo G., "^{47}Sc production with proton beams on isotopically enriched ^{48}Ti and ^{49}Ti targets," *Journal of Physics: Conference Series*, vol. 2586, no. 1, p. 012128, 2023.

[82] Levkovskij V. N., *Cross-Section of Medium Mass Nuclide Activation (A = 40–100) by Medium Energy Protons and Alpha-Particles (E = 10–50 MeV).* Inter-Vesi: Moscow, Russia, 1991.

[83] IAEA, "IAEA, Monitor Reactions." [Online]. Available: https://www-nds.iaea.org/medical/monitor_reactions.html

[84] Takacs, S ans Tarkanyi, F. a. S. M. and Hermanne A., "Investigation of the ^{nat}Mo(p,x)^{96mg}Tc nuclear reaction to monitor proton beams: New measurements and consequences on the earlier reported data." *Nucl. Instrum. Methods Phys. Res. B*, vol. 198, p. 183–196, 2002.

[85] Dellepiane G., Casolaro P., Mateu I., Scampoli P., Voeten N., and Braccini S., "^{47}Sc and ^{46}Sc cross-section measurement for an optimized ^{47}Sc production with an 18 MeV medical PET cyclotron." *Applied Radiation and Isotopes*, vol. 189, p. 110428, 2022.

[86] Goriely S., Tondeur F., and Pearson J. M., "A HARTREE–FOCK NUCLEAR MASS TABLE," *Atomic Data and Nuclear Data Tables*, vol. 77, no. 2, pp. 311–381, 2001.

[87] Sean L., *Essential in Metaheuristics*. lula.com, 2012.

[88] Gad A. F., "PyGAD: An Intuitive Genetic Algorithm Python Library," 2021.

[89] "Genetic Algorithm Python," retrieved Oct 6, 2023. [Online]. Available: https://github.com/ahmedfgad/GeneticAlgorithmPython

[90] "pygad 3.2.0 ," retrieved Oct 6, 2023. [Online]. Available: https://pypi.org/project/pygad/

[91] Avrigeanu M., Rochman D., Koning A. J. *et al.*, "Advanced breakup-nucleon enhancement of deuteron-induced reaction cross sections." *Eur. Phys. J. A*, vol. 58, p. 3, 2022.

[92] Canton L., Barbaro F., De Dominicis L., Mou L., and Pupillo G., "Metodo per produzione di Sc-47 ad alta purezza con ciclotroni ad energie intermedie (35 MeV) attraverso un bersaglio multistrato." *INFN Office for Technological Transfe*, p. Patent application No.102023000018477, 08/09/2023.

[93] Koning A., *ISOTOPIA-1.0, Simulation of medical isotope production with accelerators*, 2019.

[94] "Medical isotope browser," 2009, retrieved Sept 8, 2023. [Online]. Available: https://www-nds.iaea.org/relnsd/isotopia/isotopia.html

[95] Saar G., Millo C. M., Szajek L. P., Bacon J., Herscovitch P., and Koretsky A. P., "Anatomy, Functionality, and Neuronal Connectivity with Manganese Radiotracers for Positron Emission Tomography." *Mol. Imaging. Biol.*, vol. 20, pp. 562–574, 2018.

[96] Napieczynska H. *et al.*, "Imaging neuronal pathways with ^{52}Mn PET." *Neuroimage*, vol. 158, pp. 112–125, 2017.

[97] Li K., Yang Y., Guo D., Sun D., and Li C., "Clinical and MRI Features of Posterior Reversible Encephalopathy Syndrome With Atypical Regions: A Descriptive Study With a Large Sample Size." *Frontiers in Neurology*, vol. 11, 2020. [Online]. Available: https://www.frontiersin.org/article/10.3389/fneur.2020.00194

[98] Graves S. A. *et al.*, "Preparation and in vivo characterization of $^{51}MnCl_2$ as PET tracer of Ca^{2+} channel-mediated transport." *Sci Rep*, vol. 7, p. 3033, 2017.

[99] Coenen H. H. *et al.*, "Consensus nomenclature rules for radiopharmaceutical chemistry — Setting the record straight." *Nucl. Med. Biol.*, vol. 55, pp. v–xi, 2017.

[100] Wooten A. L., Aweda T. A., Lewis B. C., Gross R. B., and Lapi S. E., "Biodistribution and PET Imaging of pharmacokinetics of manganese in mice using Manganese-52." *PLoS One*, vol. 12, 2017.

[101] El Sayed R., Massicano A. V. F., Queern S. L., Loveless C. S., and Lapi S. E., "Manganese-52 production cross-section measurements via irradiation of natural chromium targets up to 20 MeV." *Applied Radiation and Isotopes*, vol. 147, pp. 165–170, 2019.

[102] Barbaro F., Canton L., Carante M. P. *et al.*, "The innovative ^{52g}Mn for positron emission tomography (PET) imaging: Production cross section modeling and dosimetric evaluation." *Med Phys.*, pp. 1–12, 2022.

[103] Dmitriev P. P., Konstantinov I. O., and Krasnov N. N., "Methods for producing the Mn^{52} isotope." *Atomic Energy*, vol. 26, no. 5, pp. 539–541, 1969.

[104] Bowman W. W. and Blann M., "Reactions of ^{51}V and ^{27}Al with 7–120 MeV α-particles (equilibrium and non-equilibrium statistical analyses)." *Nuclear Physics A*, vol. 131, no. 3, pp. 513–531, 1969.

[105] Michel R., Brinkmann G., and Stück R., "Measurement and hybrid model analysis of integral excitation functions for α-induced reactions on vanadium and manganese." in *Nuclear Data for Science and Technology*, Böckhoff K. H., Ed. Dordrecht: Springer, 1983, pp. 599–600.

[106] Rao J. R. *et al.*, "Non-equilibrium effects in α-particle-induced reactions in light, medium and heavy nuclei up to 120 MeV." *Journal of Physics G: Nuclear Physics*, vol. 13, no. 4, p. 535, 1987.

[107] West H. I., Lanier R. G., and Mustafa M. G., "^{52}Cr(p,n)^{52g,m}Mn and ^{52}Cr(d,2n)^{52g,m}Mn excitation functions." *Phys. Rev. C*, vol. 35, pp. 2067–2076, 1987.

[108] Sonzogni A. A., Romo A. S. M. A., Mosca H. O., and Nassiff S. J., "Alpha and deuteron induced reactions on vanadium." *Journal of radioanalytical and nuclear chemistry*, vol. 170, no. 1, pp. 143–156, 1993.

[109] Ismail M., "Measurement of excitation functions and mean projected recoil ranges of nuclei in α-induced reactions on F, Al, V, Co and Re nuclei." *Pramana.*, vol. 40, no. 3, p. 227, 1993.

[110] Singh N. L., Mukherjee S., Mohan Rao A. V., Chaturvedi L., and Singh P. P., "Effects of pre-equilibrium nucleon emission on excitation functions of various reactions in vanadium induced by alpha particles." *Journal of Physics G: Nuclear and Particle Physics.*, vol. 21, no. 3, p. 399, 1995.

[111] Chowdhury D. P., Pal S., Saha S. K., and Gangadharan S., "Determination of cross section of α-induced nuclear reaction on natural Cr and Zr by stacked foil activation for thin layer activation analysis." *Nuclear Instruments and Methods in Physics Research Section B: Beam Interactions with Materials and Atoms*, vol. 103, no. 3, pp. 261–266, 1995.

[112] Kumar B. B., Mukherjee S., and Singh N. L., "Pre-equilibrium Model Analysis of Alpha Particle Induced Reactions up to 80 MeV." vol. 57, no. 2, pp. 201–206, feb 1998. [Online]. Available: https://doi.org/10.1088/0031-8949/57/2/007

[113] Peng X., He F., and Long X., "Excitation functions for α-induced reactions on vanadium." *Nuclear Instruments and Methods in Physics Research Section B*, vol. 152, pp. 432–6, 1999.

[114] "EXFOR: Experimental Nuclear Reaction Data - IAEA NDS," retrieved Sept 16, 2023. [Online]. Available: https://www-nds.iaea.org/exfor/

[115] Avrigeanu V., Avrigeanu M., and Mănăilescu C., "Further explorations of the α-particle optical model potential at low energies for the mass range $a \approx 45$–209." *Phys. Rev. C*, vol. 90, p. 044612, 2014.

[116] Ali B. *et al.*, "Activation cross-section data for α-particle-induced nuclear reactions on natural vanadium for practical applications." *Pramana - Journal of Physics*, vol. 90, no. 3, 2018.

[117] Singh N. L., Agarwal S., and Rao J. R., "Excitation function for α-particle-induced reactions in light-mass nuclei." *Canadian Journal of Physics*, vol. 71, no. 3-4, p. 115, 1993.

[118] Hansper V. Y., Morton A. J., Tims S. G., Tingwell C. I. W., Scott A. F., and Sargood D. G., "Cross sections and thermonuclear reaction rates for ^{51}V(α,n)^{54}Mn and ^{51}V (α,p)^{54}Cr." *Nuclear Physics A*, vol. 551, no. 1, pp. 158–172, 1993.

[119] Meléndez-Alafort L. *et al.*, "Internal radiation dose assessment of radiopharmaceuticals prepared with cyclotron-produced ^{99m}Tc." *Med. Phys.*, vol. 46, p. 1437–46, 2019.

[120] Hernandez R. *et al.*, "Radiomanganese PET Detects Changes in Functional β-Cell Mass in Mouse Models of Diabetes." *Diabetes*, vol. 66, p. 2163–2174, 2017.

[121] Mahoney J. and Small W., "Studies on manganese: III. The biological half-life of radiomanganese in man and factors which affect this half-life." *J. Clin. Investig.*, vol. 47, pp. 643–653, 1968.

[122] Stabin M., "Health concerns related to radiation exposure of the female nuclear medicine patient." *Environ. Health Perspect.*, vol. 105, p. 1403–9, 1997.

[123] De Nardo L., Ferro-Flores G., Bolzati C., Esposito J., and Meléndez-Alafort L., "Radiation effective dose assessment of [^{51}Mn]- and [^{52}Mn]-chloride." *Appl. Radiat.Isot.*, vol. 153, p. 108805, 2019.

[124] Müller C., Zhernosekov K., Koster U., Johnston K., Dorrer H., Hohn A. *et al.*, "A Unique Matched Quadruplet of Terbium Radioisotopes for PET and SPECT and for - and –Radionuclide Therapy: An In Vivo Proof-of-Concept Study with a New Receptor-Targeted Folate Derivative." *J Nucl Med*, vol. 53, pp. 1951–9, 2012.

[125] Price E. W. and Orvig C., "Matching chelators to radiometals for radiopharmaceuticals." *Chem Soc Rev*, vol. 260, p. 260–90, 2014.

[126] Müller C., Fischer E., Behe M., Köster U., Dorrer H., Reber J. *et al.*, "Future prospects for SPECT imaging using the radiolanthanide terbium-155 — production and preclinical evaluation in tumor-bearing mice." *Nucl Med Biol*, vol. 41, pp. e58–65, 2014.

[127] Dmitriev P. P., Molin G. A., and Dmitrieva Z. P., "Production of ^{155}Tb for nuclear medicine in the reactions ^{155}Gd(p,n), ^{156}Gd(p,2n), and ^{155}Gd(d,2n)." *Sov At Energy*, vol. 66, pp. 470–2, 1989.

[128] Vermeulen C., Steyn G. F., Szelecsényi F., Kovács Z., Suzuki K., Nagatsu K. *et al.*, "Cross sections of proton-induced reactions on natGd with special emphasis on the production possibilities of ^{152}Tb and ^{155}Tb." *Nucl Instruments Methods Phys Res Sect B Beam Interact with Mater Atoms*, vol. 260, p. 24–32, 2012.

[129] Formento-Cavaier R., Haddad F., Alliot C., Sounalet T., and Zahi I., "New excitation functions for proton induced reactions on natural gadolinium up to

70 MeV with focus on 149Tb production." *Nucl Instruments Methods Phys Res Sect B Beam Interact with Mater Atoms.*, vol. 478, pp. 174–81, 2020.

[130] Favaretto C., Talip Z., Borgna F., Grundler P. V., Dellepiane G., Sommerhalder A., Zhang H., Schibli R., Braccini S., Müller C., and van der Meulen N. P., "Cyclotron production and radiochemical purification of terbium-155 for SPECT imaging." *EJNMMI radiopharm. chem.*, vol. 6, p. 37, 2021.

[131] Dellepiane G., Casolaro P., Favaretto C., Grundler P. V., Mateu I., P. S., Talip Z., van der Meulen N. P., and Braccini S., "Cross section measurement of terbium radioisotopes for an optimized ^{155}Tb production with an 18 MeV medical PET cyclotron." *Applied Radiation and Isotopes*, vol. 184, p. 110175, 2022.

[132] Müller C., Reber J., Haller S., Dorrer H., Bernhardt P., Zhernosekov K. *et al.*, "Direct in vitro and in vivo comparison of (161)Tb and (177)Lu using a tumour-targeting folate conjugate." *Eur J Nucl Med Mol Imaging*, vol. 41, p. 476–85, 2014.

[133] Augusto R. M. S., Buehler L., Lawson Z., Marzari S., Stachura M., Stora T. *et al.*, "CERN-MEDICIS (Medical Isotopes Collected from ISOLDE): A New Facility." *Applied Sciences*, vol. 4, pp. 265–281, 2014.

[134] Webster B., Ivanov P., Russell B., Collins S., Stora T., Ramos J. P. *et al.*, "Chemical Purification of Terbium-155 from Pseudo-Isobaric Impurities in a Mass Separated Source Produced at CERN." *Sci Rep*, vol. 9, p. 10884, 2019.

[135] Fiaccabrino D. E., Kunz P., and Radchenko V., "Potential for production of medical radionuclides with on-line isotope separation at the ISAC facility at TRIUMF and particular discussion of the examples of ^{165}Er and ^{155}Tb." *Nucl Med Biol*, vol. 94-95, pp. 81–91, 2021.

[136] Steyn G. F., Vermeulen C., Szelecsényi F., Kovács Z., Hohn A., Van Der Meulen N. P. *et al.*, "Cross sections of proton-induced reactions on ^{152}Gd, ^{155}Gd and ^{159}Tb with emphasis on the production of selected Tb radionuclides." *Instruments Methods Phys Res Sect B Beam Interact with Mater Atoms*, vol. 319, pp. 128–40, 2014.

[137] Tárkányi F., Hermanne A., Ditrói F., Takács S., and Ignatyuk A. V., “Activation cross-sections of longer lived radioisotopes of proton induced nuclear reactions on terbium up to 65 MeV.” *Appl Radiat Isot*, vol. 127, pp. 7–15, 2017.